APPROXIMATE SOLUTION OF MELT DEPTH INSIDE TITANIUM DURING LASER MATERIALS PROCESSING

DINEO NGWENYA

A dissertation submitted to the Faculty of Engineering and the Built Environment in fulfilment of the requirements for the degree of Master of Science in Mechanical Engineering

SEPTEMBER 2015

Acknowledgements

I would like to thank God for helping me see this research through. I would also like to extend a note of my deepest gratitude to the following people:

- Professor F.-J. Kahlen for his patience, wisdom and guidance throughout this project.
- Technology Innovation Agency of South Africa for sponsoring this project.
- The CME staff for welcoming me as one of their own and always willing to help with lab-related issues.
- Professor R. B Knutsen for his willingness to help with orientating me on titanium metallurgy.
- My mom for her remarkable emotional and financial support.
- Thabang Msisinyane for the love and support that made the tough times manageable.
- The rest of my family for the love and prayers.
- Soraya Allies, Letlotlo Kgomongoe and Sikelelwa Ndwayi for various ways in which they contributed towards helping me through this project.

Abstract

The use of lasers has increased in areas of science, engineering and medicine. Their advantages over the traditional methods of thermal application are their ability to localize thermal treatments, ability to deliver high power density and to complete thermal processes in extremely short time periods. During the irradiation of a material, only a portion of the laser beam energy is absorbed. If the absorbed energy is high enough, melting can occur. The ability to predict, thus control the melting process is an advantage to manufacturing processes such as laser welding, surface re-melting and alloying.

Using analytical approaches that are already in existence, this research adapts a mathematical model to approximate temperature profiles as well as isothermal depths given a single laser pulse. In order to assess the error associated with the adapted model, laser irradiation experiments are carried out on CP titanium samples using a focal spot of $600\ \mu m$ and nitrogen gas as the shielding gas at a flow rate of $5\ l/min$.

The effects of some important laser processing parameters on the melt depth are discussed. The adapted model approximated that the melt depth increases with both increasing laser power and increasing pulse duration. Furthermore, the experimental results revealed that it is the combination of short pulses and a high laser power that yields melt zones that are relatively free of porosity, craters and cracking. Additionally, an assessment of the error associated with the adapted model revealed that the adapted model generally overestimates the experimental data with increasing laser pulse duration. At a combination of $0.1s$ and $1200W$ (representing a combination of short laser pulse and high laser power) the error of approximation was 59%. The error increased to 90% at a combination of laser parameters $5s$ and $600W$ (representing a combination of a long laser pulse and low laser power). It is recommended that future studies be undertaken to improve modelling accuracies for a wider range of laser processing parameters.

Table of contents

List of Figures

List of Tables

Nomenclature

A	Absorption coefficient
I	Laser beam intensity (W/m^2)
L	Latent heat of fusion (J/kg)
P	Power (W)
τ	Irradiation time/pulse duration (s)
x	Depth (m)
T	Temperature (K)
$T(x,\tau)$	Temperature as a function of depth and time
$X(\tau)$	Melt depth (m)
k	Conductivity (W/mK)
α	Thermal diffusivity (m^2/s)
ρ	Density (kg/m^3)

Subscripts

amb	Ambient
l	Liquid phase
s	Solid phase
m	Melting point

1 INTRODUCTION

Ever since the 1960's lasers have superseded traditional methods of thermal application because of their advantageous abilities [1, 2]. Lasers have the ability to localize thermal treatments, complete thermal processes in extremely short time periods, and deliver high-power densities, amongst other favourable features.

One of the uses of laser technology has been material surface modification. As such, there has been an interest in laser surface modifications of materials known to have poor tribological properties such as titanium. High friction coefficient, low adhesive and fretting wear resistance are properties of titanium that are considered as limiting factors to its application in tribilogical uses [3-7]. The engineering community has seen the use of lasers extending into welding and alloying of materials. Even with the advantages that laser technology brings in engineering, there are still to be considered the effects of the resulting heat transfer on the metallurgy of the irradiated metal. These effects can be detrimental to the final material properties.

Therefore there is a need for the use of analytical models for the purpose of predicting the reactions of the material to heat. This can be done through predicting the temperature profiles expected to exist during laser heating. The heat transfer occurring inside a laser-irradiated target has been studied both theoretically and experimentally before [8-13]. The theoretical studies focussed mainly on developing mathematical models to predict melting during laser materials processing [10, 11, 14, 15].

It is in the prediction of melting during laser materials processing that the interest of this research study lies. Given that there already exist bodies of work that have developed analytical models that predict melting during laser-irradiation of a material, the current research project aims to adapt the existing analytical models into its region of interest for laser irradiating titanium.

2 LITERATURE REVIEW

Laser technology is used extensively for various types of materials processing [10]. There has been a rise in the use of lasers in material processing areas such as spot welding, cutting, drilling of holes, surface treatment, etc. [16-18]. In these material processing areas the need to control the melting process is crucial to the desired results. Therefore, the use of lasers has induced interest in the study of the thermal effects of laser-assisted processes on the solid targets. In particular, lasers have been extensively used in surface modification of titanium and its alloys. Consequently, studies have taken an interest in the thermal effects of laser-assisted processes on titanium and its alloys [3-7, 19-21].

2.1 Titanium

Excellent combination of strength and toughness, corrosion resistance and high melting point are titanium's most recognized properties [19, 22-25]. Nevertheless, the application of titanium alloys under severe wear and friction conditions is highly restricted due to their poor tribological properties [19, 24-27]. Low strength commercially pure (CP) titanium is used in the fabrication of tanks, heat exchangers, reactor vessels for chemical processing, desalination and power generation plants [28-31]. It has also been widely used in the biomedical industry for its suitable mechanical properties and excellent biocompatibility [32-35]. At an approximate temperature of $1155\ K$ CP titanium undergoes an allotropic phase transformation from a hexagonal close packed crystal structure (alpha phase α) to a body centred cubic structure (beta phase β) [36-39]. Under different cooling rates titanium can undergo one of three modes of transformation: long-range, short-range and diffusionless $\beta \rightarrow \alpha$ transformation [40]. Therefore, depending on the thermal processing history, the microstructure of titanium can vary. For instance, slow cooled titanium can result in annealed equiaxed microstructure which is characteristic of long-range transformation [41]. Rapidly cooled titanium can form metastable phases such as martensite (α') consisting of the Widmanstatten or acicular microstructure [41]. The Widmanstatten and acicular microstructure are characteristic of either short-range/diffusionless transformation depending on the severity of the population of the Widmanstatten or acicular microstructure [41].

2.2 Laser-assisted processing of titanium

Due to poor tribological properties of titanium, there has been an interest in laser surface modification thereof [3-7]. Laser surface alloying and laser re-melting of titanium are some of the methods used to modify titanium surfaces. Laser re-melting of the surface of titanium involves using a high power laser to melt the surface of the workpiece. It is due to the associated rapid cooling of the molten surface that a layer of α' is formed, which has excellent wear and corrosion resistance [19]. Similar to laser re-melting, the titanium surface is melted using a laser beam during laser surface alloying. The molten surface is fed the alloying powder/gas additives. Nitrogen gas is the most commonly used alloying additive when laser gas alloying titanium [7, 19]. Xin et al. [7] found that the microstructure of the treated layer was dependent on laser power density amongst other factors. Similarly, Santos et al. [42] found that increasing the laser peak power resulted in crack formation due to the high cooling rates. Fu and Batchelor [43] attributed the significant improvement of the wear resistance of their samples to the hardness and corrosion resistance improvements of the nitrided layers.

In addition to laser surface modification, lasers have also been used in welding. Laser welding has been a commonly used technology to join titanium components in dental prosthesis and other medical devices [44-49]. The main problem with welding titanium is its nature to readily react with gases such as oxygen at elevated temperatures, especially in its liquid state [12, 22, 46, 50]. This reaction with gases can lead to weld embrittlement and rapid grain growth [12, 46, 51]. This problem can be reduced with laser welding [12, 52]. The high welding speeds and fast thermal cycles of laser welding significantly reduces the time in which the material is exposed to high temperatures. This was proven in a study of joining titanium materials with tungsten inert gas (TIG) welding and laser welding by Wang and Welsch [46]. They found that grain growth (hence the heat affected zone (HAZ)) was significant in welds produced by TIG welding, even with the use of shielding gas. In welds produced by laser welding, they found localized fusion zones and heat affected zones (HAZ) that were limited only to the surface regions in the joint [46]. Comparatively, they found that laser welding caused localized fusion zones and HAZ that were limited to the surface regions in the joined areas. These results by Wang and Welsch [46] show the improvement in the state of the material post welding when laser welding is employed. Further improvements are desired as far as eliminating the HAZ associated with welding. However, this advantage of laser application in welding over the traditional welding methods has led to studies about the effects of laser welding titanium on resulting welds [40, 41, 49, 53].

2.2.1 *Microstructural effects of cooling rates associated with laser processes*

As already mentioned in the previous subchapter there are three kinds of $\beta \rightarrow \alpha$ transformation mechanisms observed in CP titanium which are dependent on cooling rates [40]. They are the long-range diffusional transformation at low cooling rates, short-range diffusional transformation at medium cooling rates, and diffusionless transformation at high cooling rates [40]. The regions closest to the point heating source (e.g., melt zone/fusion zone) experience the highest peak temperatures [54]. Therefore, these regions will experience the highest cooling rates. Consequently, the expected $\beta \rightarrow \alpha$ transformation mechanism, observed in the melt zone, is either the short-range diffusional or diffusionless transformation.

In their research, Buddery et al. [49] found that whilst many studies reported a columnar microstructure in pulsed welds of titanium, others reported a predominantly acicular microstructure. Liu et al. [40] studied the microstructural evolution of the fusion zone (referred to as melt zone in this study). They reported that with an increase in the welding speed, the microstructure became increasingly more columnar. Welding speed is indicative of cooling rates. With high welding speeds, the material is exposed to elevated temperatures for shorter periods than with lower welding speeds. The shorter the time that the material is exposed to elevated temperatures, the more localized the HAZ is. Therefore, the thermally unaffected area will consequently act as a heat sink, thus increasing the cooling rate. As shown in Figure 2.1, at low cooling rates (Figure 2.1(a)) granular-like microstructure was found in the melt zone, and with increased cooling rates (Figure 2.1(c)) there was an increase in the appearance of columnar-like structures. In their study, cooling rates were concluded to be the determining factor for the final microstructure.

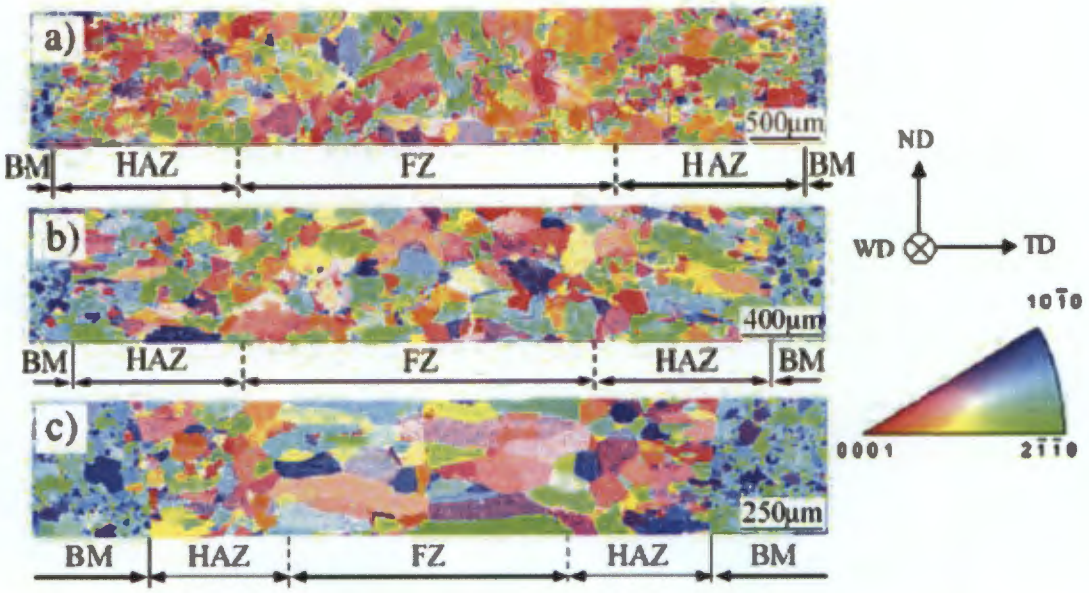

Figure 2.1: Grain orientation maps in the centre parts of the vertical cross-sections under various welding conditions: (a) $10kW - 2m/min$; (b) $10kW - 4m/min$; and (c) $10kW - 8m/min$. WD: Welding direction; ND: Normal direction; TD: Transverse direction; BM: Base metal; HAZ: Heat affected zone; and FZ: Fusion zone [40].

In a study by Yunlian et al. [53] the effects of cooling rates on the titanium weld microstructure were investigated through welding of titanium by different welding methods. Each welding method (laser beam, electron beam and gas tungsten arc (TIG) welding) represented a different cooling rate. Similar to Liu et al. [40], Yulian et al. [53] concluded that cooling rates influenced the resulting microstructure. However, unlike Liu et al. [40], they found that laser beam welding produced titanium welds that were predominantly acicular in microstructure. This is shown in Figure 2.2. The high temperatures and low welding speed of TIG resulted in the size of the grains being the largest, while the size by laser beam welding were the finest.

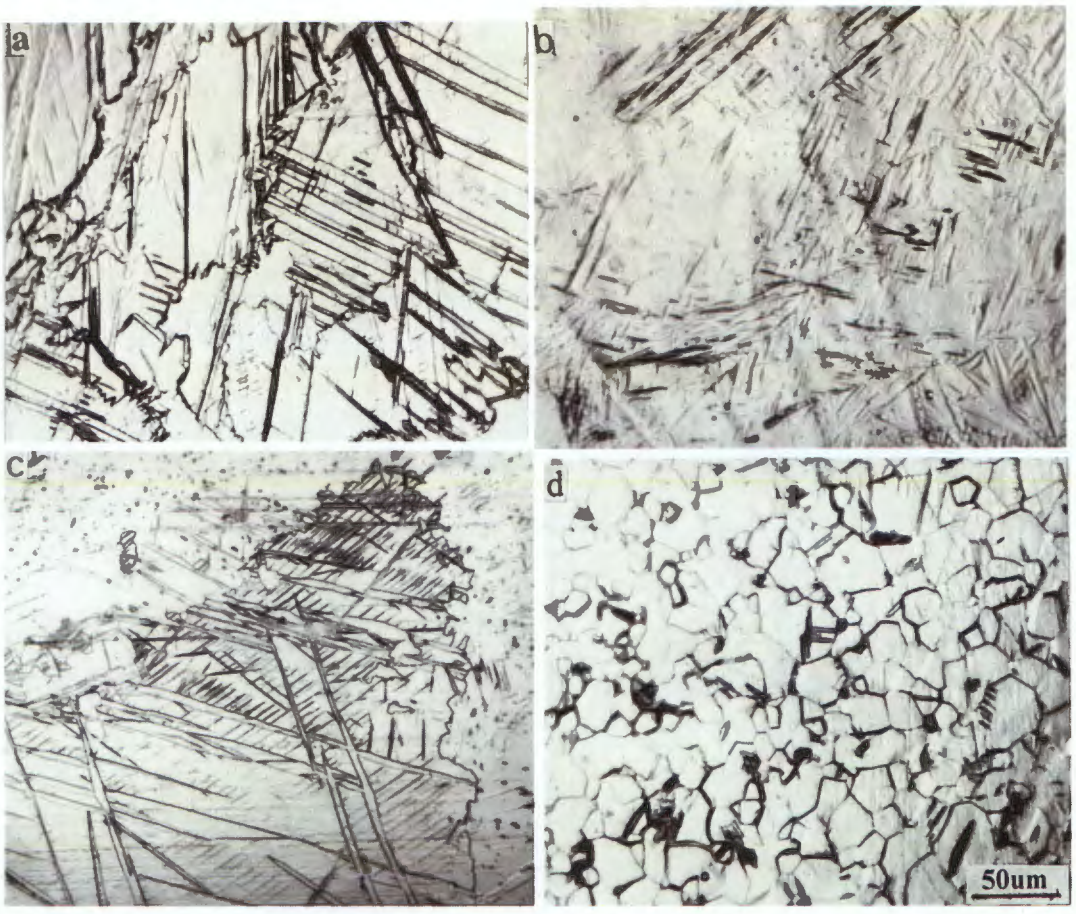

Figure 2.2: Titanium microstructures of: (a) an electron beam weld $v = 1.8m/min$; (b) a laser beam weld $v = 3m/min$; (c) a gas tungsten arc weld $v = 0.48m/min$; and (d) base metal [53].

Li et al. [55] also reported on the presence of coarse columnar α-Ti grains in the melt zone post laser welding. As shown in Figure 2.3, they found that the degree of grain coarsening increased from the periphery towards the centre of the melt zone. With increasing welding speed the appearance of acicular microstructure is noted in Figure 2.3. The common conclusion drawn from Figures 2.1 - 2.3 by the respective researchers was that cooling rates strongly affect the $\beta \rightarrow \alpha$ transformation mechanism. However, the different degrees to which the acicular α' is found suggests that the critical cooling rates at which each phase transformation mechanism occurs are different for Figures 2.1 – 2.3. The maximum welding speed that Liu et al. [40] and Li et al. [55] used in their studies was $8m/min$. This welding speed is greater than the $3m/min$ used by Yunlian et al. [53]. Therefore, the cooling rates associated with the highest welding speed should result in the highest cooling rates. However, it is Yunlian et al. [53] that reported a predominant acicular microstructure. Therefore, it is a likely explanation that the critical cooling rate at which the phase transformation mechanisms occurred in the study of Yunlian et al. [53] was altered.

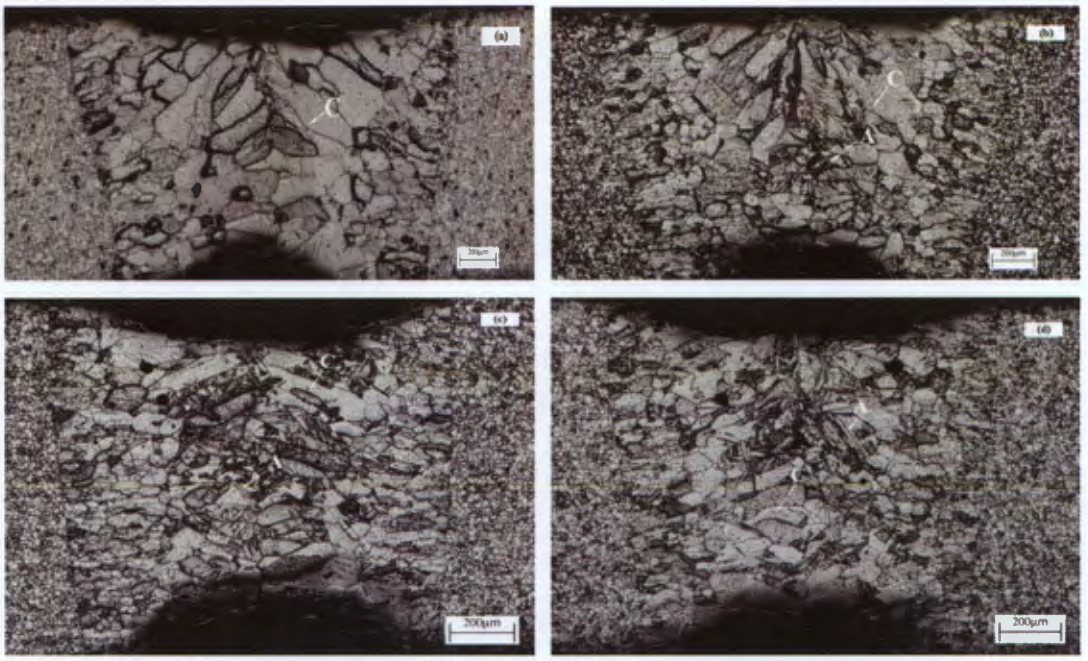

Figure 2.3: Microstructure of fibre laser welded titanium at laser power $2kW$ and welding speed: (a) $4m/min$; (b) $5m/min$; (c) $7m/min$; and (d) $8m/min$. C: columnar α-Ti grains and A: acicular α-Ti [55].

The critical cooling rates at which each transformation mechanism occurs, strongly depend on the alloying elements [40]. In the case of unalloyed titanium, the critical cooling rate depends on the degree of material contamination. For instance, the range of cooling rates for short-range diffusional transformation is significantly influenced by the presence of iron (Fe) in pure titanium [40]. It has been reported that the higher the iron content in titanium, the lower the cooling rates between which short-range diffusional transformation occurs [40]. For instance, the short-range transformation of extra-pure titanium (with $0.0004\ wt\ \%$ Fe) occurs at cooling rates $350 - 1000℃/s$, that of grade 2 CP titanium (with $0.07\ wt\ \%$ Fe) occurs at cooling rates $90 - 600℃/s$, and that of grade 4 CP titanium (with $0.13\ wt\ \%$Fe) occurs at cooling rates $30 - 300℃/s$ [40]. This then suggests that the cooling rate range within which diffusionless transformation occurs in titanium decreases with increasing iron content.

In a study by Buddery et al. [49] on the effects of contaminations on the metallurgy of laser beam welded titanium, it was found that contaminations influenced the final weld microstructure. As shown in Figure 2.4, the findings of their study showed that with increased levels of contaminations, an acicular microstructure was predominant. Figure 2.4 also shows that the welds that had the lowest contamination exposure showed a columnar microstructure. Danielson et al. [41] also found similar results in their study of titanium welds microstructures.

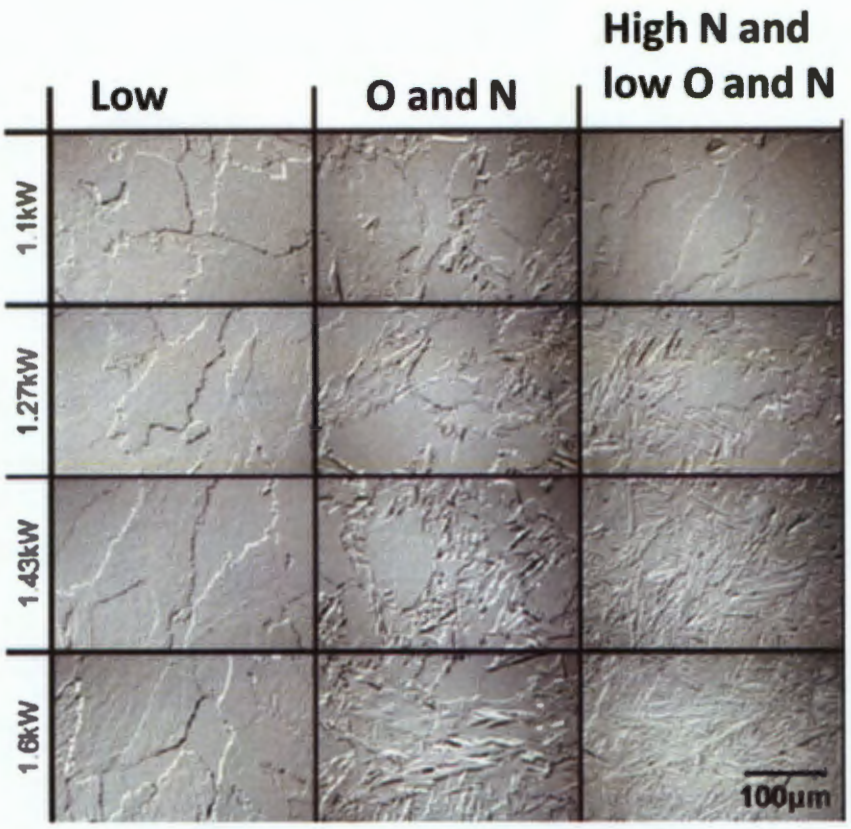

Figure 2.4: Microstructures for low, high O and N, and high Fe + low O and N contamination conditions at different pulse powers showing: columnar α-Ti under conditions of low contamination which does not appear to change with increasing pulse power; columnar α and portions of acicular α-Ti which increase with pulse power for conditions of high O and N; and columnar α-Ti at low pulse powers which becomes fine acicular α-Ti with increasing pulse power for conditions of high Fe + low O and N contamination [49].

2.2.2 Effects of the starting microstructure on the final microstructure

The starting microstructure plays a major role in determining the final microstructure post laser processing. However, it does not play as major a role in the melt zone as it does in the HAZ. The $\alpha \rightarrow \beta \rightarrow \alpha$ transformation kinetics in the HAZ of CP titanium arc welds were studied by Elmer et al. [54]. It is appreciated that this particular study was based on arc welding and not laser welding. However, due to a lack of studies focusing on the HAZ microstructural analysis of laser titanium welds, reference is made to other types of welding that produce similar microstructural effects because of similar thermal cycles. Elmer et al. [54] reported on three different microstructures in the HAZ post welding: (1) α-Ti that has undergone annealing and recrystallization; (2) partially transformed α-Ti where α and β coexist; and (3) single-phase β-Ti. These microstructures are shown in Figure 2.5. The starting microstructure shown in Figure 2.5 (a) was annealed to partially recover the cold

work that was introduced during machining [54]. Therefore, the samples had stored strain energy prior to welding. The driving force for annealing and recrystallization is strain energy. Therefore, it follows that there will be regions inside the HAZ that will not reach the beta transus temperature, but will reach temperatures high enough to anneal and recrystallize the microstructure.

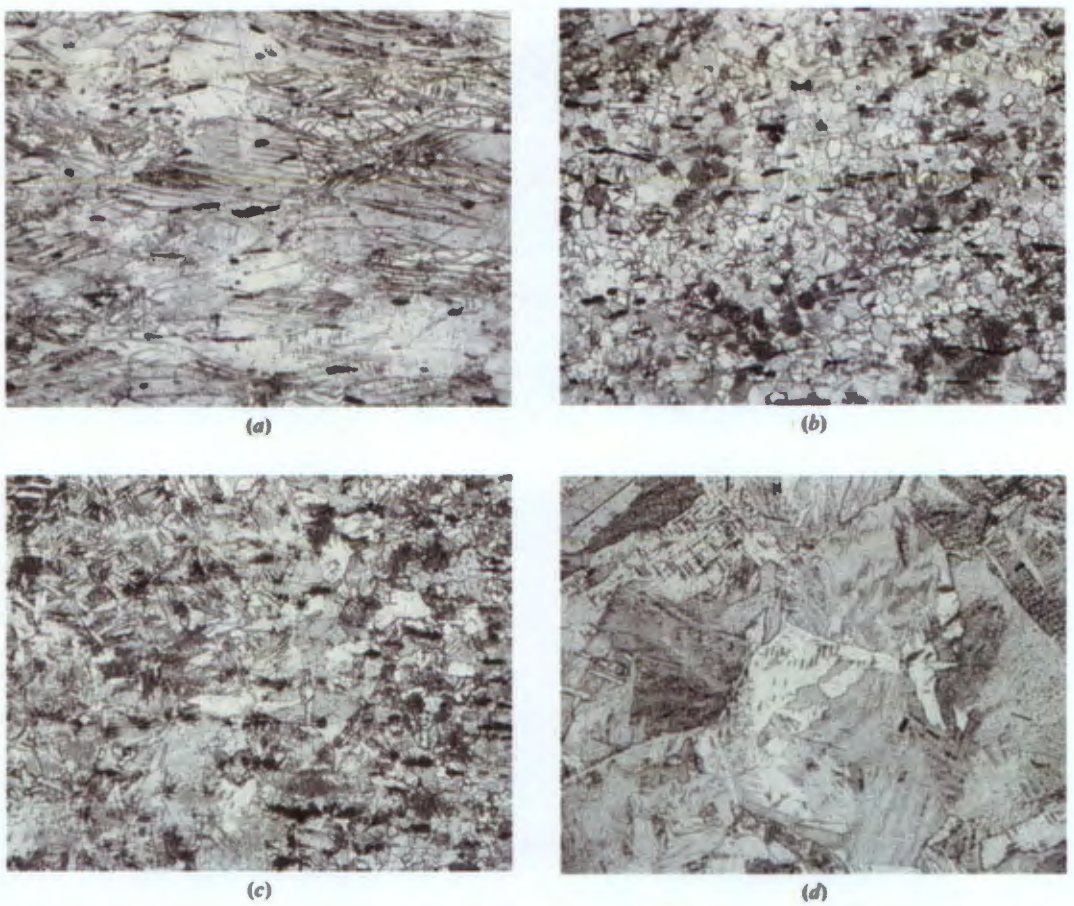

Figure 2.5: Microstructures of the base metal and HAZ of grade 2 titanium weld. (a) Base metal prior to welding; (b) annealed and recrystallized HAZ region, ~5 mm from the fusion line; (c) partially transformed HAZ region, ~2.5 mm from the fusion line; and (d) fully transformed HAZ region, ~0.4 mm from the fusion line. The fusion zone is to the left and the base metal is to the right in the micrographs. Micrographs are taken at the same magnification [54].

It is unclear as to what the morphology of the starting microstructure in the works of Liu et al. [40] and Li et al. [55] was. Therefore, it is not certain that their work did not report on HAZ regions that had undergone annealing and recrystallization because of the absence of strain energy. However, if their starting microstructure was at equilibrium characterized by equiaxed grains, the HAZ would not be expected to have annealed and recrystallized

regions. This is because equilibrium microstructure lacks the strain energy that is required for annealing and recrystallization to occur.

In light of the above review it has been shown that the resulting laser irradiated CP titanium microstructure is affected by thermal cycles, contaminations, starting microstructure and adequacy of shielding gas. It is important to note that the current study uses a stationary laser beam and the studies reviewed used travelling laser beams. However, it is expected that there will be cooling rates, contaminations, starting microstructure effects and shielding gas to be considered and accounted for even in stationary laser beam irradiation. Therefore, their effects on the final microstructure are worth understanding, even from materials processes that are slightly different from the stationary beam irradiation employed in this study.

2.3 The effects of laser parameters and thermo-physical properties on the melt zone

The melt zone geometry depends on input power density (incident power of a laser per unit area) thermal diffusivity, focal spot size, beam profile, laser power, travelling speed, gas shielding parameters, focal length, beam energy, pulse frequency and pulse duration (interaction time between laser beam and target surface) [12, 13, 56-63]. For different combinations of laser parameters, either shallow or deep and narrow welds are produced [12, 50, 56, 61, 64]. The different shapes of the melt zone are illustrated in Figure 2.6.

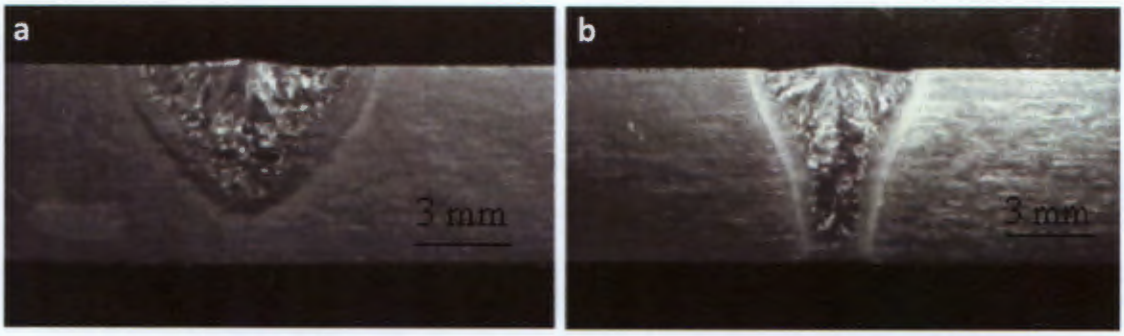

Figure 2.6: Macrograph showing a comparison between: (a) a shallow and wider Ti weld produced with operating parameters of $P = 4000W$, $v = 0.6\,m/min$, $energy\ density = 400J/mm^2$ and (b) a deeper and narrower Ti weld produce with operating parameters of $P = 8000W$, $v = 1.8\,m/min$, $energy\ density = 267J/mm^2$. Both welds are produced by fibre laser welding [12].

2.3.1 *Spot size and laser power effects on the melt zone*

In order to investigate the effects of spot size and laser power on the melt zone, literature on the aforementioned effects on welds was studied; in this study, a weld is synonymous to a melt zone.

Baba and Watanabe [50] investigated the effect of the combination of pulse energy and spot size on the geometry of a weld. They concluded that an increase in pulse energy increased the weld penetration/melt depth under constant spot size. They also concluded that the melt depth increased with a decrease in spot size. The decrease in spot size under constant pulse energy and duration resulted in an increase in the incident power density. The increase in melt depth due to increasing power density has been reported by other researchers [10, 13, 65, 66]. Akman et al. [61] investigated laser welding of Ti6Al4V titanium alloy and found that the melt depth increased linearly within a peak power range of $1.12kW - 2kW$ for a square pulse shape. However, they also found that the melt depth stopped increasing linearly after peak power of $2kW$. Instead, the melt depth was measured to be approximately constant around $1.8mm$ for a peak power range of $2kW - 2.3kW$, pulse duration of $5ms$ and beam spot diameter (on the surface) of $0.65mm$. They claimed that the arrest of the melt depth increase was due to plasma absorption of the incident laser beam that occurs at a peak power range from $2kW$ to $2.3kW$. Laser plasma is formed when a pulse delivers power density sufficient to vaporize the target metal surface [67, 68].

Plasma absorption has been reported to affect the growth of the melt depth regardless of increased incident power density [68, 69] [70]. In a study of the spectroscopy of the plasma plume induced during laser welding of titanium, Szymanski et al. [68] found that the average absorption of the laser radiation in the plasma plume was around 6%. Absorption of 6% may seem negligible thus could conclude that the absorption effects of laser plasma can be ignored during laser welding. However, the absorption measurements in their experiments were time-averaged over $200ms$ whilst plasma appeared in short bursts that lasted $100ms$. Therefore, they could not rule out the possibility that the absorption of the laser beam by the plasma during the bursts was substantial [68]. It has been reported that with continued metal vaporization at elevated temperatures, the formed plasma grows in height and diameter thus increasing the absorption of the incident laser beam [68, 69]. Also, Dowden et al. [70] describes in their analysis of the laser plasma interaction during laser keyhole welding that welding may cease should the plasma density become too dense. Therefore it a plausible explanation given by Akman et al. [61] that the melt depth ceased to increase at elevated peak power range from $2kW$ to $2.3kW$ because of laser plasma absorption of incident beam energy.

2.3.2 *Pulse duration effects on the melt depth*

In stationary laser irradiation (e.g. laser spot welding) the beam-material interaction time is the full pulse duration. In moving beam laser irradiation the beam-material interaction time is defined by the time in which a particular point on the target surface is exposed to the laser beam whilst the laser beam is moving with a constant speed [71]. Some researchers [10, 71] believe that when only considering the effects of pulse duration/interaction time on the melt pool size, the fact that it is stationary or moving beam irradiation can be ignored since the calculated interaction time is considered to be equivalent to pulse duration. This is possible only at the expense of ignoring the effects of either having a moving laser beam or one that is stationary on the flow patterns produced in the molten metal. The consideration of flow patterns created in the molten metal during beam-material interaction is beyond the scope of this study. However, the literature covered in this section utilized either a moving beam source or stationary one, thus the reader should bear in mind that the two (moving beam and stationary beam) have different liquid metal flow patterns. Because of the different liquid metal flow patterns produced by either having a moving or stationary beam, it is not expected that pulse duration of a stationary beam, and interaction time of a moving beam having the same value will give identical melt pools. However, it is speculated that the effects of each beam type on the melt depth will be similar. Figure 2.7 shows the dependence of the melt depth (penetration depth) on interaction time as found by Suder and Williams [71]. To vary the interaction time in their experiments, the travel speed was changed from 0.3 to $15m/min$ and the power density was varied by changing the laser power from $2kW$ to $8kW$. It is important to note that the lowest power density of $0.5MW/cm^2$ corresponds to the highest attained density used in the current study ($0.424MW/cm^2$). Therefore, only one trend in Figure 2.7 is achievable and is a realistic reference to this study. However, it is still worth noting the effects of interaction time on the penetration depth even at high power densities.

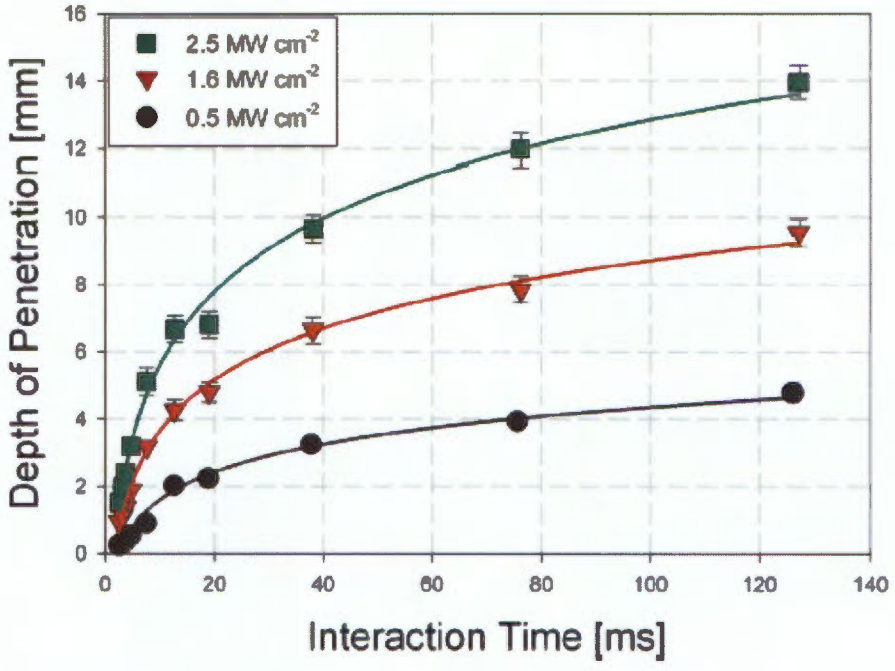

Figure 2.7: Depth of penetration as a function of interaction time and power density for a beam diameter of $0.63mm$ [71].

As shown in Figure 2.7, the slope of the penetration depth is very high at short interaction times. With an increase in interaction time, the slope of the melt depth decreases. The melt depth in a study done by Weckman et al. [13] showed the same dependency on pulse duration, as shown in Figure 2.8. This behaviour can be attributed to the fact that at shorter pulse durations, the absorbed laser energy is greater than the penetrating heat energy [72]. With increasing pulse duration the conduction losses increase and when they equal the amount of absorbed laser energy, the melt depth will reach its maximum.

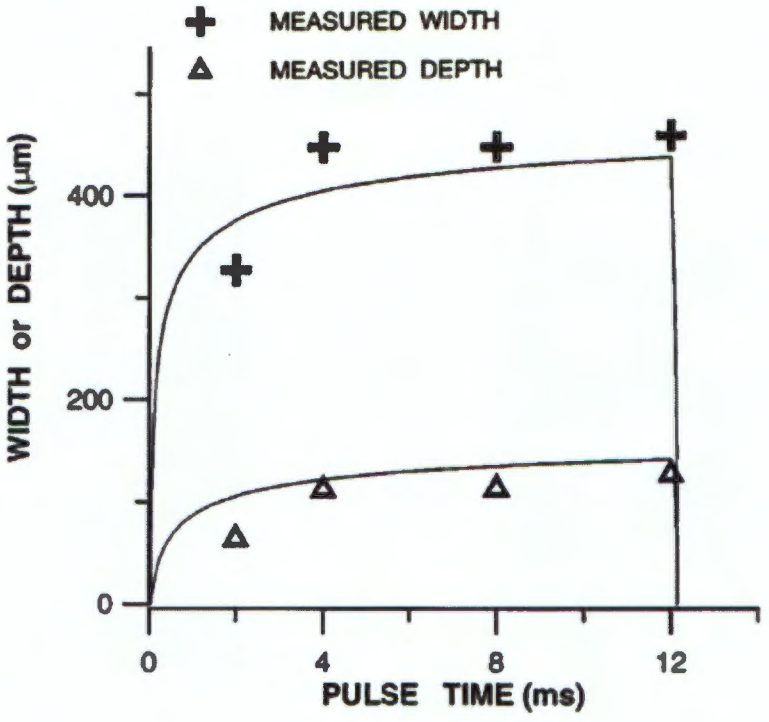

Figure 2.8: Predicted (solid lines) and measured (+ and Δ) weld pool widths and depths vs pulse duration showing a logarithmic dependency of weld pool on pulse duration. AA 1100 welds produced using average power density 6 GW/m^2 and absorptivity of 0.24 [13].

There are cases where the melt depth is predicted to decrease after reaching its maximum with a further increase in pulse duration [72]. Continuing with the theme of energy balance, the decrease in the melt depth occurs when energy losses (conduction and convection) become greater than the absorbed energy. In the case where the absorbed energy is less than the energy losses, that absorbed energy is not sufficient to maintain the elevated temperatures and so the melt depth will decrease [72]. Shown in Figure 2.9 are the spot weld profiles as functions of pulse duration and power density. It is observed that an increase in pulse duration increases the melt depth. For power density 14.51 GW/m^2 in Figure 2.9, the melt depth seems to reach a maximum at pulse duration of 10 ms after which it looks like it starts to decrease. Therefore, Figure 2.9 could validate the melt depth behaviour as a function of pulse duration as predicted by Abd El-Ghany [72]. In the case of keeping the laser power and beam diameter constant and only increasing pulse duration, the pulse energy should decrease with a flat-top pulse shape. The units of power density (W/m^2) suggest that when all parameters are kept constant and only pulse duration is changed, the energy in a pulse should decrease to keep constant the laser power.

Therefore, the decrease in the melt depth with increasing pulse duration for a constant power density as shown in Figure 2.9 is plausible.

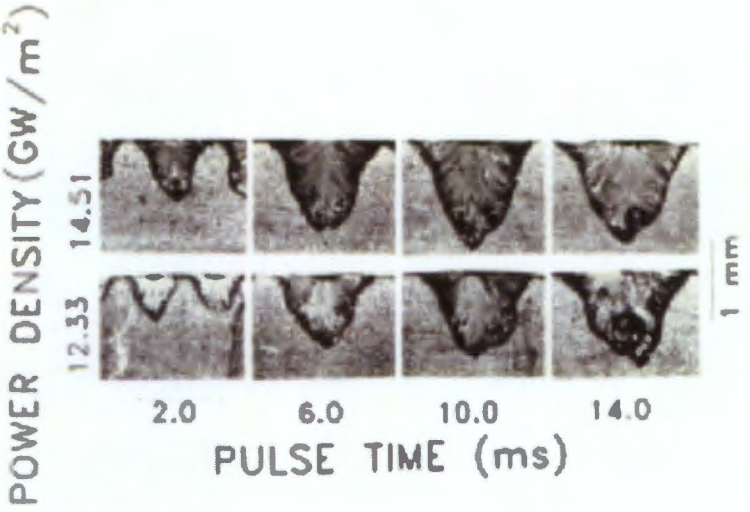

Figure 2.9: Weld pool profiles of AA 1100 aluminium alloy laser spot welds as a function of pulse time and power density [13].

Figure 2.10 is a schematic representation of the effect of increasing pulse duration on the amount of energy carried in a pulse. The energy carried in a pulse influences the amount of energy absorbed by the workpiece. If the pulse energy is high, the amount of energy absorbable will also be high. Since it is said that the pulse energy increases with short pulses, it follows that the amount of absorbed energy increases well beyond that amount lost to conduction and/or convection. Therefore, the melt depth will increase rapidly with short pulses. With an increase in pulse duration, the pulse energy decreases but is still high enough to ensure that the absorbed energy is kept higher than that lost to conduction and/or convection. When the melt depth is approaching its maximum, the rate at which it increases starts to decrease until it reaches its maximum after which it decreases. This could be due to the further decrease in pulse energy with increasing pulse duration. As mentioned already, at the melt depth maximum the energy losses are significant relative to the energy absorbed. A further increase in pulse duration past the melt depth maximum results in the pulse energy being too low to effect temperature increases. Therefore, the melt depth decreases after having had reached a maximum.

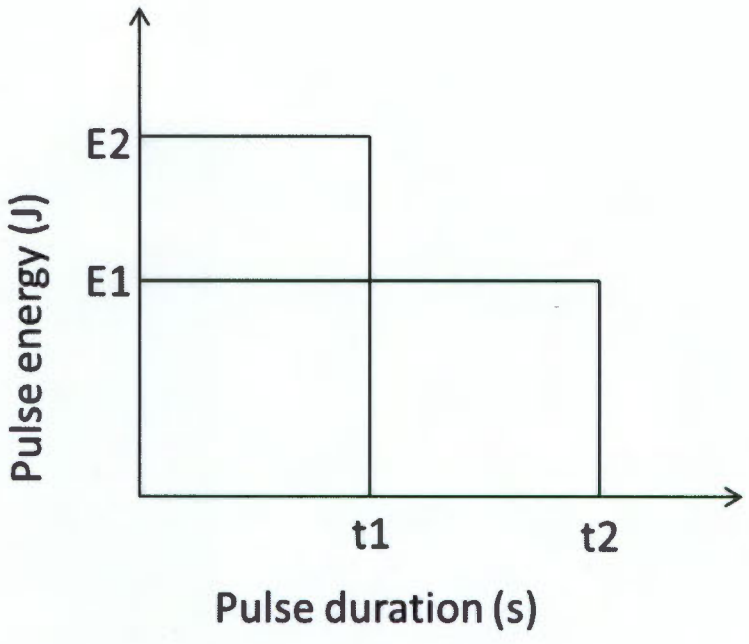

Figure 2.10: Schematic illustration of the effect of increasing pulse duration on the amount of energy carried in a single pulse.

2.3.3 Effect of different combinations of laser parameters on the melt depth

A more meaningful evaluation of the effects of laser parameters on the melt depth is the consideration of the interaction of the laser parameters. It has been shown previously that an increase in laser power increases the melt depth, an increase in beam diameter decreases the power density at the target surface, therefore, decreases the melt depth. It has also been shown that an increase in pulse duration increases the melt depth. The next step is to evaluate the effect of combining these mentioned factors on the melt zone characteristics.

The combination of short pulses and high laser power has been reported to produce deep welds [12, 56]. As mentioned before, during shorter pulses the energy losses (conduction and/or convection) are not significant enough to prevent surface temperatures from reaching the melting point. Therefore, the high laser power will increase the amount of absorbed energy at the irradiation target surface. This leads to the melting of the surface thus propagation of the melt-front into the workpiece. This combination of laser power and pulse duration can lead to surface damage such as crater formation as shown in Figure 2.11.

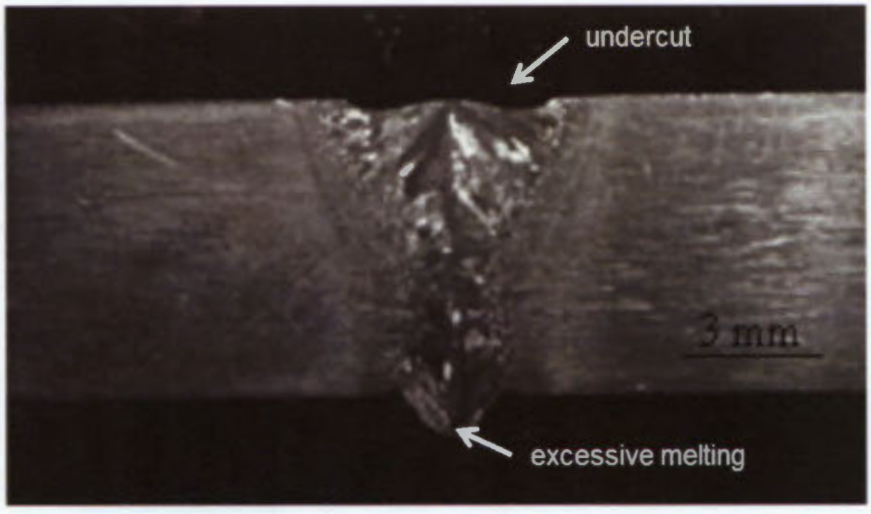

Figure 2.11: Excessive melting and crater/undercut formation due to high laser power and low interaction time [12].

Longer pulses combined with low laser power levels have been reported to produce shallow melt zone with less spattering [56]. The low laser power causes a drop in the amount of energy available for absorption by the workpiece surface. With a decrease in the amount of absorbable energy, surface temperatures are not able to be maintained above melting point thus cannot be maintained at the vaporization point. This then limits the deepening of the melt pool. Also, Weckman et al. [13] showed that for low power densities, near steady-state conditions are reached quicker than for higher power densities. The beam diameter was kept constant in their study, therefore, the previous statement can be rephrased as follows: for low laser power, near steady-state conditions are reached quicker than for higher laser power. A closer look at Figure 2.12 shows that the melt depth seems to decrease with increasing pulse duration as it was also seen in Figure 2.9. This shows that with long pulses and low laser power, shallow melt pools are possible.

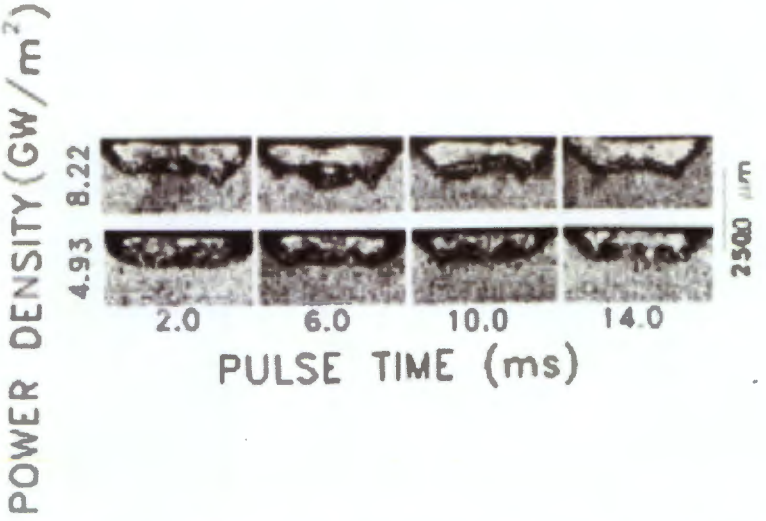

Figure 2.12: Laser spot welds of AA 1100 as a function of power density and pulse duration. Pulse duration has no effect on the melt depth for power densities shown [13].

2.3.4 Defects resulting from a combination of varying laser parameters

This section is included for the benefit of understanding the possible defects that can be found in laser irradiated materials. Furthermore, because this study conducts laser irradiation experiments on titanium samples followed by a microstructural analysis thereof, it was considered appropriate to include this section.

Surface craters/undercuts are defects that are caused by mass loss due to evaporation and/or spattering. Spattering is defined as the molten metal droplets that are thrown out of the melt pool [56]. As mentioned already, this type of damage is caused by short pulses of high laser power.

Unlike craters, weld defects such as porosity and cracking, are not associated with a particular laser parameter. Considering that spattering is caused by increased laser power levels thus high surface temperatures, it follows that spattering can be controlled by reducing laser power or surface temperatures [56]. However, the disadvantage of reducing laser power or surface temperatures is the possibility of reducing the producible melt depth.

There are two causes of porosity. The one is the entrapment of the shielding gas and/or metal vapour in the molten metal [13, 56]. The other cause of porosity is the rapid enclosure of the keyhole [56]. Figure 2.13 is a schematic illustration of how the collapsing of the keyhole can result in porosity. Due to the instability of the keyhole, the molten metal oscillates upwards and downwards the keyhole wall [73]. The upward motion of the molten metal results in the upper wall of the keyhole being convex. This convex profile of the upper keyhole wall produces pressures that induce a downward flow opposite to the upward flow [73]. These opposing flows collide and form an inward protrusion at the keyhole entrance.

With time, the protrusion grows larger and eventually collapses thus closing the keyhole. Therefore, voids are trapped at the bottom of the keyhole as illustrated in Figure 2.13.

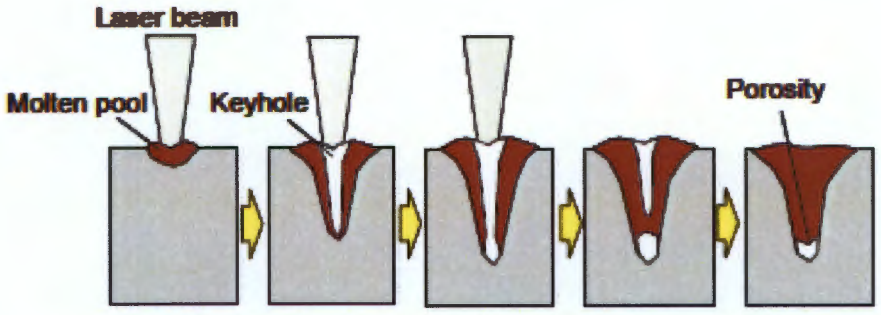

Figure 2.13: Schematic drawing of porosity formation mechanism [64].

With porosity and spattering reviewed, this leaves one more defect associated with laser irradiation of metals. There are three main criteria for crack formation during laser irradiation. The presence of a defect can represent the location of a high stress concentration that can initiate cracking [56]. The high cooling rates associated with laser irradiation can induce high stress states in the melt zone that can often lead to cracking [56]. When one has such high stresses in brittle material such as titanium martensite (α'), cracking can also occur.

The effects of basic laser parameters and those of their combinations have been reviewed. The different defects associated with laser irradiation have been identified as porosity, spattering and cracking. However, only the laser parameters were reviewed. The thermo-physical properties of the workpiece also affect the heat transfer thus affect the melt zone characteristics. The heating and melting of the workpiece surface starts with the absorption of the incident laser beam [74]. This means that the material absorption coefficient plays an important role in initiation of the laser heating and/or melting of the irradiation target surface. A high absorption coefficient will ensure larger amounts of absorbed energy at the irradiation target surface.

2.3.5 Effect of material thermo-physical properties on the melt zone

Even though the amount of absorbed energy is dependent on the absorption coefficient, the surface temperature rise is dependent on the conductivity and heat capacity properties of a material. The conductivity is responsible for the transfer of the absorbed energy to the cooler regions of the irradiated workpiece. The heat capacity can be considered to be the energy-storing ability of the material. It is the stored energy that is used in raising temperatures. Therefore, in the case of having more stored energy than that lost to

conduction, it follows that surface temperatures will be rapidly increased. However, the relatively lower conductivity value will result in shorter heat penetration depths. In a study by Momin et al.[75], temperature profiles existing in titanium and steel during laser heating, were measured. According to their results, titanium exhibited higher peak temperatures than those of steel. They explain the difference in peak temperatures by claiming that the thermal diffusivity of titanium is lower than that of steel [75]. Figure 2.14 (a) shows the thermophysical properties of both titanium and steel as a function of temperature. Thermal diffusivity,α, is the ratio of conductivity, k, to the volumetric heat capacity,$c_p\rho$ (product of heat capacity, c_p,and density ρ), which is represented as $\alpha = k/c_p\rho$. Therefore, a relatively low thermal diffusivity suggests that the heat capacity of the material is higher than its conduction rate, resulting in increased surface temperatures. However, as shown in Figure 2.14 (b) the thermal diffusivity of titanium in not lower than that of steel. This contradicts the explanation given by Momin et al. [75]. Since the absorption coefficient of the steel used in their study was not given, the absorption coefficient of stainless steel is used instead (0.27), as reported by He et al. [76]. The absorption coefficient of stainless steel is lower than that of titanium which is reported to be 0.443 [77]. The high absorption coefficient of titanium could be the reason for its higher peak temperatures when compared with steel. In general, the higher the absorption coefficient and the lower the thermal conductivity, the greater the melt depth [78].

(a)

Titanium	Temp (K)	300	400	500	600	800	1200	2000
	k W/mK	21.9	20.4	19.7	19.4	19.7	22.2	28.7
Titanium	Temp (K)	293	373	473	673	873	1073	1958
	ρ kg/m^3	4500	4490	4478	4452	4425	4397	4130
	C_p J/kg K	519	540	569	619	636	682	700
Steel	Temp (K)	298	373	473	673	873	1073	
	ρ kg/m^3	7920	7893	7851	7765	7673	7579	
Steel	Temp (K)	200	400	600	800	1000	1200	1500
	k W/mK	12.6	16.6	19.8	22.6	25.4	28.0	31.7
	C_p J/kg K	402	515	557	582	611	640	682

(b)

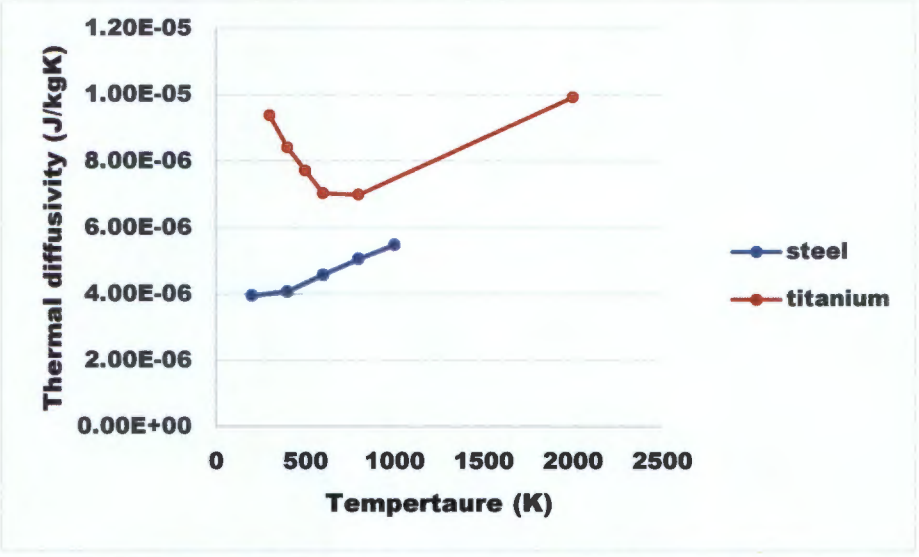

Figure 2.14: a) Thermophysical properties of titanium and steel as a function of temperature as extracted from the work of Momin et al. [75] and b) calculated thermal diffusivities of titanium steel as a function temperature.

2.4 Analytical approach towards thermal process analysis

In almost all cases where lasers are used, melting of a material occurs. It is appreciated that there are circumstances where melting is not required. Therefore, it is of great interest to have the knowledge of how to control the melting process or how to avoid it. Having knowledge of how to control thermal processes is necessary to achieve high quality materials processing. When a laser beam is irradiated on a material surface, a portion of the laser energy is absorbed and conducted into the interior of the material [10]. Should the deposited energy be high enough, the targeted surface will melt and the melt-front propagation into the interior of the work-piece will begin.

Analytical predictions of thermal processes allow a process operator the advantage of being able to easily optimize the process before it even begins. Therefore, the outcome of the

thermal process can be predicted without leaving much to surprise. This has a positive effect on the time taken to optimize a thermal process by eliminating much of the trial-and-error method of trying to achieve optimum process parameters. However, the main disadvantage with theoretical analyses is that the studies are often (if not always) based on assumptions. These assumptions make the modelling of thermal processes manageable. Otherwise, modelling becomes too complex to comprehend. However, the disadvantage of using assumptions in modelling is the error introduced in calculations. Because of the many assumptions possible, only some of the common ones are discussed.

2.4.1 The exclusion of latent heat of fusion

For the ease of implementation, some analytical solutions of the thermal conduction process exclude the effects of latent heat [2, 11, 79]. Latent heat is understood to be heat that is absorbed or released during a material phase change. In processes where solid-solid transformations are expected to occur, latent heat has been regarded to be negligible thus omitted from the analytical solutions [79]. However, in processes where solid-liquid phase transformations occur, latent heat is expected to have a significant effect on the analytical solution. Karkhin [79] points out that aluminium alloys can have latent heat of fusion as much as forty percent (40%) of the energy required to bring the material to its melting point. Therefore, omitting latent heat from the analytical solution in this case, would translate in approximately 40% reduction/increase of the total absorbed energy not being accounted for. This would expectedly introduce significant errors.

An interesting aspect of latent heat is the effect it has on the temperature profile inside the material. Latent heat of fusion is understood to be the energy that is required by the material for its phase transformation from solid to liquid. Therefore, its effects are expected to be seen at the melting temperature. Garai [80] even mentions in his work, that latent heat of fusion is absorbed by the material at a constant temperature when the solid-liquid phase transformation occurs. In addition, since this type of transformation occurs at the melting point (for materials with distinct melting points), it makes sense that the constant temperature that Garai [80] is referring to, is the melting temperature. Despite the above considerations, some published temperature profiles that are claimed to have been derived from calculations that considered latent heat, do not exhibit the effects of latent heat. For instance, the reader is referred to Figures 2.15 and 2.16. Note that the temperature profile expected (when considering latent heat) by Tokarev and Kaplan [14] in Figure 2.15 exhibits a distance along the depth of the material where temperature is constant. From this figure, that constant temperature is labelled as the melting temperature. This ties in well with the expectations of the author. However, the temperature profile by Shen et al. [15] in Figure

2.16 does not show temperature remaining constant at the melting point. Instead, the melting point is characterized by a point of inflection in the graph.

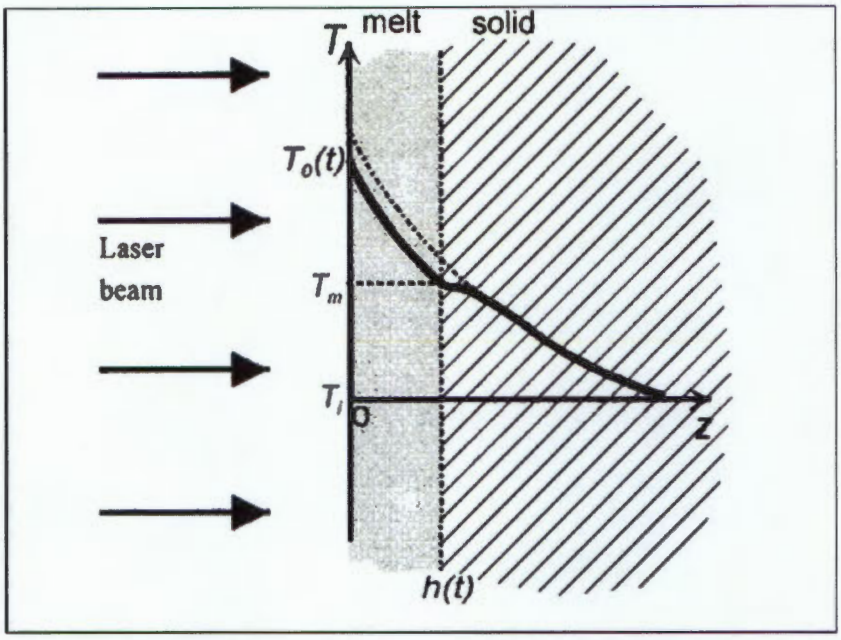

Figure 2.15: Temperature distribution inside a material with (solid line) and without (dotted line) consideration of latent heat as expected by Tokarev and Kaplan [14].

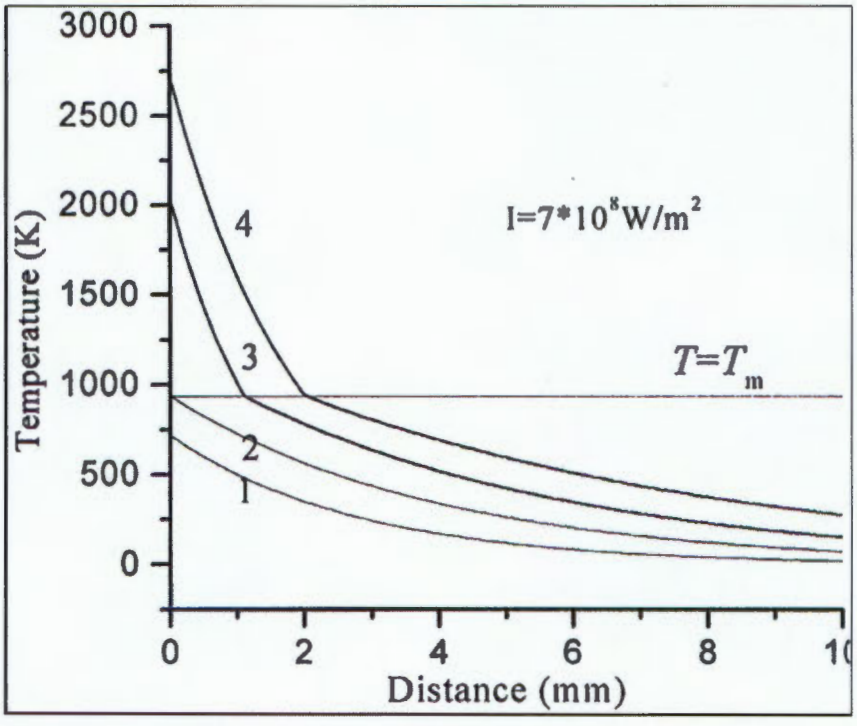

Figure 2.16: Temperature profile inside aluminium. Curves 1, 2, 3 and 4 correspond to 40, 80, 100 and 120 ms [15]

Two reasons come to mind as to why this difference exists between Figures 2.15 and 2.16. The first one has to do with the kind of material used. With non-crystalline solids, latent heat is not required for a solid-liquid transformation, since they do not have a well-defined melting temperature [80]. The second one involves the graphical visibility range. The distance/layer where temperatures remain constant at the melting point could be too small to be picked up on the current x-axis scale used in Figure 2.16. Therefore, perhaps upon zooming in on the graph, that distance over which temperature is constant will be shown more clearly. The first reason is not possible because the material used in Figure 2.16 is aluminium which is crystalline. That leaves the second reason as a possibility.

2.4.2 Temperature independency of thermophysical properties

The assumption that thermophysical properties are constant is one that is widely used. Density, thermal conductivity, heat capacity and absorptivity are properties known to be temperature-dependent. However, for the ease of implementation these properties are assumed to be independent of temperature.

The works of Yillbas and Shunja [11], Xie and Kar [10] and Shen et al. [15] are just a few of many that employ the assumption that thermophysical properties are constant. Figure 2.17 shows the results obtained by Refs. [10, 11, 15]. Each Ref. approached the heat flow problem differently to the others. Therefore, the plots in Figure 2.17 may not necessarily be comparable. The authors of Figure 2.17 (a) derived two analytical solutions which were compared with experimental data. The authors of Figure 2.17 (b) derived only one solution which they compared with their experimental data. Similarly, the authors of Figure 2.17 (c) compared one solution against experimental data.

In Figures 2.17 (a) and (b), the authors plotted melt depth against time whilst in Figure 2.17 (c), it is the dimensionless temperature plotted against dimensionless time. The lack of similarity in the three plots is of no concern to the author. The purpose of Figure 2.17 is to show the effects on analytical results, of assuming that thermophysical properties are independent of temperature. In all three plots, the analytical results are compared with experimental results. Both Refs. [10, 15] acknowledge that their results are not exact replicas of the experimental results, as shown in Figures 2.17 (a) and (b). However, they conclude that there is a reasonably good agreement between their theoretical results and the experimental results. Furthermore, they seem not to owe the lack of total agreement between their two sets of results (theoretical and experimental) to the assumption that thermophysical properties are temperature independent. However, the results of Yilbas and Shuja [11] in Figure 2.17 (c) show the best possible agreement with experimental data.

These results show that keeping thermophysical properties constant might not introduce large calculation errors.

a

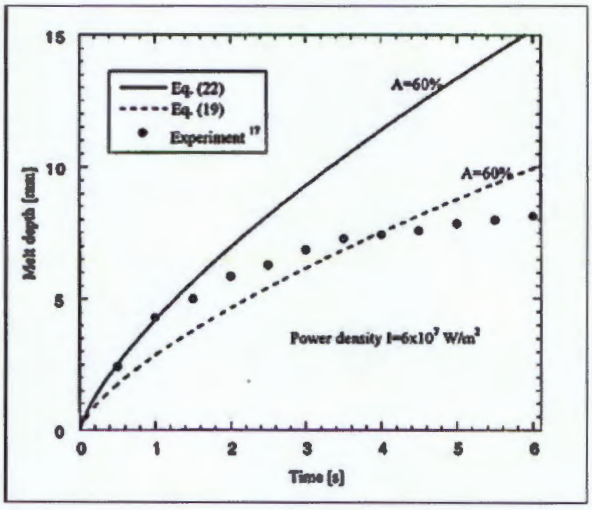

b

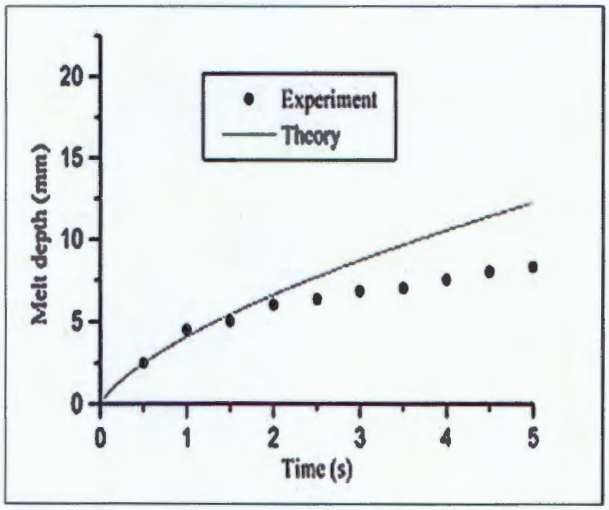

c

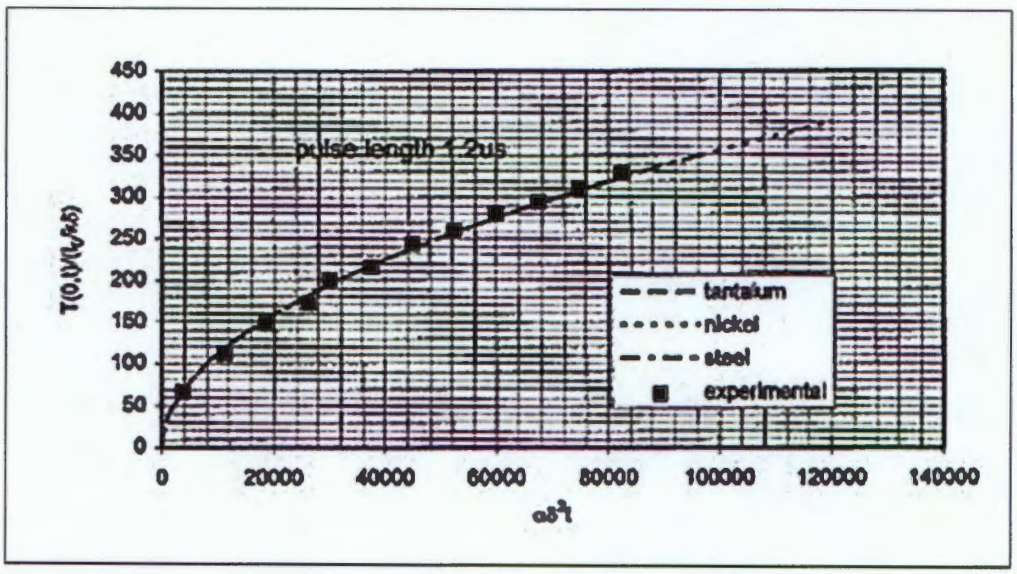

Figure 2.17: Illustration of the agreement of theoretical results with experimental data: (a) Melt depth variation for fused quartz [10]; (b) Melt depth evolution of fused quartz [15] and (c) Variation of dimensionless surface temperature $T(0,t)/(I_0/k\delta)$ with dimensionless time $(\alpha\delta^2 t)$ [11].

2.4.3 The neglect of vapour and plasma effects

The blight flame that is generated when a laser beam is incident on a target is called laser induced plasma. It is known to disturb the deliverance of the laser beam on to the surface of

the target [10, 15, 81]. It does this by absorbing a part of the incident energy. It is believed that this phenomenon, known as plasma absorption, is attributed to the fact that the plasma is not a perfect transparent medium [81].

The work on the interaction of the laser beam with plasma done by Matsunawa et al. [81, 82], has shown that a part of the laser beam energy is absorbed and another scattered. From the plasma absorption aspect, Matsunawa and Ohnawa [81] found that six percent (6%) of the incident beam was absorbed whilst the beam propagated through a specified length of the plasma. Their suspicion of some of the laser beam energy being scattered was brought on by the finding that the titanium target (sample in their study) only absorbed about fifty percent (50%) of the laser beam energy. In addition, the energy absorbed by the plasma was about thirty (30%) to forty percent (40%). Therefore, the rest had to be dissipated through another mechanism which they suspected to be laser beam scattering. The work of Matsunawa et al. [81, 82] validates the possibility of the claims made in Refs. [10, 15] that the lack of total agreement between the predictions and the experimental results was due to the plasma absorption of the incident beam energy.

2.5 Comparison of the analytical and experimental results

Besides temperature profiles, the HAZ and melt depth are two phenomena in laser heating that are greatly studied [10, 15, 61, 83, 84]. Some studies are analytically based [10, 15, 83] whilst others are experimental [61, 84]. Similar to the current work, other models also utilise assumptions to simplify the nature of the heat transfer problem. Therefore, comparing theoretical data against other theoretical data leaves room for misleading errors.

It is mentioned as a reminder that the model developed in this work assumes a stationary laser beam. In light of the reminder, only data obtained from experiments where both the workpiece and the laser beam are stationary are considered for comparative purposes. An example of such a process that has both the workpiece and the laser beam stationary is laser spot welding. Due to a lack in reported data on laser spot welding of titanium, the comparative study makes use of laser spot welding data of other materials. Figure 2.18 is a comparison of the laser spot welding results obtained by He et al. [76] in their study of heat transfer and fluid flow during laser spot welding of 304 stainless steel and the calculated results thereof. From Figure 2.18, it seems that the calculated results of He et al. [76] are in close agreement with their experimental results. However, both the calculated and the experimental results have a 'chainsaw teeth' pattern. With an increase in the power density the melt depth/weld pool depth seems to alternate between increasing and decreasing. Considering that the reason for this behaviour is not mentioned in the report by He et al. it follows that one is left to their own interpretation. Given that He et al. [76] did not provide the laser parameter combinations used in their study, the trends in Figure 2.18 could be

explained by a possible variation in pulse duration ($4\ ms\ and\ 3\ ms$) within the same plot. That is, the results by He et al. [76] are not represented by one pulse duration value. This is a possible explanation as to why the melt depth alternates between increasing and decreasing with increasing laser intensity. For example, the data points at $I = 2200\ and\ 2300 W/mm^2$ have similar power densities and yet have different melt depths. However, the data point at $I = 3200\ W/mm^2$ has a different power density to $I = 2200\ or\ 2300\ W/mm^2$ and yet has a similar melt depth to that at $I = 2300\ W/mm^2$.

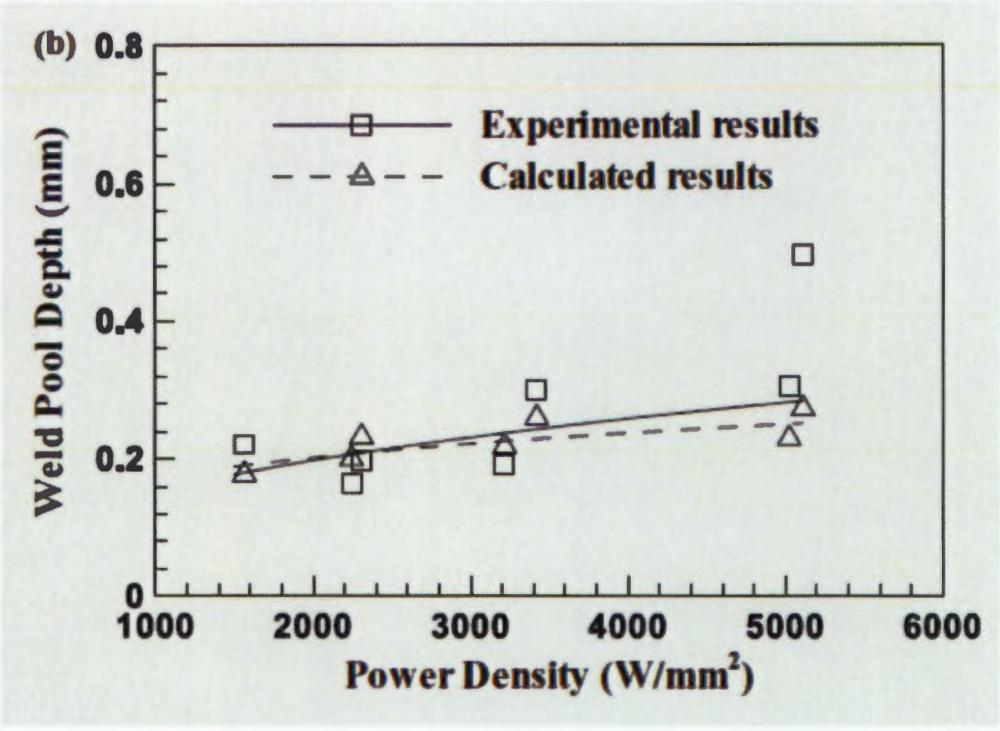

Figure 2.18: A comparison of the calculated and experimental results of the effects of laser intensity on the melt depth. A beam diameter and pulse duration of 428μm and 3ms are assumed [76].

Chang and Na [63] conducted single-pulsed spot welding experiments to validate their predictions. Figure 2.19 is a comparison of their theoretical with experimental results. There is a correlation between the theoretical and experimental results. The observed trend in Figure 2.19 is that the melt depth increases with increasing laser beam energy. This is expected since an increase in laser beam energy (whilst pulse duration is constant) is synonymous with increasing laser beam power which, in previous sections has been reported to be directly proportional to the melt depth.

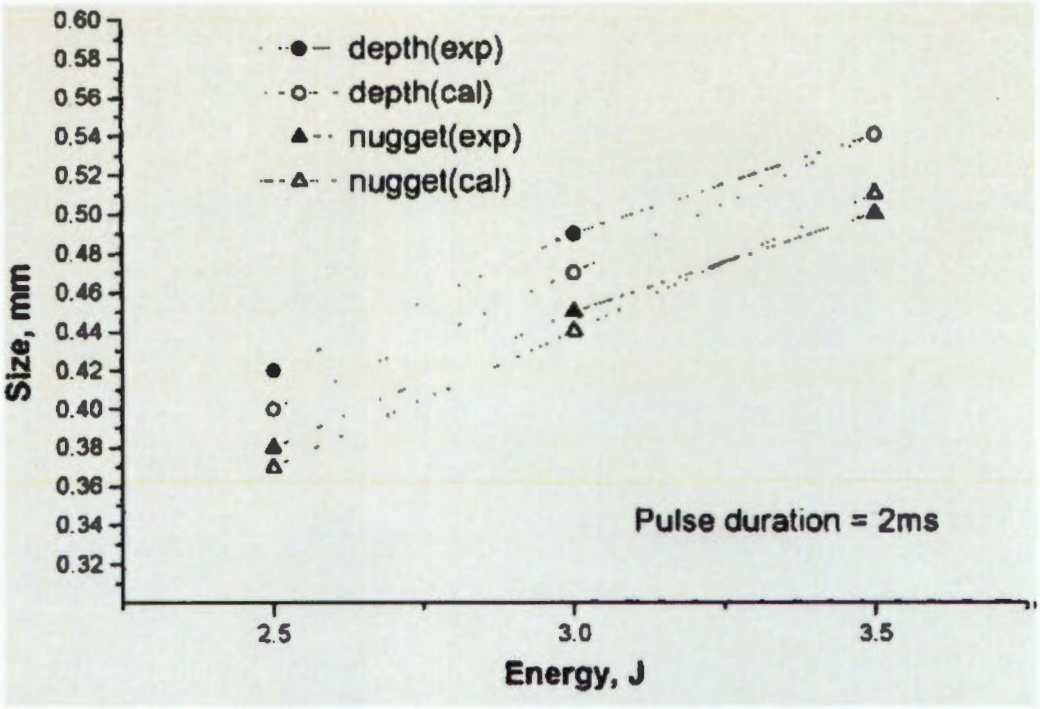

Figure 2.19: Comparison of numerical results and experimental results of laser spot welding of stainless steel conducted by Chang and Na [63].

In a study of laser process variables on laser spot welds, Weckman et al. [13] successfully showed that an increase in pulse duration increases the melt depth. Shown in Figure 2.20 is a comparison of their theoretical results with their experimental results. The comparison reveals that there is a good correlation between the two sets of results.

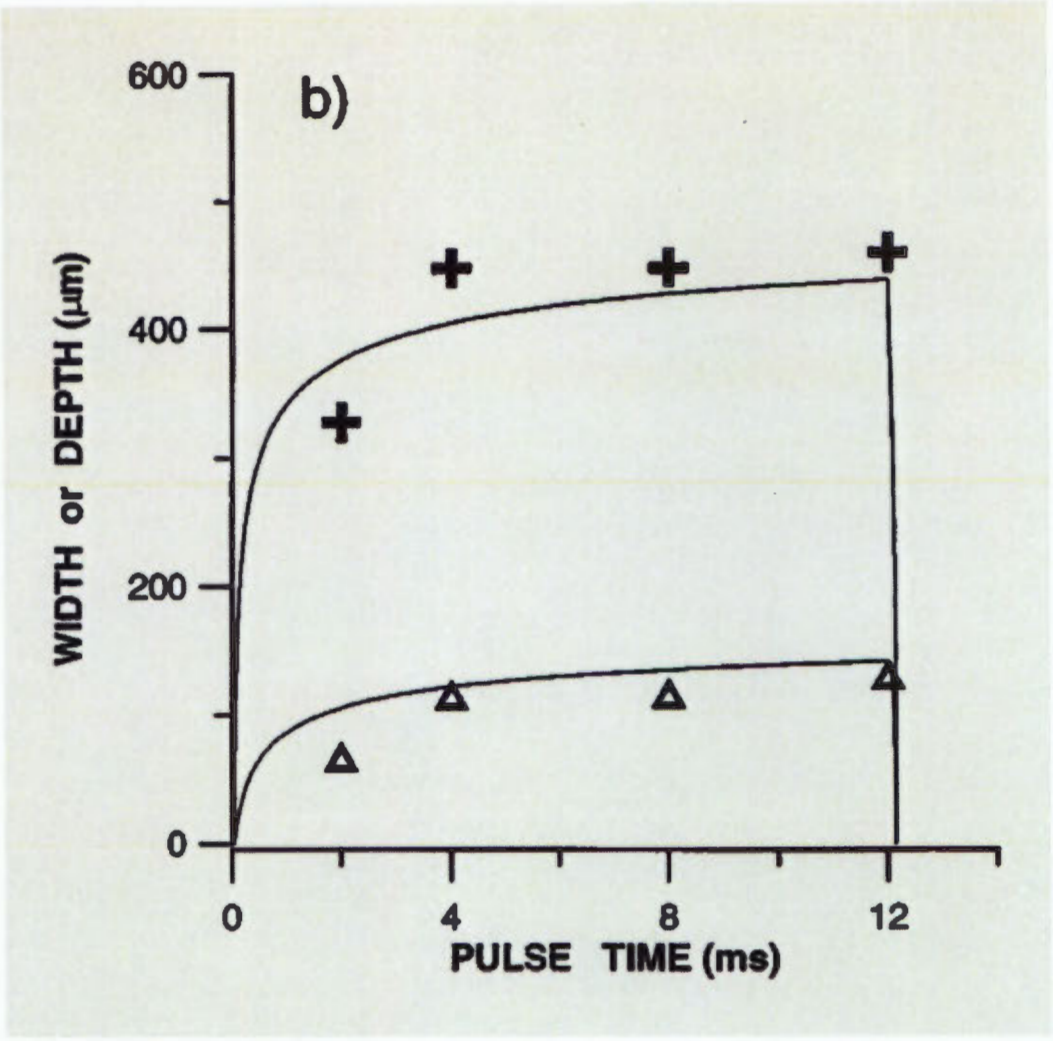

Figure 2.20: Comparison between predicted (+) and measured (Δ) melt depths and widths of AA100 laser spot welds by Weckman et al. [13].

With similar success, Frewin and Scott [85] developed a three-dimensional finite element model of the heat flow during pulsed laser welding. Their model was successfully applied to spot welds on mild steel. Figure 2.21 is a comparison of their experimental results with their numerical results. It can be seen that their predicted weld and fusion zone depths are in excellent correlation with the experimental measurements over a focal point range of -6mm (6mm into the workpiece) to 6mm (6mm above the workpiece surface). Frewin and Scott [85] found that two of the most sensitive inputs to their model were the shape of the laser beam intensity profile and the absorptivity of the beam at the surface of the workpiece.

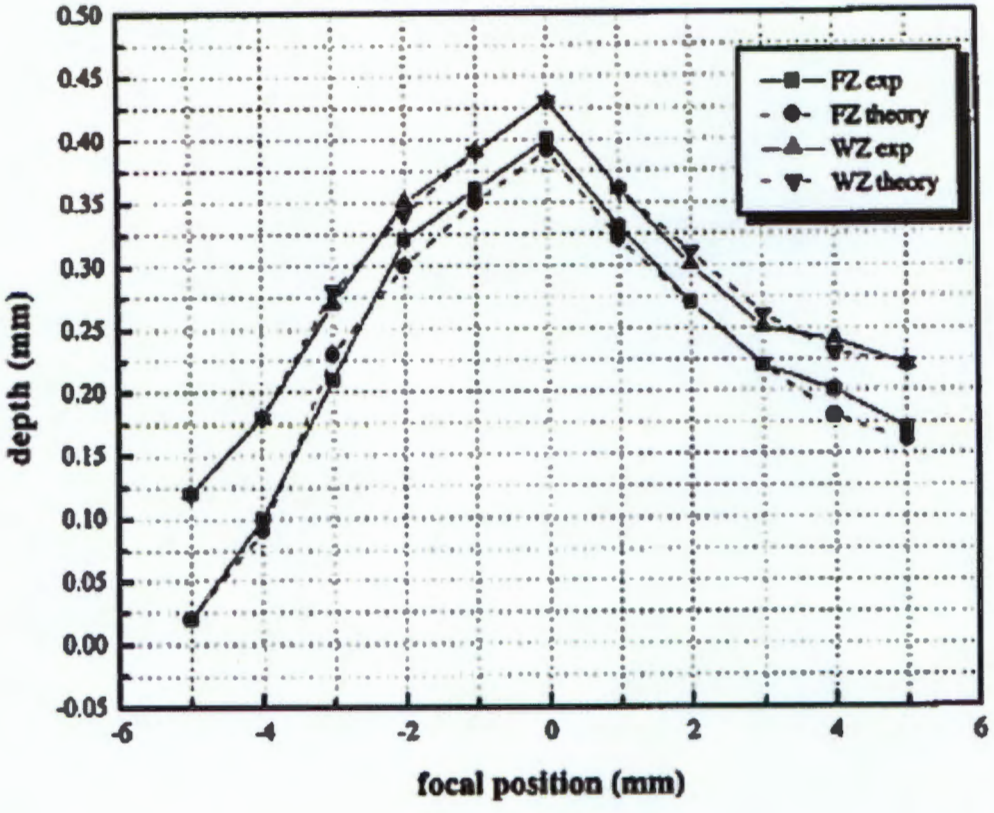

Figure 2.21: Measured fusion and weld zone (FZ and WZ respectively) depths compared with model predictions based on changing absorptivity [85].

Although it was only a handful of studies found to conduct both theoretical and experimental investigations of laser spot welding, it has been shown that it is possible to obtain a close correlation between theoretical and experimental results.

2.6 Summary of presented background and problem statements

Titanium is a material that is commonly subjected to laser surface modifications and laser welding processes that involve melting the material. There have been studies dedicated to investigating the effects of laser parameters on the outcome of the aforementioned laser processes [5, 43, 58, 59]. More relevant to this study are the effects of laser parameters on the evolution of the melt depth during laser irradiation. In their investigations, different researchers have employed different approaches to mathematically solve the heat transfer problem and understand the influence that each laser processing parameter has on the outcome. He et al. [76] employed a three-dimensional transient heat transfer and fluid flow model to calculate temperature profiles and melt depths. Their model took into consideration the Marangoni forces resulting from the spatial gradient of surface tension. Similarly, the

model employed by Chang and Na [63] to simulate pulsed laser spot welding processes treated the heat transfer problem as a three-dimensional problem. However, because Chang and Na [63] considered temperature-dependent parameters, their nonlinear parabolic differential equation for heat diffusion was solved numerically. Frewin and Scott [85] developed a three-dimensional finite element model by solving the energy balance equation and employing temperature-dependent variables. It is worth noting that Frewin and Scott [85] improved the accuracy of their results (shown in Figure 2.21) by utilizing measured beam intensity profile instead of assuming a profile (line, Gaussian or top-hat profile).

The abovementioned models utilize complex mathematics which would require a certain level of a specialised skill. Simpler models that utilize basic mathematics have been employed by the likes of He et al. [76], Xie and Kar [10] and Shen et al. [15]. In developing these simpler models, numerous assumptions are made thus having a negative effect on the accuracy of the model. Treating the heat transfer problem during laser irradiation as a one-dimensional problem, only considering conduction as the only heat transfer mode, considering the heat flow as being in one direction, are some of the critical assumptions that are made in developing simpler models. These simplified models have been reported to predict melt depths that are in good correlation with the experimental melt depths [10, 15]. However, it has also been reported that the predicted melt depths overestimate the experimental results with increasing pulse duration and laser power [10, 15]. Therefore there should also be the consideration of the error introduced by the simplification of the heat transfer problem.

The current study adapts the aforementioned simpler models to approximate the melt depth inside a laser irradiated titanium sample. The irradiation period (pulse duration) is considered to be a single pulse. Furthermore, the study assesses the error with which the adapted model approximates the melt depth measurements.

2.7 Research questions

With analytical models already developed by other researchers, the following questions form the basis of this research:

- Within this research project's region of interest for surface modification of titanium, can existing analytical approaches presented by refs [10, 11, 14, 15] be simplified even further to approximate the resulting melt depth post a single laser pulse?
- How large is the error introduced by this simplification, compared to the aforementioned analytical results and the experimental data of this research project?

2.8 Research objectives

In answering the posed research questions, the objectives of this study are therefore to

- Adapt a mathematical model for predicted temperature profiles and isothermal depths at the end of a single laser pulse.
- Assess the error introduced by the use of the adapted model.

2.9 Research scope and methodology

As already mentioned, there are analytical models that have been developed by other researchers [10, 11, 14, 15]. These analytical models were adapted in the current work with a few deviations. In the analytical approach, only the onset of melting was considered because it is the evolution of the melt depth that the study is interested in. Therefore at the onset of melting, the laser irradiated titanium sample is considered to be in its solid phase. At any given time post the onset of melting the titanium sample is considered to have two phases, liquid and solid. The condition equations used in order to arrive at the melt depth profiles as well as temperature profiles which are predicted to exist in the respective phases, were obtained from the works of Xie and Kar [10], Shen et al. [15].

In order to simplify the heat transfer equations the following assumptions were made [10, 11, 14, 15]:

- The heat transfer problem is one dimensional, thus the laser beam diameter encapsulates the entire molten surface
- The target is semi-infinite thus $x \rightarrow \infty$.
- The conduction and convection losses are neglected.
- The thermophysical properties of the target are independent of temperature.
- The laser beam delivers constant and uniform energy density
- Vaporization and its effects are ignored

The resulting profiles were modelled in MATLAB Student version, Microsoft Excel 2010 and Mathematica version 8.0.4 software packages. From the derived melt depth equation the isothermal depth equation was derived. This isothermal equation was used to determine the depth to which temperature-associated phase transformations occur inside titanium at the end of a single laser pulse.

To compare analytical results with the experimental results, the thermo-physical properties of titanium and the laser parameters used in the experiments were fed into the model.

In order to validate the developed profiles, laser spot irradiation was carried out on titanium (CP) samples. Laser power and pulse duration were varied during the laser spot irradiation experiments. Cross-sections of the irradiated titanium samples were prepared for microstructural analysis using the standard method, involving cross-sectioning the samples

using a diamond-blade cutter, and then grinding the cross-sectional surfaces; this was then followed by cleaning, polishing and etching of the cross-sectional surfaces. The etching reagent used was the Keller's reagent. The analysis of the cross-sections was carried out through the use of optical and light microscopy. An assumption made in this analysis was that the cross-sections were precisely through the middle of the weld surface diameter. Some of the melt zones were too small in diameter to accurately cut through the middle of the melt zone. Therefore, the limitation encountered was that the measured characteristic depths (melt depths) were not always the true maximum of the melt zone.

2.10 Project limitations

The only limitation encountered was the inability to measure the temperatures inside the titanium samples during laser irradiation. The equipment available during this investigation did not allow for the measurement of the vertical or horizontal temperature distributions with sufficient accuracy and in a repeatable manner. However, through the ability to physically measure the characteristic depths (i.e. melt and beta phase transformation depths) post laser irradiation, model verification was carried out by comparing the calculated depths to those measured.

This report begins with a review of the literature relevant to the current study. The review is followed by Chapter 3 presents the analytical and experimental approaches taken in this study. Chapter 4 is comprised of the theoretical and experimental results also including the comparison between the two sets of results. The experimental results include both the macrostructural (shape, size and defects observed in welds) and the microstructural results. Conclusions on the presented work are drawn in Chapter 5 followed by recommendations.

3 APPROACH AND METHODOLOGY

This chapter presents the research methodologies that were utilized in order to carry out the set-out objectives.

The analytical model developed is based on initial-, boundary- and interface- boundary conditions and assumptions for simplifying the heat transfer problem. From the adapted model, temperature profiles (in the liquid and solid phases) and melt depths were modelled in MATLAB Student version, Microsoft Excel 2010 and Mathematica version 8.0.4 software packages. From the derived melt depth equation the isothermal depth equation was derived. This isothermal equation is to determine the depth to which temperature-associated phase transformations occur inside titanium at the end of a single laser pulse. To compare analytical results with the experimental results, the thermophysical properties of titanium and the laser parameters used in the experiments were fed into the model.

In order to validate the adapted profiles, laser spot irradiation was carried out on titanium (CP) samples. Laser power and pulse duration were varied during the laser spot irradiation experiments. Cross-sections of the irradiated titanium samples were prepared for microstructural analysis using the standard method. The standard method involves cross-sectioning the samples using a diamond-blade cutter, and then grinding the cross-sectional surfaces, this is then followed by cleaning, polishing and etching of the cross-sectional surfaces. The etching reagent used was the Keller's reagent. The analysis of the cross-sections was done through the use of optical and light microscopy. An assumption made in this analysis was that the cross-sections were precisely through the middle of the weld surface diameter. Some of the welds were too small in diameter to accurately cut through the middle of the weld. Therefore, the limitation encountered was that the measured characteristic depths (melt depths) were not always the true maximum of the weld.

3.1 Analytical approximation of melting during laser irradiation

3.1.1 Problem Definition

Figure 3.1 is a schematic representation of the heat transfer problem describing the solid-to-liquid phase change during laser irradiation. In the case of Figure 3.1, a laser beam is shone onto the surface of a target. With sufficient energy absorption, the surface, $x = 0$, begins to melt thus creating two phases. Phase 1 represents the liquid phase and Phase 2 the solid phase.

Since the current work is interested in approximating the melt depth during laser irradiation, the period before melting is ignored. Therefore, τ_m will represent the time at which the surface starts melting and will also represent the initial condition used in the current theory. That is, the initial condition for the current work will be when the surface $x = 0$ starts to melt when $\tau = \tau_m$, thus having the surface temperature equal to the melting temperature (i.e. $T(0, \tau_m) = T_m$). The variables τ_m and T_m are time at which melting occurs and melting temperature of the irradiation target, respectively.

With continued laser irradiation beyond τ_m, the surface temperature increases beyond the target's melting temperature. Consequently, the phase boundary $X(\tau)$ moves from the surface further into the target, thus increasing the liquid region at the expense of the solid region. It is this phase boundary that the current work aims to develop an approximating equation for.

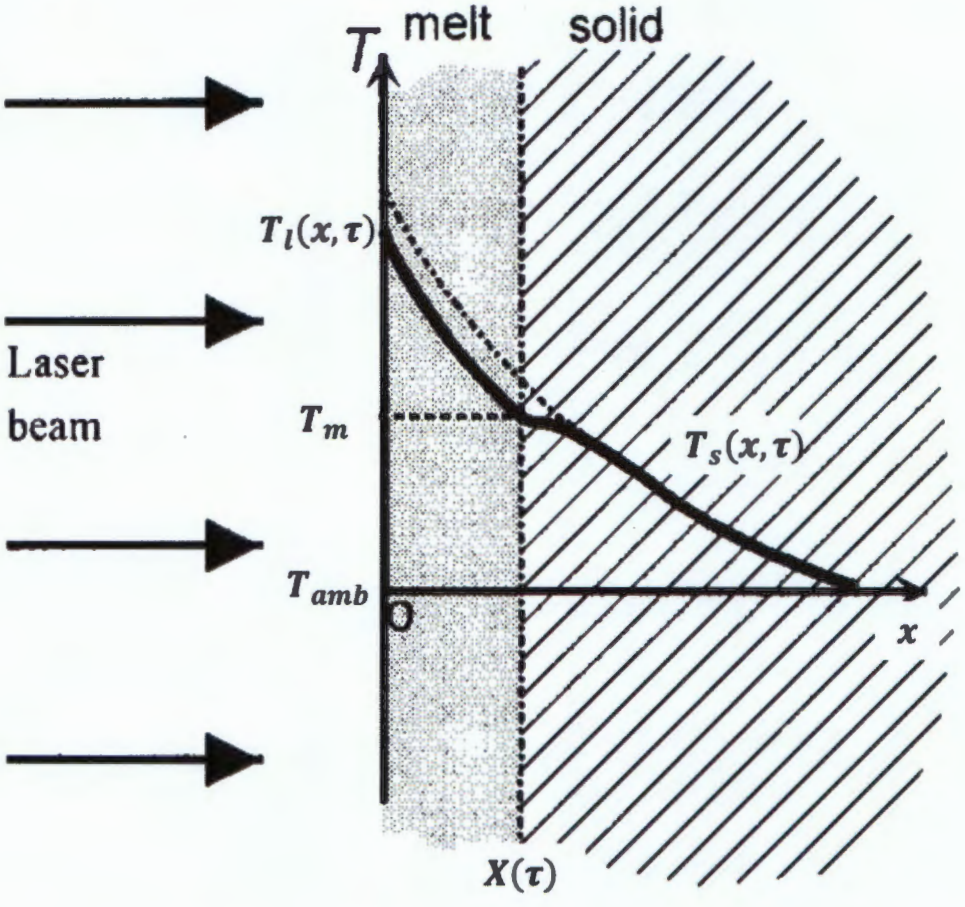

Figure 3.1: Schematic diagram of the heat transfer problem describing melting during laser irradiation of a target.

The following equations mathematically describe the heat transfer problem as illustrated in Figure 3.1:

$$\frac{\partial^2 T_l(x,\tau)}{\partial x^2} - \frac{1}{\alpha_l}\frac{\partial T_l(x,\tau)}{\partial \tau} = 0, \qquad 0 < x < X(\tau) \tag{3.1}$$

$$\frac{\partial^2 T_s(x,\tau)}{\partial x^2} - \frac{1}{\alpha_s}\frac{\partial T_s(x,\tau)}{\partial \tau} = 0, \qquad X(\tau) < x < \infty \tag{3.2}$$

$$T_l(x,\tau) = T_s(x,\tau) = T_m, \qquad x = X(\tau) \tag{3.3}$$

$$k_l\frac{\partial T_l(x,\tau)}{\partial x} = k_s\frac{\partial T_s(x,\tau)}{\partial x} - \rho L\frac{dX(\tau)}{d\tau}, \quad x = X(\tau) \tag{3.4}$$

$$-k_l\frac{\partial T_l(x,\tau)}{\partial x} = AI, \qquad x = 0 \tag{3.5}$$

$$T_s(x,\tau = 0) = T_{amb}, \qquad x \to \infty \tag{3.6}$$

$$X(\tau) = 0, \qquad \tau = 0 \tag{3.7}$$

In the above, T_i, α_i and k_i represent the temperature, thermal diffusivity and thermal conductivity of the respective phase according to $i = l$ and $i = s$. Here, l and s represent the liquid and solid phases, respectively. Also, T_{amb} represents the ambient temperature.

To be able to simplify the heat transfer problem, the following assumptions were made:

- The heat transfer problem is one dimensional, thus the laser beam diameter encapsulates the entire molten surface.
- The target is semi-infinite thus $x \to \infty$.
- The conduction and convection losses are neglected.
- The thermophysical properties of the target are independent of temperature.
- The laser beam delivers constant and uniform energy density.
- Vaporization and its effects are ignored.

The mathematical description of the heat transfer problem in Figure 3.1 has been used by other researchers as well [10, 15, 86]. However, the approach to deriving a solution to Equations (3.1) – (3.7) can vary from one researcher to the next.

From Equations (3.1) – (3.7), it can be said that the heat transfer problem is described by linear homogeneous partial differential equations subjected to nonhomogeneous boundary conditions. A common method of solving the heat differential equation is the Separation of Variables method [87]. This method relies upon the assumption that a function of the form,

$$T(x,\tau) = \varphi(\tau)G(x), \tag{3.8}$$

will be the solution to the linear homogeneous differential equation (Equations (3.1) and (3.2)). In addition to satisfying the linear homogeneous differential equation, Equation (3.8)

needs to satisfy the boundary conditions (Equations (3.3) – (3.6)). Provided that the boundary conditions are also linear and homogeneous, they can be satisfied by a solution in the form of Equation (3.8) [88]. This is considered as a limitation because boundary conditions are not always linear and homogeneous.

Depending on the purpose of a study, different researchers choose to deal with this limitation in their own way. El-Adawi and Elshehawey [89] chose to manipulate their conditions, by transforming their linear homogeneous differential equation, into a nonhomogeneous equation subjected to homogeneous boundary conditions. Due to the nonlinearity of the condition in Equation (3.4), elementary methods such as Separation of Variables method fail [90]. Therefore, researchers turn to laborious numerical methods [91]. Others opt to obtain approximate solutions to modified problems that are expected, on physical grounds, to represent the actual situation quite closely [10, 15, 86].

In their approach to determine the approximate solution to the heat transfer problem, Sharma et al. [86], Shen et al. [15], Xie and Kar [10] utilize an arbitrary temperature profile that satisfies the differential equations only at the bounds, $x = 0$ and $x = X(\tau)$. Both references [10, 86] reported that this type of approximation provides temperature profiles at the boundary within 20% of the correct value.

In a slightly similar manner, the melt depth is approximated in this work. In order to develop an equation for melt depth, the temperature profile has to be determined first. Because of the difficulty of analytically determining a temperature profile that satisfies all conditions in Equations (3.1) – (3.7), the temperature is also approximated.

3.1.2 *Derivation of the approximate solution*

Since it is the approximate temperature that is to be derived, the boundary-, interface- and initial conditions in Equations (3.1) – (3.7) can no longer be satisfied in their entirety. They are satisfied only at the boundaries. Therefore, the following are conditions that are satisfied by the approximate solution. The reader will note that the governing heat equations are not included in the conditions to be satisfied by the approximate solution. This is due to approximating a solution that only satisfies the heat conditions at the boundaries.

$$T_l(x,\tau) = T_s(x,\tau) = T_m, \qquad x = X(\tau) \tag{3.9}$$

$$k_l \frac{\partial T_l(x,\tau)}{\partial x} = k_s \frac{\partial T_s(x,\tau)}{\partial x} - \rho L \frac{dX(\tau)}{d\tau}, \quad x = X(\tau) \tag{3.10}$$

$$-k_l \frac{\partial T_l(x,\tau)}{\partial x} = AI, \qquad x = 0 \tag{3.11}$$

$$T_s(x,\tau) = T_{amb}, \qquad x \to \infty \tag{3.12}$$

$$X(\tau) = 0, \quad \tau = 0 \tag{3.13}$$

3.1.3 Phase 2 approximate solution

Although this work is only concerned with periods after the onset of melting, periods before melting are considered for the sake of finding the solid region temperature profile. At the initial time $\tau = 0, X(\tau) = 0$ and $T_s = T_{amb}$ therefore, it is only the solid region that exists, and the problem can be treated as a transient process in a semi-infinite solid. The solution thereof has been solved by Gabhart [92].

In his solution, the temperature is initially $T_i(x,0)$ throughout the target (i.e. surface and target interior), and the surface temperature is changed to $T_{i+1}(0,\tau)$ at the onset of heat application. The temperature in the solid increases from $T_i(x,0)$ to $T_{i+1}(x,\tau)$ with time. The following conditions describe the statement in terms of temperature excess,

$$\frac{\partial^2\theta}{\partial x^2} = \frac{1}{\alpha}\frac{\partial\theta}{\partial\tau} \tag{3.14}$$

$$\theta = 0, \quad x \to \infty \tag{3.15}$$

<u>At $\tau = 0$:</u>

$$\theta_1 = T_{i+1}(0,\tau) - T_i(x,0), \quad x \geq 0 \tag{3.16}$$

<u>For $\tau > 0$:</u>

$$\theta = 0, \quad x = 0 \tag{3.17}$$

The solution to Equations (3.14) – (3.17) is given by

$$\frac{\theta}{\theta_1} = erfc\left(\frac{x}{\sqrt{4\alpha\tau}}\right) \tag{3.18}$$

Gebhart's [92] solution is modified and used to approximate the temperature profile in the solid region of Figure 3.1.

$$\frac{T_s(x,\tau) - T_{amb}}{T_m - T_{amb}} = erfc\left(\frac{x}{\sqrt{4\alpha_s\tau}}\right) \tag{3.19}$$

Or

$$T_s(x,\tau) = T_{amb} + (T_m - T_{amb})erfc\left(\frac{x}{\sqrt{4\alpha_s\tau}}\right) \tag{3.20}$$

The temperature delta ($T_m - T_{amb}$) represents the maximum temperature-increase possible in the solid phase. According to Xie and Kar [10], the time for the surface to reach melting temperature is obtained by

$$\tau_m = \frac{\pi k_s{}^2 (T_m - T_{amb})^2}{4\alpha_s (AI)^2} \tag{3.21}$$

Therefore

$$T_m - T_{amb} = \frac{\sqrt{4\alpha_s \tau_m} AI}{\sqrt{\pi} k_s} \tag{3.22}$$

Equation (3.22) states that for the target surface to undergo the given temperature change, the absorbed laser intensity $I\left(\frac{W}{m^2}\right)$ has to be stored for τ_m seconds. Laser intensity is the amount of laser power delivered per m^2 area of the target surface.

Considering that the onset of melting is at τ_m, it follows that with an increase in time ($\tau > \tau_m$) Equation (3.22) needs to be modified for $x \geq X(\tau)$. Figure 3.2 demonstrates the latter.

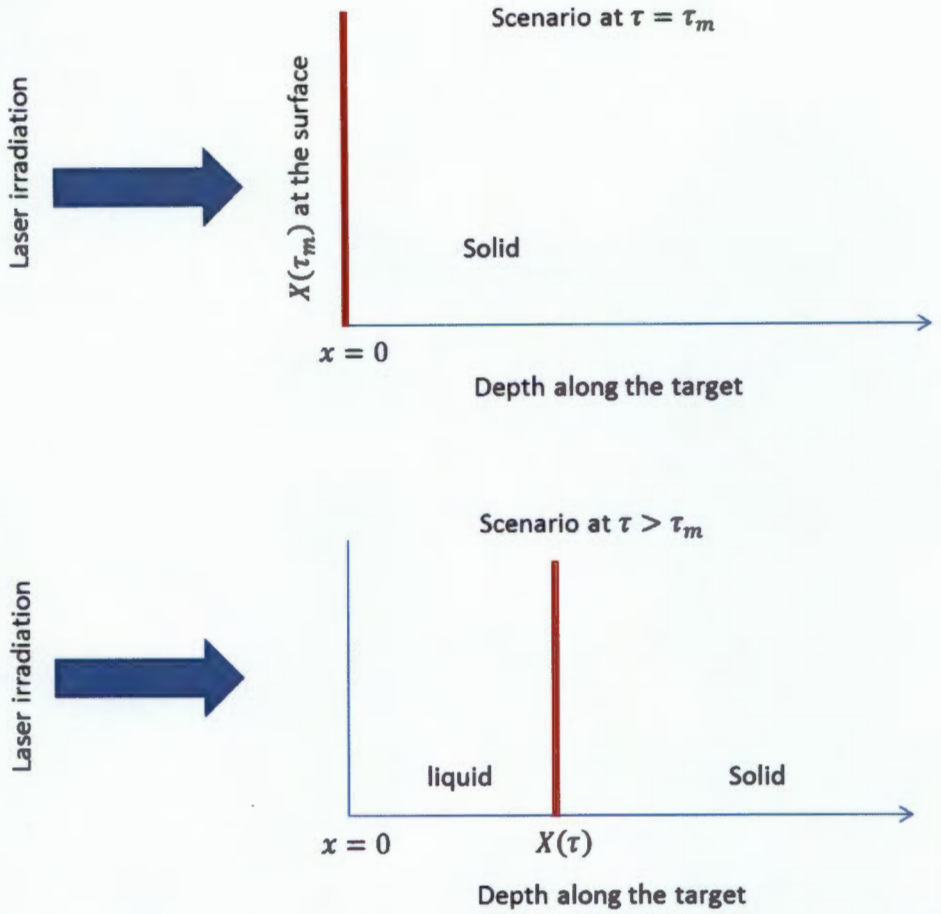

Figure 3.2: Demonstration of solid regions ($x \geq X(\tau)$) reaching a ΔT of $T_m - T_{amb}$ at $\tau > \tau_m$.

From Figure 3.2 it is clear that it is only at $x = 0 = X(\tau_m)$ that $\Delta T = T_m - T_{amb}$. However, when the phase boundary $X(\tau)$ has started moving into the target, the remaining solid regions can only reach $\Delta T = T_m - T_{amb}$ at $\tau > \tau_m$. Therefore Equation (3.22) can be generalized as

$$T_m - T_{amb} = \frac{\sqrt{4\alpha_s \tau} AI}{\sqrt{\pi} k_s} \qquad x > X(\tau), \tau > \tau_m \tag{3.23}$$

Therefore, Equation (3.20) can be rewritten as

$$T_s(x,\tau) = T_{amb} + \frac{\sqrt{4\alpha_s \tau} AI}{\sqrt{\pi} k_s} erfc\left(\frac{x}{\sqrt{4\alpha_s \tau}}\right) \tag{3.24}$$

3.1.4 *Phase 1 approximate solution*

The aim here is to approximate the temperature profile in the molten region. The temperature profile is assumed to be

$$T_l(x,\tau) = Dx^2 + Bx + C \tag{3.25}$$

The variable B is determined by satisfying the condition in Equation (3.11)

$$\frac{-AI}{k_l} = 2D(0) + B \tag{3.26}$$

$$B = \frac{-AI}{k_l} \tag{3.27}$$

To solve for the variable C, Equation (3.9) is satisfied. Therefore,

$$T_m = DX(\tau)^2 + \frac{-AI}{k_l}X(\tau) + C \tag{3.28}$$

and

$$C = T_m - DX(\tau)^2 + \frac{AI}{k_l}X(\tau) \tag{3.29}$$

Therefore the liquid phase temperature profile is

$$T_l(x,\tau) = Dx^2 - \frac{AI}{k_l}x + (T_m - DX(\tau)^2 + \frac{AI}{k_l}X(\tau)) \tag{3.30}$$

When rearranged, Equation (3.30) is

$$T_l(x,\tau) = -\frac{AI}{k_l}\big(x - X(\tau)\big) + D\big(x^2 - X(\tau)^2\big) + T_m \tag{3.31}$$

To solve for D the condition in Equation (3.10) is satisfied.

$$k_l\left(-\frac{AI}{k_l} + 2DX(\tau)\right) = k_s\left(\frac{\sqrt{4\alpha_s\tau}AI}{\sqrt{\pi}k_s}\right)\left(\frac{2}{\pi}\right)e^{-\left(\frac{X(\tau)^2}{4\alpha_s\tau}\right)}\left(\frac{1}{\sqrt{4\alpha_s\tau}}\right) - \rho L\frac{dX(\tau)}{d\tau} \tag{3.32}$$

Therefore,

$$D = \frac{\frac{1}{k_l}\left(k_s\left(\frac{\sqrt{4\alpha_s\tau}AI}{\sqrt{\pi}k_s}\right)e^{-\left(\frac{X(\tau)^2}{4\alpha_s\tau}\right)} - \rho L\frac{dX(\tau)}{d\tau}\right) + \frac{AI}{k_l}}{2X(\tau)} \quad (3.33)$$

3.1.5 Phase boundary approximate solution

In order to derive an approximate solution for the moving phase boundary, the condition in Equation (3.9) is satisfied using the solid phase temperature profile in Equation (3.24).

$$T_m = T_{amb} + \frac{\sqrt{4\alpha_s\tau}AI}{\sqrt{\pi}k_s} erfc\left(\frac{X(\tau)}{\sqrt{4\alpha_s\tau}}\right) \quad (3.34)$$

Rearranging Equation (3.34) yields an equation for $X(\tau)$

$$X(\tau) = \sqrt{4\alpha_s\tau} \times erfc^{-1}\left(\frac{\sqrt{\pi}k_s(T_m - T_{amb})}{\sqrt{4\alpha_s\tau}AI}\right) \quad (3.35)$$

3.2 Laser parametric study

To understand the effect of laser parameters on heat transfer, a parametrical study is done for different laser parameters. Other literature [50, 71, 84] have investigated the influence of laser parameters: scanning speed and beam diameter on the heat transfer. However, these parameters are not investigated in this laser parametric study. The reason for their omission is that the model in this study is based on a stationary laser beam and workpiece. Therefore, the effects of scanning speed on the heat transfer are not covered. The beam diameter is not given its own treatment because laser intensity is a function of the beam diameter.

3.2.1 Laser power

Laser power and laser intensity are related through the following expression

$$I = \frac{P}{\pi\frac{b^2}{4}} \quad (3.36)$$

where P and b are laser power and laser beam spot size respectively. With b kept constant (as is done in this work), laser intensity increases with increasing laser power. Even though the melt depth in Equation (3.35) is a function of laser intensity I, this work will evaluate the

effects of laser power. This is because with the experimental work, it is the laser power that is varied in order to vary the laser intensity.

An increase in laser power has been reported to increase temperature profiles inside a heated target [9, 10, 15, 83]. When laser power is increased whilst pulse duration is kept constant, the amount of thermal energy carried in a pulse increases. Therefore, there is an increase in the amount of energy available for absorption by the heated target. An increase in the total energy absorbed by the heated target, results in an increase in the amount of energy available to raise temperatures.

With increasing temperatures, melting is probable. The melt depth is the depth to which the melt-front propagates into the workpiece, which is always at $T = T_m$. As shown in Figure 3.3, the melt depth increases with an increase in laser power. Another way of explaining the trend shown in Figure 3.3 is by making reference to two points on the curve, $300\ W$ and $1200\ W$. The two conditions have equal thermal diffusivities but different amounts of absorbed energy. Therefore, the condition with a higher amount of absorbed energy will have increased temperatures comparatively. Therefore, the excess energy in the $1200\ W$ condition is responsible for increasing temperatures to beyond the melting point, of areas that still remain solid in the $300\ W$ condition. Consequently, the melt depth increases with increasing laser power. This relationship between the melt depth and laser power was also observed by Xie and Kar [10].

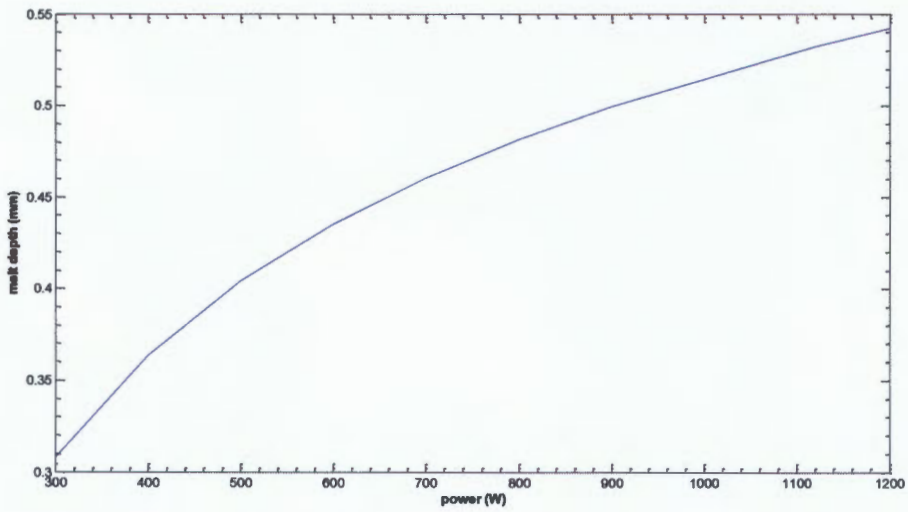

Figure 3.3: Influence of laser power on melt depth with pulse duration kept constant at $5ms$ and laser beam spot size of $600\mu m$. Melt depth modelled for Ti.

3.2.2 Pulse duration

Experimental studies for laser drilling of fused quartz and sapphire, and spot welding of stainless steel showed that the melt depth increased rapidly at the beginning of laser

heating and then slowly after a certain time [10]. A similar trend is shown in Figure 3.4. The melt depth is shown to increase rapidly at smaller exposure times, and slower as it approaches its maximum. This trend is also observed in other literature [10, 15, 72].

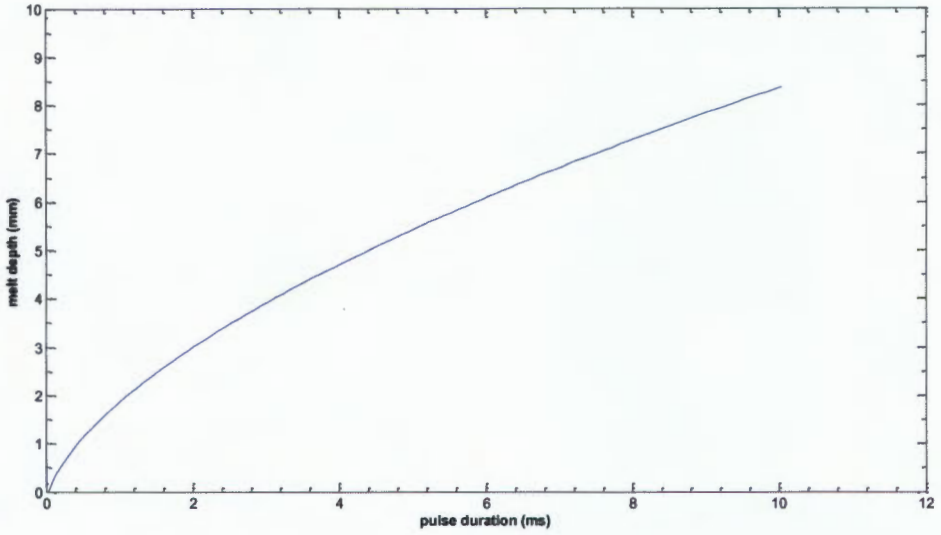

Figure 3.4: Influence of pulse duration on melt depth with laser power of 1200 W and laser beam spot size of 600 μm for Ti.

With increased pulse duration the absorbed energy is given time to be conducted away from the surface to the cooler interior where temperatures are then increased from ambient point. Another way of explaining this is by considering the energy lost to raising temperatures and that lost to conduction being in competition for the total energy's bugdet [11].The laser intensity is assumed to have a constant distribution across the irradiated target. Therefore, it follows that the energy carried in a single pulse increases or decreases with decreasing or increasing pulse duration respectively.This is shown in Figure 3.5. At short pulse durations, the conduction losses are not enough to support the increased incoming flux of energy carried in the short pulse. Therefore, the majority of the absorbed energy is used up in raising near-surface temperatures and less lost to conduction. This explains the rapid increase in the melt depth at shorter pulse durations.

However, at longer pulse durations there is a greater energy transfer rate than there is of energy used to raise temperatures. However, with time there is less and less energy left for a transfer after a portion is used every time in raising temperatures [83]. This is when the melt depth starts increasing slowly. It continues to increase slower until it reaches a maximum, which is where there is no more energy left to either increase temperatures beyond or maintain them at the melting point

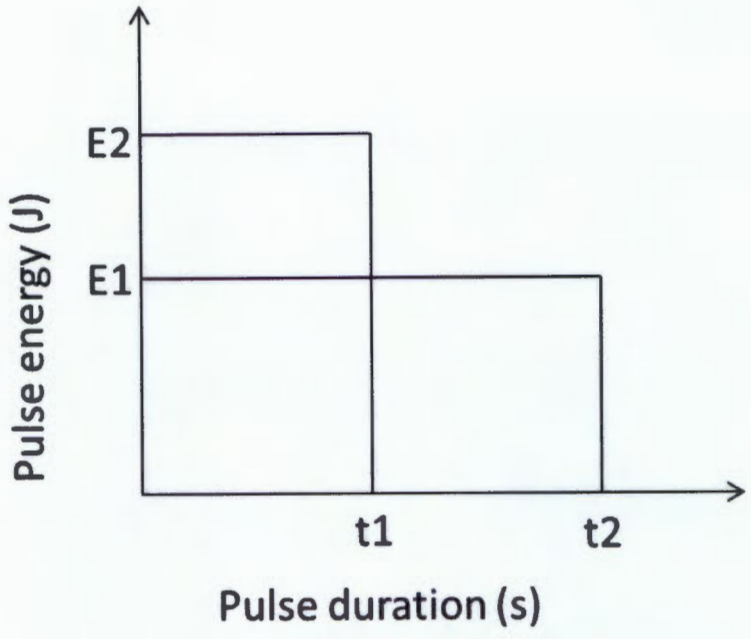

Figure 3.5: Illustration of the effect of pulse duration on laser pulse energy with laser beam intensity assumed to have a constant distribution across the irradiated surface area.

3.3 Thermophysical parametric study

In addition to laser parameters, the thermophysical properties of a material influence the thermal energy transfer. It has been established in the previous parametric study, that the amount of energy and the rate at which that energy is transferred to the interior of the workpiece, influence the temperature profiles. The absorption coefficient (A) and thermal diffusivity (α), affect the amount of absorbed energy and the rate at which that energy is transferred, respectively. There are two possible ways in which this study can be conducted. First, the particular parameters can be varied whilst keeping all other parameters constant. The only problem with this way is that there will be combinations of thermophysical properties that will represent unreal materials. Investigating unreal materials will only make the investigation irrelevant. The second method is to keep this study relevant by using real materials. However, because of the uniqueness of each material, it will be difficult to single out the influence of one thermophysical parameter on the melt depth.

In all cases where the second method is employed, the materials used for comparison purposes are titanium alloy (Ti6Al4V) and gold (Au). The choice of these materials is motivated by their extremely differing absorption coefficients and thermal diffusivities. The different absorption coefficients and thermal diffusivities allow for the investigation of the effects of varying these thermophysical properties on temperature profiles whilst using real materials. Furthermore, the titanium alloy has a lower thermal diffusivity than gold, but has

the highest absorption coefficient. Therefore, the choice of Ti6Al4V and Au presents the opportunity to investigate the effects of the combinations of low/high absorption coefficient and low/high thermal diffusivity values. Their thermophysical properties used in this parametric study are given in Table 3.1.

Table 3.1 Thermo-physical properties of Au and Ti6Al4V for [a]solid phase and [b]liquid phase [83].

	Au	Ti6Al4V
Density (kg/m^3)	19320	4110
Melting temperature (K)	1336	1928
Latent heat of fusion (J/kg)	66200	290000
Specific heat capacity (J/kgK)	128.8^a 148.6^b	764.58^a 1126^b
Thermal conductivity (W/mK)	314.4^a 99^b	20^a 29^b
Thermal diffusivity (x 10^{-6} m^2/s)	126^a 34.46^b	5.8^a 5.95^b
Absorption coefficient	0.018^a 0.16^b	0.23^a 0.433^b

3.3.1 Absorption coefficient

The absorption coefficient is the first thermophysical property to contribute to thermal transfer at the start of laser irradiation since energy must first be absorbed into the heated target, before heat conduction can occur. From the knowledge that a material with a high absorption coefficient absorbs larger amounts of energy, it is expected that that material will exhibit higher temperatures relatively. Consequently, melting occurs at relatively smaller times for a material with superior absorption coefficient. Figure 3.6 is a comparison of the melting time of Ti6Al4V and Au with increasing laser power. According to Figure 3.6, the melting time decreases with increasing laser power. As already mentioned earlier, increasing laser power effectively increases the total internal thermal energy. Even though the internal energy increases, the thermal conductivity remains constant therefore conduction losses are not substantial enough to slow down the temperature rise [11].Therefore, with an increase in the influx of thermal energy , the times at which melting occurs decrease. Given that the absorption coefficient of Ti6Al4V is almost three times that of Au, it follows that it should absorb more of the beams energy that Au does. Therefore, it is expected that Ti6Al4V reaches its melting temperature before Au does due to increased amounts of internal thermal energy. The expectation is proven true as shown in Figure 3.6. Despite its higher melting temperature, the melting time for Ti6Al4V is smaller than that for Au (with the lower melting temperature).

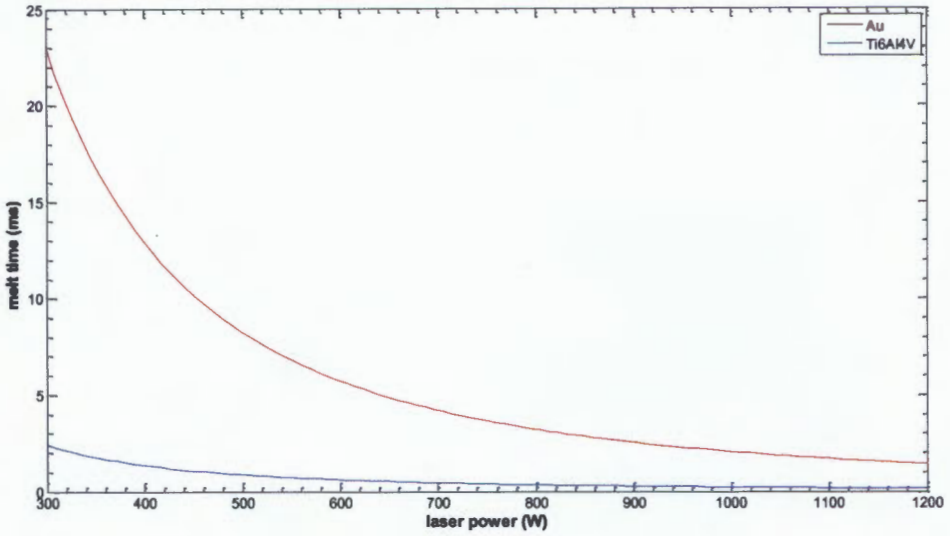

Figure 3.6: Melting times for Au and Ti6Al4V with increasing laser power.

3.3.2 Thermal diffusivity

The term α_s $(m.s^{-1})$ is understood to be the diffusivity of a material's solid phase. It is a measure of a material's ability to conduct thermal energy relative to its ability to store thermal energy [87]. Therefore, the internal energy (responsible for raising temperatures) and the energy lost to conduction are always in competition for the budget of the total absorbed energy [11]. Diffusivity is generally expressed as shown in Equation (3.37), where k is conductivity and ρc_p is the volumetric thermal capacity.

$$\alpha = \frac{k}{\rho c_p} \tag{3.37}$$

Wang and Chang [83] simulated laser welding of Ti and Au, and they found that the superior k value of Au was responsible for a thermal penetration depth much larger than that of Ti. Figure 3.7 is a comparison of the melt depths of Ti6Al4V and Au. With increased pulse duration, the melt depth for both materials increases. This is expected since it has been shown that melt depths increase with increasing pulse duration. Also, Ti6Al4V melts first at 0.6 ms and Au melts later at 5.7 ms. The earlier melting of the Ti6Al4V surface has already been attributed to its superior absorption coefficient.

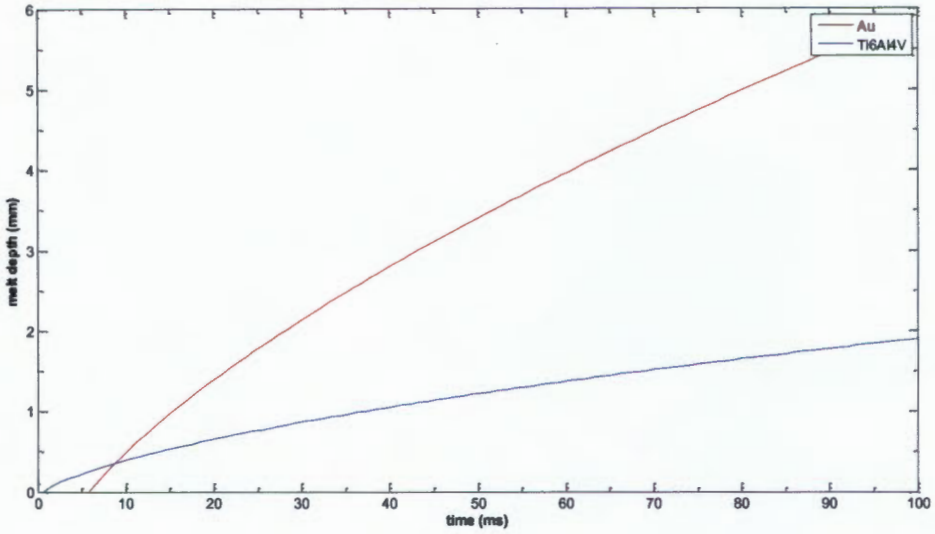

Figure 3.7: Comparison of the melt depths of Ti6Al4V and Au with increasing pulse duration for laser power of $600\,W$.

However, the melt depth of Au is seen to increase beyond that of Ti6Al4V with increasing pulse duration. To explain this observation, the energy-storage capacities ρc_p will not be considered since they are similar thus cannot be regarded for comparison purposes. In order to initiate melting, energy is required to raise temperatures to the melting point. In order for the melt depth to grow, energy needs to be conducted to the cooler interior of the heated target where that energy can be used to raise temperatures to the melting point. Both materials are absorbing enough of the $600\,W$ of laser power to be able to initiate melting. However, unlike Au, Ti6Al4V is not able to conduct the thermal energy to the cooler regions rapidly enough for its melt depth to increase rapidly. Although Ti6Al4V absorbs almost three times more laser power than Au, it has a higher melting temperature. Therefore it requires more energy to raise its temperatures to the melting point. On the other hand, Au absorbs less of the laser power but, it has a lower melting temperature. Therefore, it requires less energy to raise temperatures to its melting point.

3.4 Comparative study

To complete the feasibility study, the current analytical model must be compared to experimental data obtained by other researchers. The aim is to obtain an idea of the accuracy with which this analytical model approximates thermal transfer during laser irradiation.

Figure 3.8 is a comparison of the laser spot welding results obtained by He et al. [76] in their study of heat transfer and fluid flow during laser spot welding of 304 stainless steel with the calculated results thereof. The thermo-physical properties used for 304 stainless steel are obtainable from the work of He et al. [76] and Xie and Kar [10]. It must be noted that the laser beam diameter and the pulse duration are assumed values. He et al. [76] did not specify the specific values used for laser beam diameter and pulse duration in generating the results shown in Figure 3.8. However, the values for laser beam diameter and pulse duration are both from the laser parameter range (of both laser beam diameter and pulse duration) specified in their report.

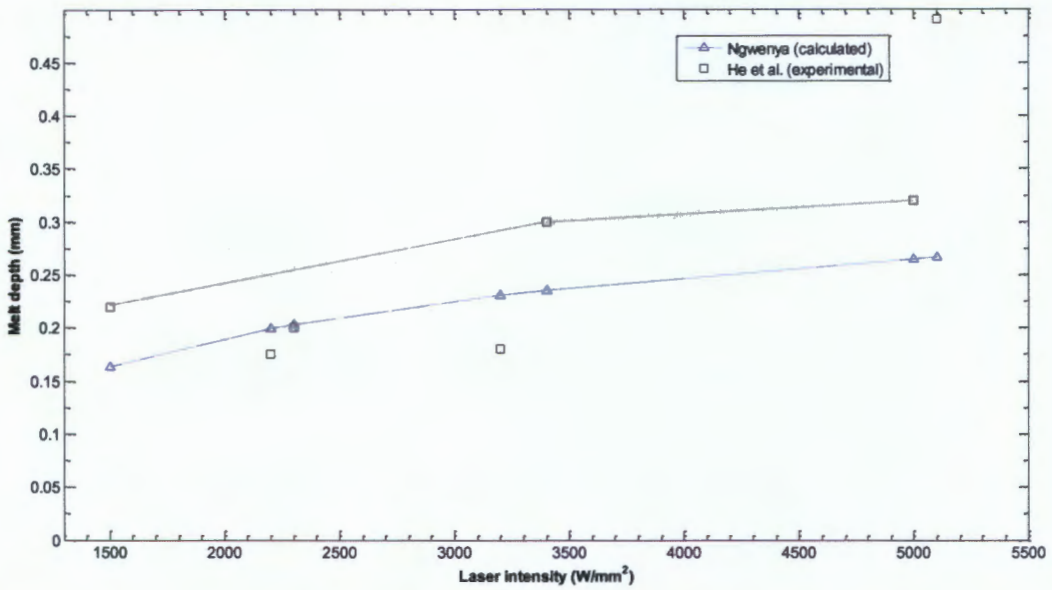

Figure 3.8: A comparison of the calculated and experimental results of the effects of laser intensity on the melt depth. A beam diameter and pulse duration of 428μm and 3ms are assumed [76].

The calculated results for 304 stainless steel are generally not in agreement with the experimental results. It is only at laser intensity of $2300W/mm^2$ that the calculated melt depth is equal to the experimental value. However, the results by He et al. [76] seem to trend in a similar manner to that of the calculated melt depth. The reason for the disagreement is unclear. He et al. [76] reported to have varied laser intensity as a result of varying the beam diameter. Assumptions made on beam diameter and pulse duration could have an effect on the outcome of the results in Figure 3.8. Firstly, in generating Figure 3.8 the beam diameter was assumed to be constant when in fact it was varied by He et al. [76] to get the same laser intensity, but only a range of the beam diameter was given and the specific pairing of parameters was not given. Suder and Williams [71] found that having the same laser intensity does not translate into having the same specific point energy during the

interaction time (pulse duration). This could explain the differences between the calculations by Ngwenya and the experimental results by He et al. [76]. The reason for the decrease in the measured melt depth at laser intensity values $2200W/mm^2$ and $3200W/mm^2$ was not mentioned in the work of He et al. [76].

Without the knowledge of specific laser parameter combinations used in experiments, comparisons are made difficult. Despite the lack of specification of the combination of laser parameters used in the experimental results of He et al. [76], the calculated melt depths by Ngwenya show an agreement with the experimental results within a 45% error.

Chang and Na [63] conducted single-pulsed spot welding experiments to validate their predictions. Figure 3.9 is a comparison of the approximations calculated by Ngwenya with the experimental results of Chang and Na [63].

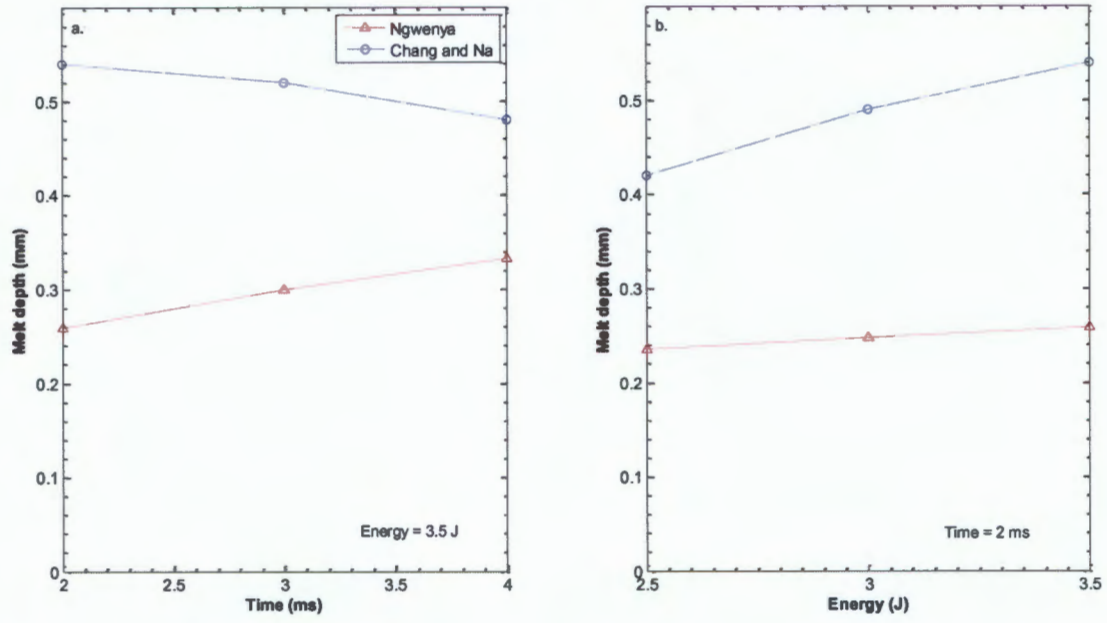

Figure 3.9: Comparison of the calculated melt depths by Ngwenya with the experimental results obtained by Chang and Na [63]. Beam diameter of $428\mu m$ is assumed.

The limitations presented by the experimental results do not allow for a more detailed comparison of the two data sets. The first limitation is the same problem encountered with the previous comparison, due to the non-specification of the beam diameter an assumption had to be made. The beam diameter used in the calculations for Figure 3.9 is $328\ \mu m$. Laser intensity values were not given either therefore the calculation of a beam diameter used in the experiments was not possible. The second limitation is the number of data points given. For their study, three data points were sufficient to show a correlation with their predictions. For the three data points, their predictions showed excellent agreement with their experimental results. However, the calculated melt depths by Ngwenya are under-

approximating the experimental results. Therefore, it is suspected that more data points would allow for a more conclusive comparison over a wider range of time and energy. The third limitation falls out of the scope of this research but is nonetheless worth being mentioned. These particular experimental results were obtained under the 'no gap' condition. Chang an Na [63] varied the gap size between the two specimens to be laser spot welded from $0 - 0.12\ mm$. The closest condition to the current work is that which has no gap between the two laser spot welded specimens. This 'no gap' condition was picked for comparison purposes over the others because the model developed in this work does not take into account the convection losses in the gap. With that said, there is no guarantee as to how tightly closed the gap between the two specimens was in order to deem the two specimens as one. The fourth limitation is the small specimen thickness used in the experiments. For instance, the thicknesses of the specimens used in the experiments whose results are shown in Figure 3.9 are $0.3\ and\ 0.33\ mm$. The model developed in this work assumes that the irradiated specimen is semi-infinite. That is, the specimen is infinite in the z direction thus producing a heat sink effect. The effects of having a specimen infinite in the z direction and having another with finite depth on the transfer of heat may result in differing melt depths in each specimen.

Despite the limitations of the comparison between the two data sets in Figure 3.9, the calculations under-approximate the experimental results by a maximum of 52% in both Figures 3.9 (a) and (b).

With the limitations associated with the above assessment, conclusions on the success of the adapted model cannot be drawn and be considered conclusive yet. Even more so, a comparison with only two sets of work by other researchers is not considered to be enough to draw concrete conclusions. However, the assessment does reveal that the adapted model's approximations are at least following a trend that is similar to what other researchers have reported.

3.5 Experimental approach

3.5.1 Sample preparation

The CP titanium sheet of dimension $150mm \times 150mm \times 5mm$ was cut into 39 samples of dimension $15mm \times 15mm \times 5mm$. The samples were cleaned in acetone to remove any grease or lubrication from the cutting process.

3.5.2 *Single pulse laser irradiation*

The 39 CP titanium samples were laser irradiated. Each sample was irradiated with a single pulse. The focal spot on the sample surface was 600 μm. The shielding gas used was nitrogen at a flow rate of 5 l/min to prevent oxidation. The angle of the incident laser beam axis with respect to the normal axis (perpendicular to the sample surface) was 10°. Table 3.2 describes the laser irradiation conditions that each sample was subjected to. Each experimental condition was used three times for reproducibility of results.

Table 3.2: Description of the experimental conditions used for each set of laser-processed samples

Sample	Laser power (W)	Pulse duration (s)	Pulse energy (J)
1 – 3	1200	0.1	120
4 - 6	1200	1	1200
7 – 9	300	1	300
10 – 12	600	0.1	60
13 – 15	600	1	600
16 – 18	600	5	3000
19 – 21	300	10	3000
22 – 24	900	0.1	90
25 – 27	900	1	900

3.6 Post experiment analysis

Before processing, the sample surfaces were examined using a Nikon Shuttle Pix P.MFSC optical microscope. Each laser irradiated sample was then cut perpendicular to its surface with a diamond blade cutter at a speed of $5\ rpm$. The cross-sections were prepared for microstructrural analysis. The cross-sectioned samples were hot-compression mounted with MultiFast resin. The grinding process was carried out with 800 SiC paper for $25s$ and with 1200 SiC paper for $60s$ or long enough to achieve a flat surface for polishing. The grinding speed was $300\ rpm$. Its ductility makes titanium prone to mechanical deformation during grinding or/and polishing. These grinding times were kept as short as possible to avoid losing significant amount of the laser-affected regions. After grinding, the samples were rinsed with distilled water then placed in a solution of ethanol and put inside the ultrasonic bath for $10\ min$. Micrographs of the as-ground surfaces were captured with an optical microscope. The polishing was done with the following procedure:

1. $9\mu m$ diamond polishing for $10\ min$
2. Chemical-mechanical polishing with a mixture of $50\ ml$ colloidal silica (OP-S) and $10\ ml$ hydrogen peroxide (40%) for $10\ min$
3. Water flushing for $5\ min$

This entire polishing procedure was automatic with a polishing speed of $150\ rpm$. Both grinding and polishing processes used a force of $30\ N$. The polished surfaces were etched with a mixture of Keller's reagent. The solution included:

$190\ ml$ Distilled water

$5\ ml$ HNO_3

$3\ ml$ HCl

$2\ ml$ HF

Due to unsuccessful etching results, the first polishing step was omitted as it was suspected that the mechanical deformation seen on the polished surfaces was from the diamond suspension used in the $9\ \mu m$. Consequently the second step 'attack polishing' was carried out for $20\ min$. The etched surfaces were examined under an optical microscope.

3.7 Experimental Limitations

It is difficult to measure the spatial temperature profile inside a sample of $5mm$ depth during laser irradiation. The inability to drill holes small enough to mount thermocouples into the samples prevented the spatial temperature profiles from being measured. Consequently the spatial temperature profiles (measured and calculated) could not be compared. However, the isotherm depth which is the by-product of the adapted model was measurable. Therefore, it is important to note that only the melt depth and beta phase transformation depths were measured and compared with the calculated depths.

The metallurgy of titanium also posed limitations during the post-experiment analysis. As part of evaluating the effects of laser parameters on the resulting melt zone, phase differentiation was planned to be done. Phase differentiation involves identify phases present in the melt zone in order to identify 'phase freezing' as a result of extreme laser parameters (high laser power vs low laser power). This could not be achieved with the available Scanning Electron Microscope (SEM). What was possible with SEM was the identification of elements. Given that titanium is a pure metal, phases present in the melt zone would merely comprise titanium and no other element. Therefore, only titanium would be picked up by SEM. A possible method of phase differentiation would be using the fact that the lattice parameters for titanium phases are all different. However, this would require a different type of microscope. A likely option would be the Transmission Electron Microscope (TEM). Due to time constraints, this option was not explored.

4 RESULTS AND DISCUSSIONS

Mathematical expressions are better utilized when their physical interpretation is understood. In addition to presenting the results and discussion, this chapter reviews the terms of the solution with the aim to observe their physical meaning.

4.1 Effects of laser pulse

At t_m the surface of the laser heated target is expected to melt. Therefore, the melt depth is expected to be zero at the onset of melting. The expressions for τ_m and $X(\tau)$ are given again below for the convenience of the reader.

$$\tau_m = \frac{\pi k_s{}^2 (T_m - T_{amb})^2}{4\alpha_s (AI)^2} \tag{4.1}$$

$$X(\tau) = \sqrt{4\alpha_s \tau} \times erfc^{-1}\left(\frac{\sqrt{\pi} k_s (T_m - T_{amb})}{\sqrt{4\alpha_s \tau} AI}\right) \tag{4.2}$$

The substitution of Equation (4.1) into Equation (4.2) should result in $X(\tau_m) = 0$. This is demonstrated below.

$$X(\tau_m) = \sqrt{4\alpha_s \frac{\pi k_s{}^2 (T_m - T_{amb})^2}{4\alpha_s (AI)^2}} \times erfc^{-1}\left(\frac{\sqrt{\pi} k_s (T_m - T_{amb})}{\sqrt{4\alpha_s \frac{\pi k_s{}^2 (T_m - T_{amb})^2}{4\alpha_s (AI)^2}} AI}\right) \tag{4.3}$$

Equation (4.3) becomes

$$X(\tau_m) = \frac{\sqrt{\pi} k_s (T_m - T_{amb})}{AI} \times erfc^{-1}(1) \tag{4.4}$$

which finally results in

$$X(\tau_m) = 0 \tag{4.5}$$

The physical meaning of Equation (4.5) is that at the onset of melting ($\tau = \tau_m$) the moving phase boundary should still be at the target's surface. So far from the demonstration given by Equations (4.3) to (4.5), the approximated solution of the melt depth yields expected results at the onset of melting. The physical interpretation of the approximated solution for times greater than the melting time is also required.

From the explanation of diffusivity given in the previous chapter, it follows that the term $\sqrt{4\alpha_s\tau}$ from Equation (4.2) describes the depth to which thermal energy penetrates a material in a certain amount of time. Figure (4.1) is an illustration of how the term $\sqrt{4\alpha_s\tau}$ evolves with time beyond τ_m. The curve in Figure (4.1) increases rapidly initially and then slowly after a certain time.

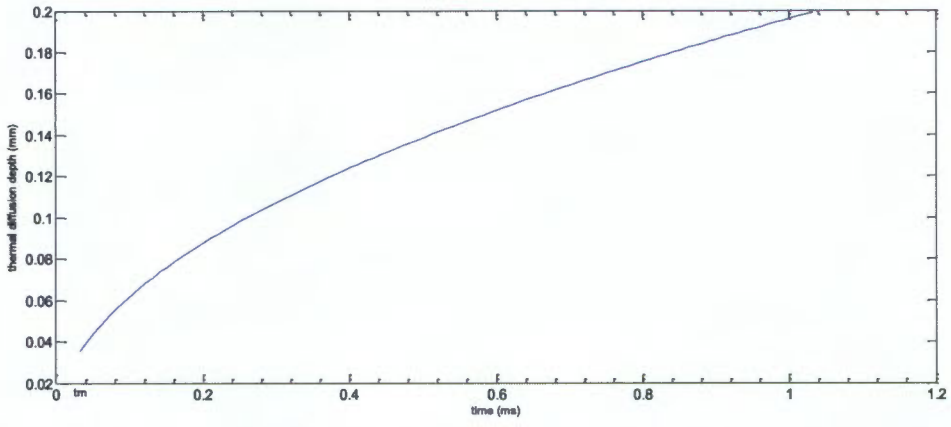

Figure 4.1: Variation of $\sqrt{4\alpha_s\tau}$ with increase in time and laser power of $1200\,W$ for Ti. Properties of Ti are found in Ref. [10].

According to the definition, diffusivity can be thought of as a measure of the competition between how much of the thermal energy is conducted and stored. The portion of the thermal energy that is stored is used to raise temperatures locally. Therefore, at shorter times there is still more thermal energy available for conduction to cooler regions of the material. However, with time there is less and less energy left for further conduction since a portion is used every time in raising temperatures [83]. Consequently the curve increases rapidly in the beginning and begins to increase slowly at longer times. The available thermal energy lessens until there is no more left to be conducted into the material.

From Equation (4.2), the ratio of melt depth to diffusion depth ($\sqrt{4\alpha_s\tau}$) is expressed as

$$\frac{X(\tau)}{\sqrt{4\alpha_s\tau}} = erfc^{-1}\left(\frac{\sqrt{\pi}k_s(T_m - T_{amb})}{\sqrt{4\alpha_s\tau}AI}\right) \tag{4.6}$$

and can be rewritten as

$$\frac{X(\tau)}{\sqrt{4\alpha_s\tau}} = erfc^{-1}\left(\frac{(T_m - T_{amb})}{\frac{\sqrt{4\alpha_s\tau}AI}{\sqrt{\pi}k_s}}\right) \tag{4.7}$$

Equation (4.7) is plotted in Figure 4.2. It can be seen that the ratio of melt depth to the diffusion depth increases with time. It increases rapidly at shorter times, and then continues to increase slowly at longer times. There is however a limitation on up to how far the ratio in Figure 4.2 can increase. Realistically, the melt depth should be less than or equal to the diffusion depth ($X(\tau) \leq \sqrt{4\alpha_s\tau}$). Before melting can occur within the solid region, local temperatures must have been increased gradually. Therefore, there must first be thermal energy transferred to those cooler regions in order to raise temperatures to T_m. It is for this reason that the melt depth cannot be greater than the diffusion depth. Therefore, the limit to which the ratio in Figure 4.2 can increase is 1. The reader is reminded that with time, the melt depth penetrates deeper into the material. Therefore, the liquid region increases at the expense of the solid region. Consequently, the expectation is that at prolonged times, there will only be a liquid region. In such a case, $X(\tau) = \sqrt{4\alpha_s\tau}$ when the entire material becomes molten. Therefore, the melt depth should seize as there will not be a solid region to penetrate into, hence the limit to which the ratio can increase is unity.

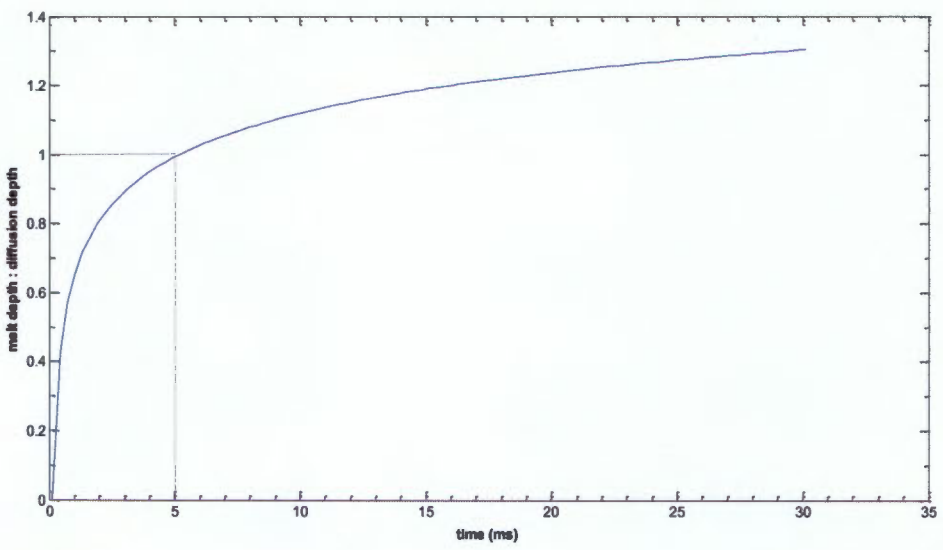

Figure 4.2: Variation of the ratio of melt depth to diffusion depth with time and laser power of 600 W for Ti.

Figure 4.3 shows a plot of $erfc\left(\frac{X(\tau)}{\sqrt{4\alpha_s\tau}}\right)$ (which is an equivalent of the argument of the inverse complimentary error function $\left(\frac{(T_m-T_{amb})}{\frac{\sqrt{4\alpha_s\tau}AI}{\sqrt{\pi}k_s}}\right)$) with time. The argument of the inverse complimentary error function is a ratio of the maximum temperature change in the solid region and the total internal energy. Therefore, it represents a portion of the internal energy that is required to cause a temperature change $T_m - T_{amb}$ at a particular x depth along the path of $X(\tau)$. For an arbitrary point x along the depth of the target, the maximum temperature change occurs with increasing time (i.e $\tau > \tau_m$). For demonstration purposes, let us assume x_1 is an arbitrary point along the depth of the target and that it melts (i.e. experiences$(T_m - T_{amb})$) at τ_1. For $\tau_m \leq \tau < \tau_1$, x_1 is still in solid form therefore as time increases from τ_m to τ_1 the denominator in the above ratio approaches the numerator (which is the maximum allowable temperature difference). So this means that τ may only increase until the denominator equals to the numerator for all points along the depth of the target/path of the melt interface.

From Figure 4.3, it can be seen that this ratio decreases with time. With increasing time, the amount of internal energy increases. However, the temperature change from ambient to melting point remains constant, hence the ratio decreases.

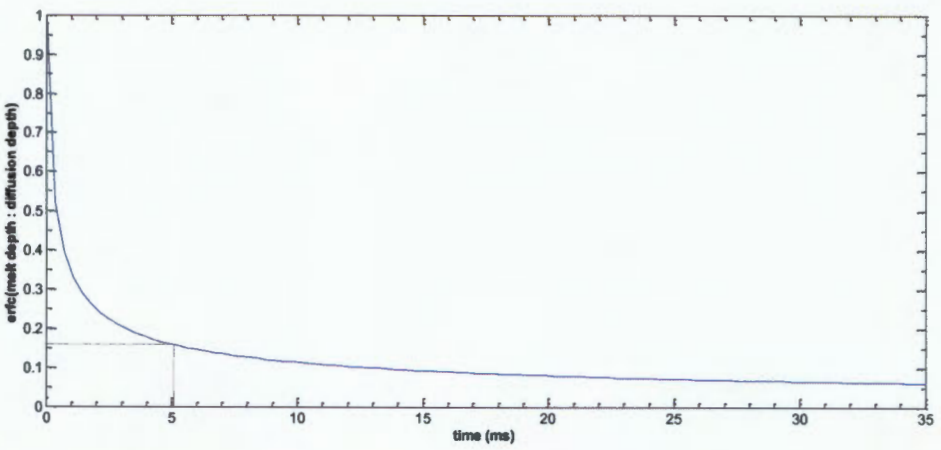

Figure 4.3: Portion of the internal energy within the solid region required for a temperature change $T_m - T_{amb}$ with increasing time for Ti.

4.2 Effects of laser power

The reader is reminded that laser power and laser intensity are related through the following expression

$$I = \frac{P}{\pi \frac{b^2}{4}} \tag{4.8}$$

where P and b are laser power and laser beam spot size (or beam diameter) respectively. With b kept constant (as is done in this work), laser intensity increases with increasing laser power. With reference to Equation (4.7), it is only the argument of the inverse complimentary error function that is influenced by laser power. Figure 4.4 shows that the ratio of melt depth to the diffusion depth increases with increasing laser power. An increase in laser power increases the total internal energy therefore the ratio limit of unity is reached at shorter times. With an increase in internal energy, the melt depth increases more rapidly whilst the diffusion depth remains constant since it is not a function of laser intensity.

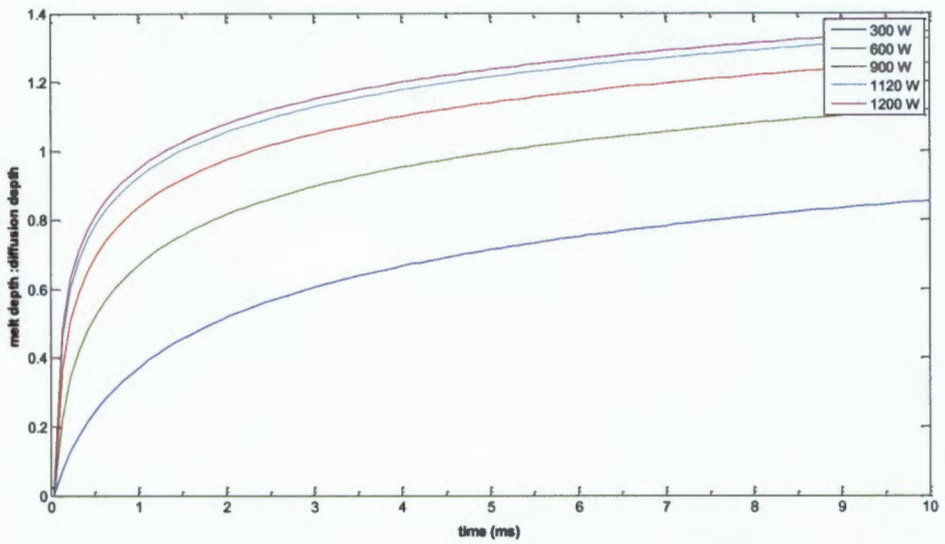

Figure 4.4: Effects of laser power on the ratio of melt depth to diffusion depth with time.

4.3 Macrostructure results and discussion

Laser irradiation processes have to consider the effects of the laser parameters on the desired results. In the case of laser welding, unsuccessful results can be obtained if the melt pool is too large or too small or if significant vaporization occurs during processing [61]. Therefore it is important to know the effects of laser power and pulse duration on the

desired results. This knowledge will assist in the controlling of the process outcome. For the sake of familiarizing the reader with how a laser irradiated CP titanium looks, Figure 4.5 is an annotated cross-section of one of the laser irradiated CP titanium samples.

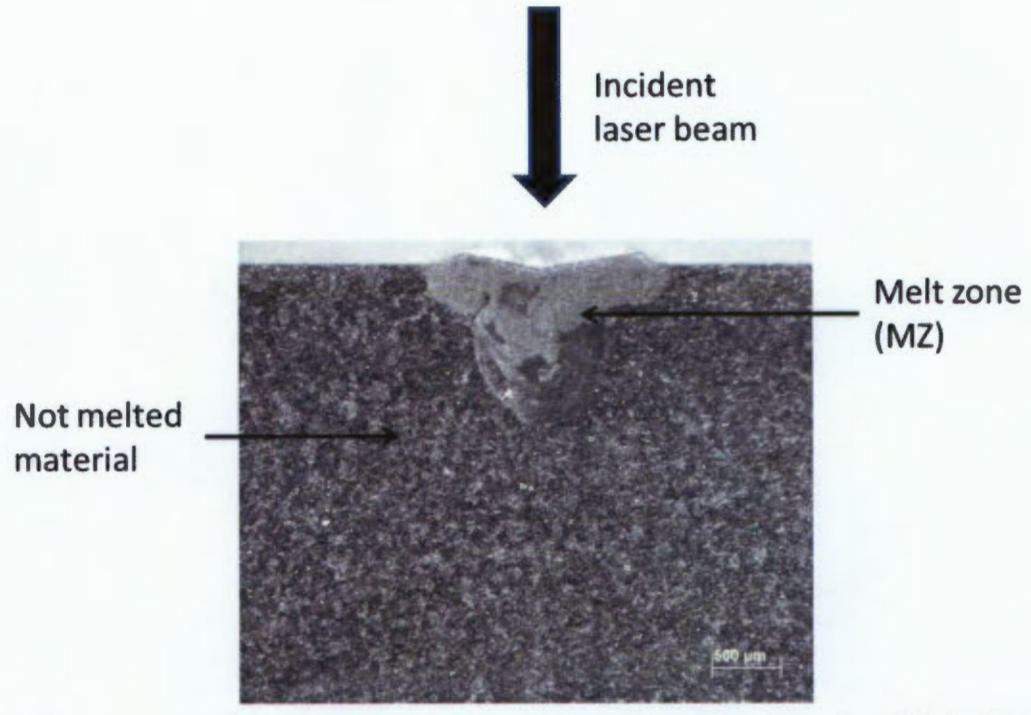

Figure 4.5: Annotated micrograph of a cross-section of a laser irradiated CP titanium sample. Laser parameters used are $1200W$ and $0.1s$.

4.4 Defects associated with laser irradiation

Shown in Figure 4.6 are CP titanium samples with porosity and cracking post laser irradiation. The porosity shown in Figure 4.6 is mainly found in two locations. The porosity shown in Figures 4.6 (a) – (d) is found on the side of the MZ and that in Figures 4.6 (e) and (f) is located at the bottom of the MZ.

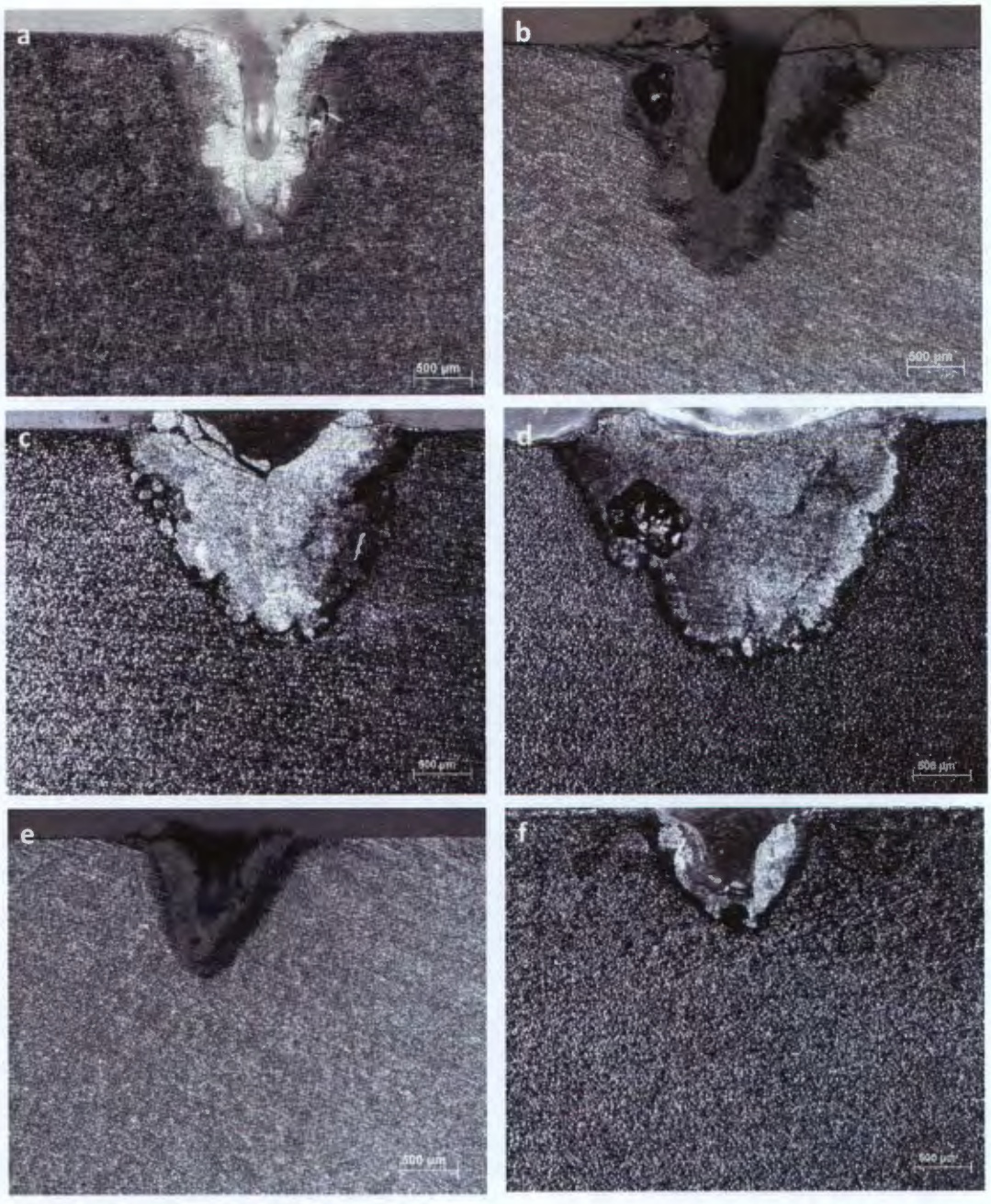

Figure 4.6: Porosity in laser irradiated CP titanium samples (a) $460W$ and $6.5s$, (b) $600W$ and $5s$, (c) $900W$ and $1s$, (d) $1200W$ and $1s$, (e) $300W$ and $10s$ and (f) $600W$ and $1s$.

The reader is reminded that there are two causes of porosity. The one is the entrapment of the shielding gas and/or metal vapour in the molten metal [13, 56]. The other cause of porosity is the rapid enclosure of the keyhole [56]. Due to the instability of the keyhole, the molten metal oscillates upwards and downwards the keyhole wall [73]. The upward motion of the molten metal results in the upper wall of the keyhole being convex. This convex profile of the upper keyhole wall produces pressures that induce a downward flow opposite to the upward flow [73]. These opposing flows collide and form an inward protrusion at the

keyhole entrance. With time, the protrusion grows larger and eventually collapses thus closing the keyhole. Therefore, voids are trapped at the bottom of the keyhole. The porosity shown in Figure 4.6 (e) and (f) is consistent with that caused by the collapsing of the keyhole. The porosity found on the side of the MZ is probably due to the entrapment of either shielding gases or material vapour in the melt pool during laser irradiation.

The cracks observed in the samples shown in Figure 4.6 could be attributed to the high cooling rates associated with laser irradiation. High cooling rates can induce high stress states in the MZ that can often lead to cracking [56].

When the absorbed energy is high enough, surface temperatures can reach evaporation point. With such high temperatures, surface defects such as spattering and cratering are unavoidable. The samples in Figure 4.6 also exhibit craters. The degree of crater formation is different for each sample. However, it must be noted that the sample irradiated at $1200W$ and $1s$ has a shallow crater compared to those of samples irradiated at lower power levels. Since the micrographs in Figure 4.6 are taken at the same magnification, a visual comparison of the size of the craters is possible. Figures 4.6 (c), (d) and (f) show samples irradiated at the same pulse duration but different laser power. It can be seen from these three samples that the depth of a crater decreases with increasing laser power. However, the width of the crater increases with increasing laser power. Also, it should be noticed also that an increase in laser power results in an increase in the size (width and depth) of the MZ. Therefore, the bigger the MZ is, the shallower the crater depth is because of the increased width. Surface craters are caused by mass loss due to evaporation and/or spattering. Spattering is defined as the molten metal droplets that are thrown out of the melt pool [56]. It was suggested by Kawahito et al. [64] that a larger melt pool, as measured by diameter, is required to reduce spattering of the liquid metal. They explained that with a large melt pool, the molten metal droplets that are thrown out of the melt pool fall onto molten region. Therefore, the droplets are returned to the melt pool. The resulting effect is reduced spattering. This could probably explain the trend seen in Figures 4.6 (c), (d) and (f) that the crater depth decreased with increasing laser power whilst the crater width increased with increasing laser power.

4.5 Effects of pulse duration on the melt zone size

Figure 4.7 shows the effects of increasing pulse duration on the size of the MZ. It is clear that an increase in pulse duration results in an increase in the size of the MZ. With the samples shown in Figure 4.7 the laser power and beam diameter were kept constant. Therefore it is expected that the power density should be constant as well.

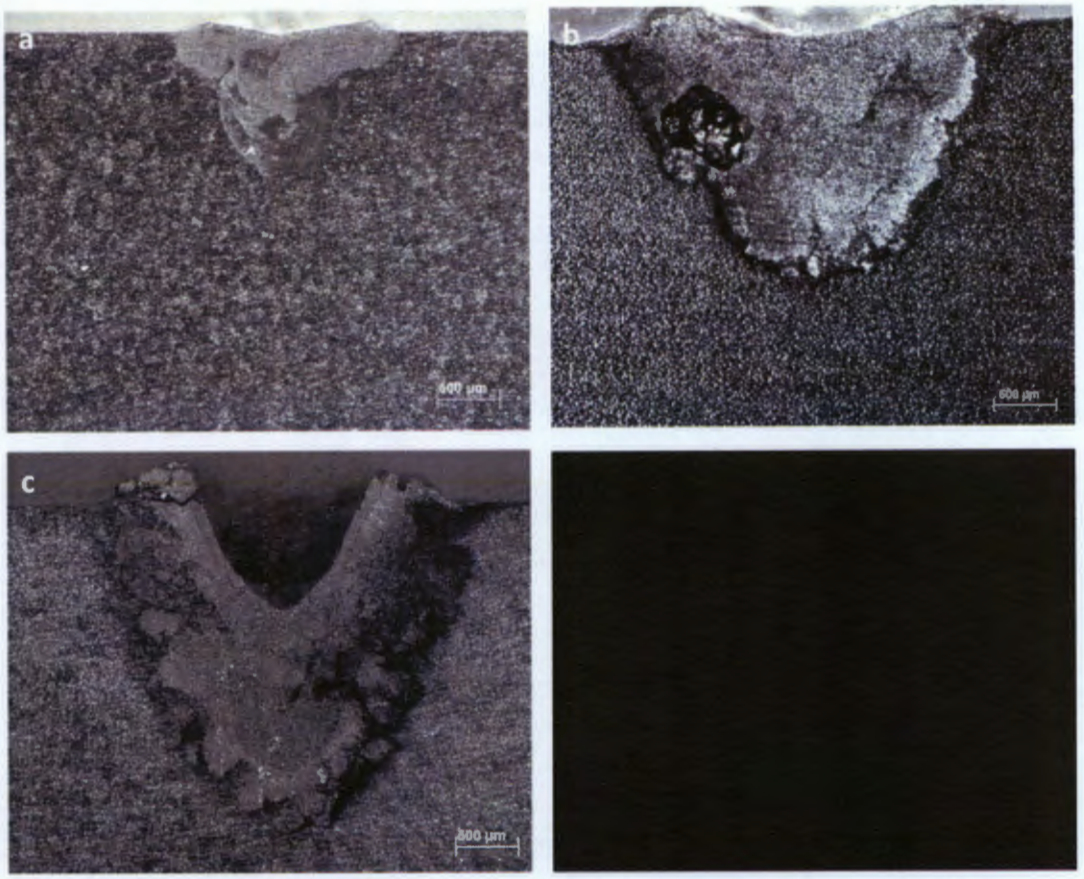

Figure 4.7: Effect of pulse duration (a) $0.1s$, (b) $1s$ and (c) $2.5s$ on melt depth at laser power and beam diameter $1200W$ and $600\mu m$ respectively.

This behaviour can be attributed to the fact that at shorter pulse durations, the absorbed laser energy is greater than the penetrating heat energy [72]. With increasing pulse duration the conduction losses increase and when they equal the amount of absorbed laser energy, the melt depth will reach its maximum. However, the cross-sections shown in Figure 4.7 suggest that the melt depth is still on the increasing side of its trend with increasing pulse duration.

4.6 Effects of laser power on melt zone size

Figure 4.8 shows cross-sections of single-pulse-irradiated titanium samples with a pulse duration of $1s$ and beam diameter $600\mu m$. The melt depth decreases with decreasing laser power. Also, the melt width is observed to increase as well with an increase in laser power. With an increase in laser power the absorbed energy increases thus increasing the melt depth.

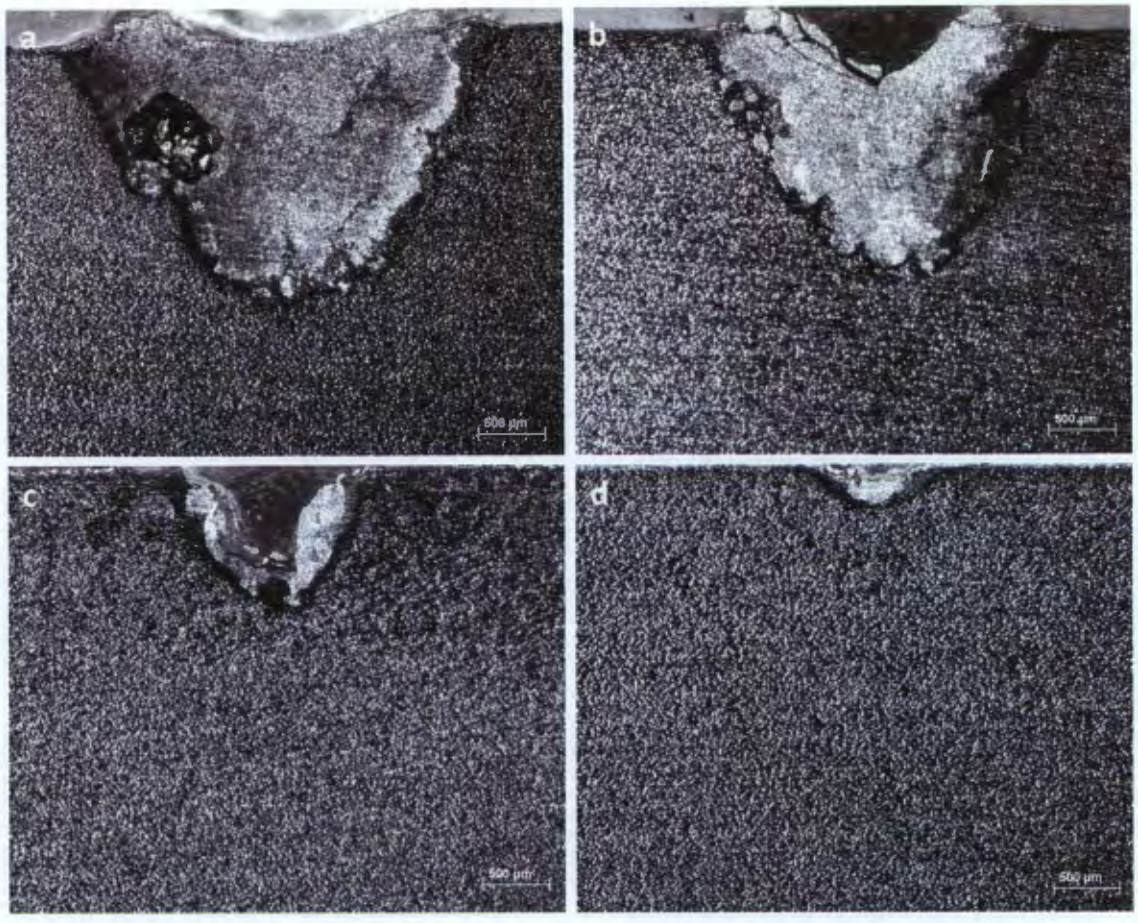

Figure 4.8: The effect of laser power (a)$1200W$, (b)$900W$, (c) $600W$ and (d) $300W$ on melt deptfor pulse duration of $1s$ and beam diameter $600\mu m$.

4.7 Combined effects of laser power and pulse duration on melt zone

In addition to knowing the effects that each laser parameter has on the process outcome, it is worth knowing the effects that a combination of laser parameters have on the process outcome. Table 4.1 is a list of the laser parameter combinations that are going to be discussed. The pulse duration is classified as either low or high according to its ranking in the pulse duration range irradiated for at a specific constant power. For instance, $2.5s$ was the longest pulse duration at a laser power of $1200W$ however, $10s$ was the longest pulse duration used for $300W$ laser irradiation. The cross-sections resulting from each combination are shown in Figures 4.9 – 4.12.

Table 4.1: Combinations of laser power and pulse duration.

Sample #	Combination	Power (W)	Time (s)	Energy (J)
3	Low t + high P	1200	0.1	120
36		1120	0.8	900
33	High t + high P	1200	2.5	3000
9	Low t + low P	300	1	300
12		600	0.1	60
30	High t + low P	460	6.5	2990
21		300	10	3000
18		600	5	3000

It has been shown that defects such as craters, porosity and cracking were found in different samples. Some of their severity varied with varying laser parameters. The ideal result in processes such as laser welding is a weld without defects. It is shown in Figures 4.9 and 4.10 that for short pulses with low and high laser power, the resulting MZ is relatively small. Figure 4.9 (a) suggests that when relatively larger melt pools without crater formation are desired, a combination of short pulses with high laser power is suitable. The high laser power increases the amount of absorbed energy. With the short pulses, the increased absorbed energy is greater than the energy losses associated with conduction and convection heat transfer. Therefore, there is more energy available to increase temperatures to the melting point thus enlarging the melt pool. This explains the difference in melt zones of Figure 4.9 (a) and (b). Even though both cross-sections in Figure 4.9 represent effects of short pulses of high laser power, Figure 4.9 (b) has the longer pulse of the lower laser power between the two. Therefore, the lower laser power decreases the absorbed energy. Furthermore, the longer pulse allows for the conduction/convection losses to increase, therefore leaving less energy available for increasing temperatures to the melting point thus enlarging the melt pool.

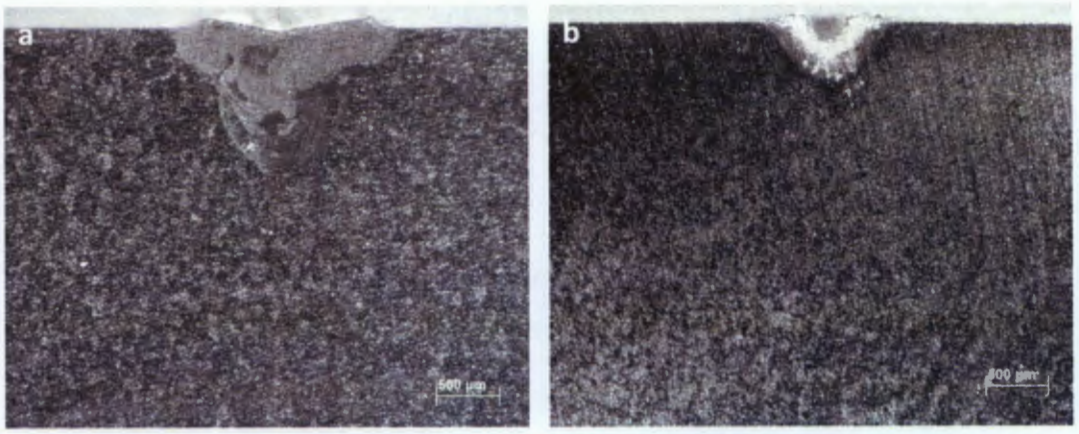

Figure 4.9: Laser irradiated titanium cross-sections resulting from a combination of low pulse duration and high laser power (a) $1200W$ and $0.1s$, (b) $1120W$ and $0.8s$.

As shown in Figure 4.10, the decrease in laser power results in smaller melt pools in comparison to those in Figure 4.9 where high laser power was used. As expected, the decrease in laser power resulted in a decrease in the amount of energy absorbed. Even though the pulses were short, the decrease in absorbed energy meant that the conduction/convection losses became significant. Therefore the areas where temperatures were increased to the melting point were limited. Figure 4.9 (a) and 4.10 (b) represent melt zones resulting from short pulses of high laser power within their respective figures. In Figure 4.9, Figure 4.9 (a) has the shortest pulse of the highest laser power. In Figure 4.10, Figure 4.10 (b) has the shortest pulse with the highest laser power. However, Figure 4.9 (a) exhibits a larger melt pool and less significant crater size than Figure 4.10 (b). The laser power can explain this difference. It was reported that short pulses of high laser power can cause spattering [56]. This is observed in Figure 4.10 (b). The crater formed in Figure 4.10 (b) is more significant in size because of the small melt pool that resulted from the lower laser power (than that of Figure 4.9 (a)). The higher laser power used in Figure 4.9 (a) resulted in an enlargement of the melt pool thus ensuring that the metal droplets expelled from the melt pool are returned to melt pool by falling onto molten regions.

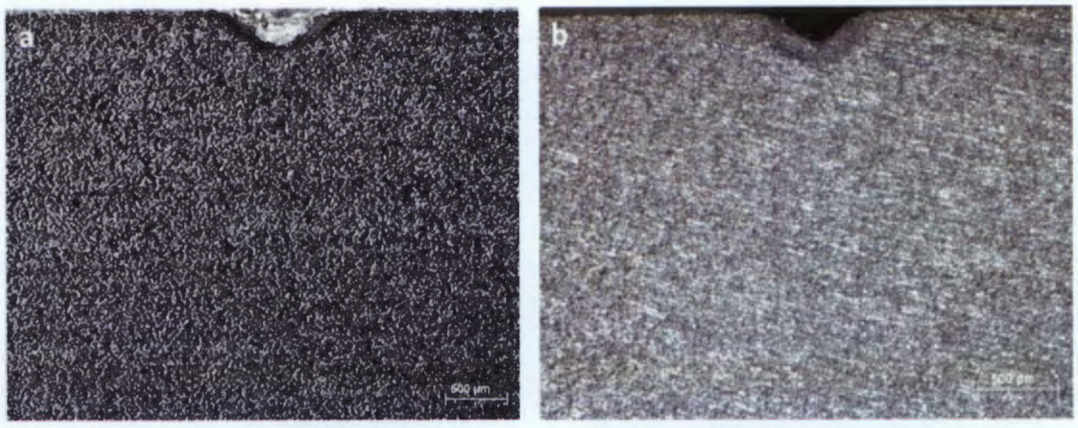

Figure 4.10: Laser irradiated titanium cross-sections resulting from a combination of short pulses and and low laser power (a) $300W$ and $1s$, (b) $600W$ and $0.1s$.

The result of long pulses with high laser power is shown in Figure 4.11. This combination yields a much larger melt pool, a larger crater and more cracking. The larger melt pool and crater are expected. The higher laser power translates into a higher energy density deposited at the sample surface. Therefore, this increases the amount of absorbable energy by the sample. Increased absorbed energy raises temperatures rapidly and results in a rapid propagation of the melt front into the sample. Therefore, this results in large melt pools. However, the large melt pool did not lead to shallow craters as explained for Figure 4.9 (a). The increased pulse duration resulted in prolonged interaction between the laser beam and the workpiece therefore causing metal vaporization significant enough to cause significant mass loss.

Figure 4.11: Laser irradiated titanium cross-section resulting from a combination of a long pulse and high laser power: $1200W$ and $2.5s$.

As shown in Figure 4.12, long pulses of low laser power yield narrower melt pools. The craters are also narrower and significantly deeper. There are cracks visible on cross-sections shown in Figure 4.12 (b) and (c). Porosity is observed on all cross-sections shown in Figure 4.12. The increased crater and melt pool depths were a result of the prolonged interaction between the laser beam and the workpiece. The difference in the melt pool sizes between that in Figure 4.11 and those in Figure 4.12 suggests that laser power has the effect of increasing the melt width. Both situations in Figures 4.11 and 4.12 are as a result of long pulses. However the melt pools in Figure 4.11 are significantly wider than those in Figure 4.12. Considering that the laser power in Figure 4.11 is higher than those used in Figure 4.12, it follows that the widening of the melt pool in Figure 4.11 may be due to increased laser power.

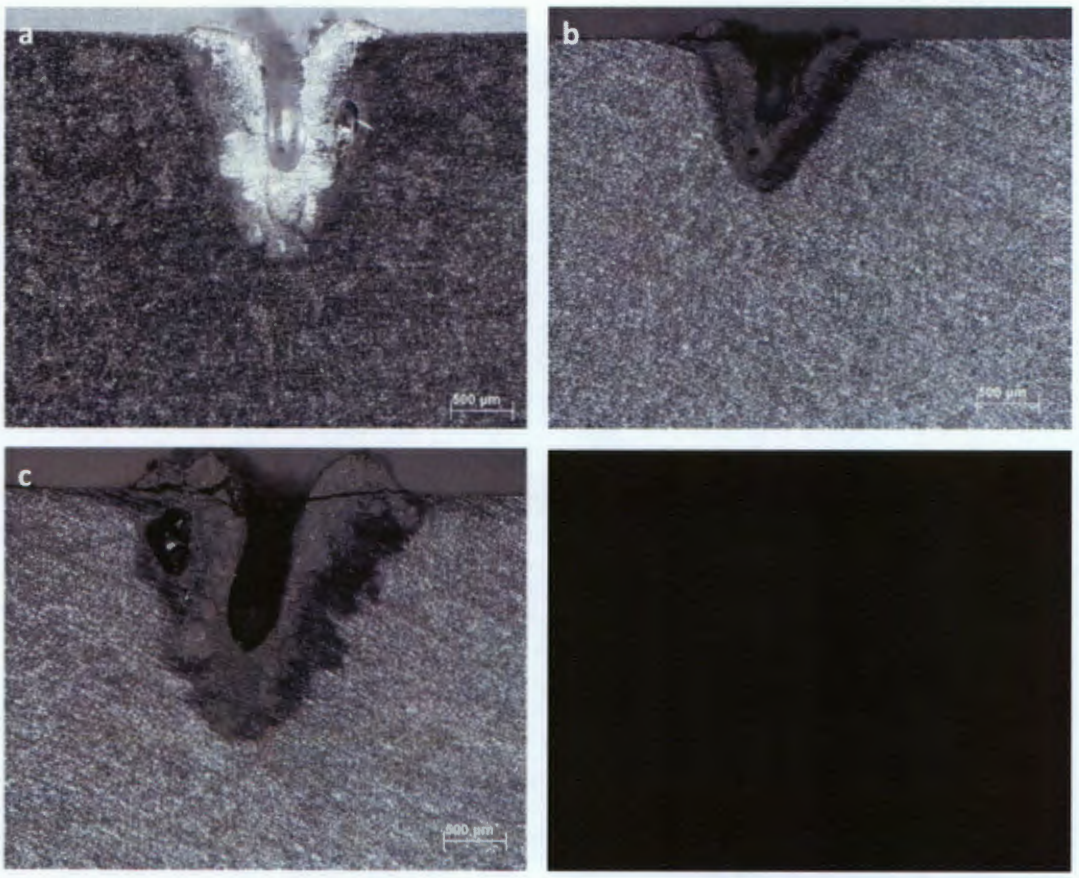

Figure 4.12: Laser irradiated titanium cross-sections resulting from a combination of high pulse duration and low laser power (a) $460W$ and $6.5s$, (b) $300W$ and $10s$, (c) $600W$ and 5.

The laser parametric study in subchapter 3.2 showed that the melt depth trends predicted by the adapted model were similar to those that had been predicted by other researchers.

The melt depth was approximated to increase with an increase in laser pulse duration, as well as with increasing laser power. However, the approximations were analytically-based. It is with Figures 4.7 and 4.8 that the approximated relationship between the melt depth and the laser parameters (power and pulse duration), is physically shown through experimental results. Even though the model cannot predict the presence of laser irradiation defects (porosity, cracking and craters), the results shown in Figures 4.7 and 4.8 validate the adapted model's prediction of melt depth increasing with increasing laser pulse duration and laser power.

4.8 Measured melt depths

The melt-depth measurements are plotted against laser irradiation conditions as shown in Figure 4.13. Since each condition was employed on three samples for reproducibility purposes, ideally the three samples should have identical cross-sections. However, there are differences between the measurements of the samples irradiated under the same conditions. These differences are suspected to be introduced during the metallographic preparation process. Grinding the cross-sections exactly to the centre of the laser beam-surface interaction plane was a difficult task. Therefore, in cases where the sample was ground beyond the centre of the laser beam-surface interaction plane, a smaller melt depth would be measured. So shown in Figure 4.13 are the maximum of each set of three samples subjected to one experimental condition.

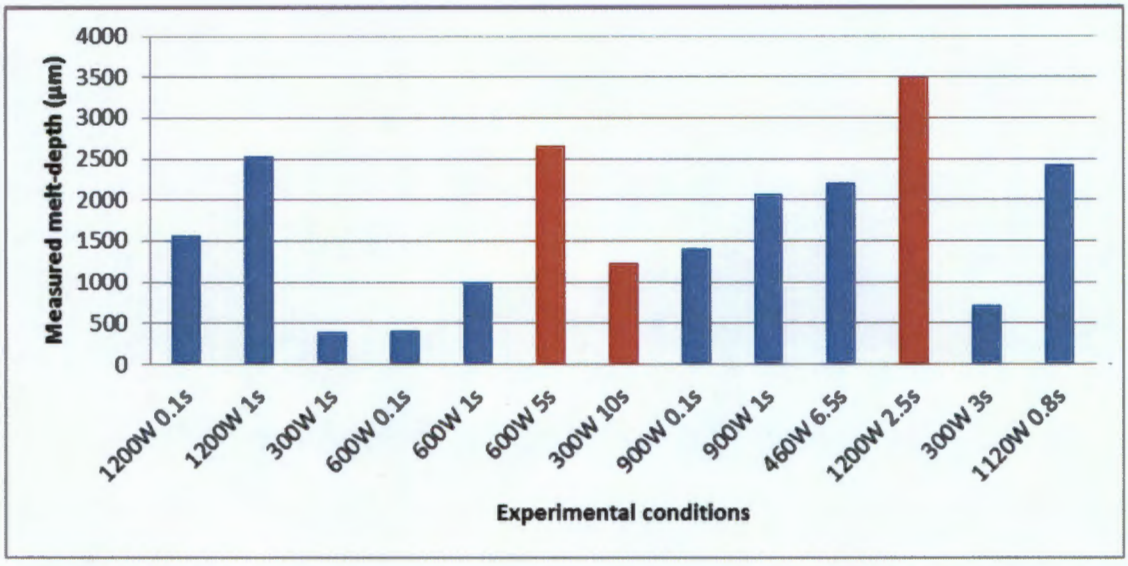

Figure 4.13: Showing measured melt depths for each experimental condition for titanium. The highlighted conditions are those that have equal pulse energy of 3000J

As already discussed, the effect of pulse duration (with constant laser power) on the melt depth is that the melt depth increases with increasing pulse duration. This is shown in Figure 4.13 with laser power kept constant at $300W, 600W, 900W$ and $1200W$. It is noted that laser power is only kept constant for either two or three pulse duration points (e.g. $0.1s$, $1s$ and $2.5s$ for $1200W$). Therefore, the data in Figures 4.7 and 4.13 cannot be used alone to conclude that increasing pulse duration increases the melt depth because of insufficient data points. However, when paired up with experimental work by other researchers [61], the data in Figures 4.7 and 4.13 can be used to suggest that indeed increasing pulse duration increases the melt depth.

The data points highlighted in red in Figure 4.13 represent melt depths produced under laser conditions that have laser pulse energy of $3000J$. Melt depths produced under different conditions but equal laser pulse energy, will not necessarily be equal. That laser pulse energy is distributed along the pulse duration; hence the energy concentration in that single pulse decreases. Therefore the longer the pulse, the less energy concentration that pulse will have thus the smaller the drilling effect will be. The laser condition with the highest laser beam intensity will have the greatest drilling effect, thus have the largest melt depth. This explains why the experimental condition $1200W$ $2.5s$ produces the largest melt depth of the three red-highlighted data points. The $3000J$ of pulse energy are distributed along a shorter pulse of only $2.5s$ as compared to those of $5s$ and $10s$ .The experimental condition $300W$ $10s$ produces the smallest melt depth of the three red-highlighted data points.

Based on the above explanation, it is interesting to note that the melt depths produced by experimental conditions $1200\,W$ $1s$ and $600W$ $5s$ are very similar even though the laser power ratio is 2:1. From laser intensity perspective, the experimental condition with the highest laser power should produce the deepest melt pool. However, the longer exposure time in the condition: $600W$ $5s$ compensates for the decreased drilling effect. It has been shown that an initial increase in pulse duration results in an increase in the melt depth. Again, this is owing to the longer interaction time between the laser beam and target surface and that the steady state conditions are not yet reached. The similarity between the melt depths produced by conditions $1200\,W$ $1s$ and $600W$ $5s$ suggests that combinations of high laser power with short pulses and low laser power with long pulses can yield the same melt depth. However, the reader is reminded in Figure 4.14 of the difference in the quality of the MZ produced by the two conditions discussed. The combination of high laser power with a short pulse yields MZ with much shallower craters and fewer cracks.

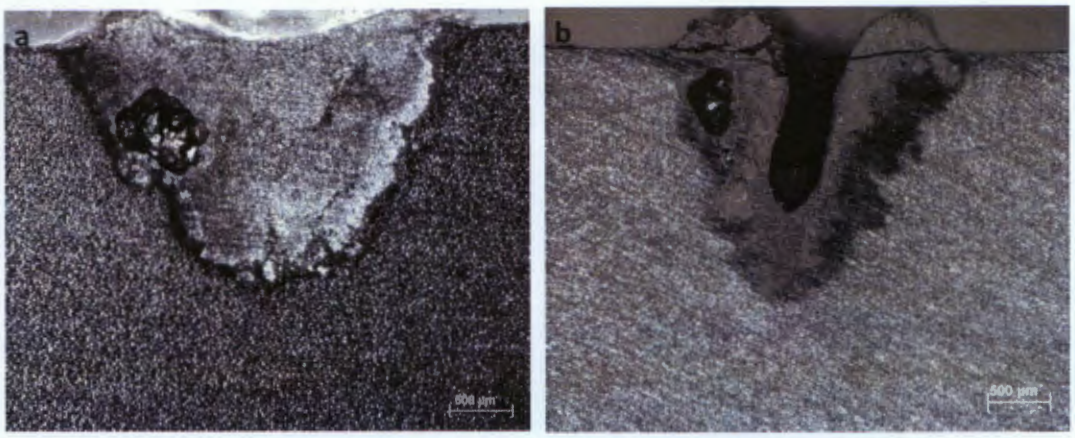

Figure 4.14: Cross-sections of titanium samples laser irradiated under conditions (a)$1200W$ $1s$ and (b) $600W$ $5s$. Both conditions produce melt-depths of similar measurement but different MZ quality.

4.9 Assessment of the adapted model's accuracy against experimental melt depth results

Figure 4.15 shows some of the experimental results superimposed onto the analytical results plots. The thermo-physical properties of CP titanium used in the model are given in Table 4.2.

Table 4.2: Thermophysical properties used in the analytical model of melt depth for CP titanium laser irradiation [10, 75]

Property	Value
Density (kg/m^3)	4425
Specific heat capacity ($J/kg.K$)	636
Thermal conductivity (solid phase) ($W/m.K$)	19.7
Absorption coefficient	0.43
Beta transus temperature (K)	1939
Melting temperature (K)	1163
Latent heat of fusion (J/kg)	3.9×10^5

As per the two research objectives addressing the research questions, an analytical model has been adapted from existing analytical models and is compared to the experimental results in Figure 4.15. The assessment of the error introduced by the adapted model is covered in subsequent paragraphs.

The general case in Figure 4.15 is that the adapted model seems to overestimate the measured data with increasing pulse duration. Also, the adapted model's accuracy shows a

slight improvement with increasing laser power, especially at shorter laser pulses. Therefore Figure 4.15 shows that there already is an error introduced by the adapted model at all specified laser pulses and power. From the above-mentioned trends, it is clear that the error introduced by the adapted model seems to increase and decrease with increasing laser pulse and increasing laser power respectively, with the error ranging from approximately 59% (0.1s at 1200W) at short laser pulses to 90% at long pulses (5s at 600W laser power). The trends observed in Figure 4.15 suggest that there could be a 'thermo-factor' (heat consumption factor) that is not accounted for in the model, but is present in the laser irradiation experiments. Since for constant laser power the approximation deteriorates with increasing pulse duration, it seems that the heat consuming factor becomes significant with increasing pulse duration. Also, the migration of the measured data points towards the calculated melt depth curve with increasing laser power suggests that there is something occurring as laser power is increased. Therefore, this 'thermo-factor' is a function of both laser power and pulse duration.

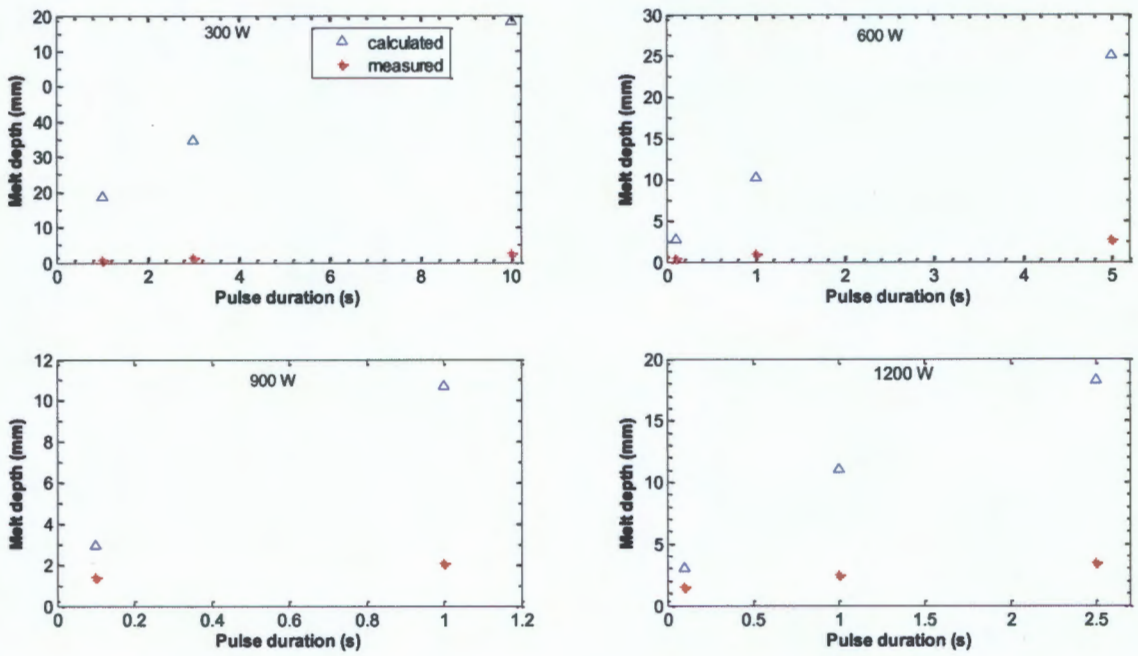

Figure 4.15: Comparison of the titanium laser irradiation experimental results to the calculated melt depth curves for different laser power and pulse duration.

Laser plasma is suspected to be the thermo-factor in question. Akman et al. [61] reported that the penetration depth (melt depth) increased linearly with peak power, however it was measured to be approximately constant after a certain peak power ($2kW$). They explained

this seizure of the penetration depth increase with the presence of laser plasma in the keyhole. The laser-beam-absorbing nature of laser plasma restricts the irradiated target from receiving all of the laser beam's energy. Since it has also been reported that laser plasma grows with increasing laser power and pulse duration [69], it follows that its laser-beam-absorbing effects increase with laser power and pulse duration as well. Therefore, with increasing laser power and pulse duration, laser plasma increases thus absorbs the laser beam's energy that would otherwise be used to increase the melt depth. This potentially explains the trend observed in Figure 4.15 where the accuracy of the approximation deteriorated with increasing pulse duration. However, it does not explain the improvement of the approximation accuracy with increasing laser power. The accuracy with which the calculations approximate the measured depths improves significantly with short laser pulses. Since laser plasma is reported for long pulse durations, it is possible that laser plasma must have been absent in the experiments at short laser pulses (i.e.$0.1s$).

The given explanation holds true provided that laser plasma was present during the experiments in this study. Figure 4.16 is a plot of the measured melt depth and width as a function of laser power. The experimental conditions used in Figure 4.16 are: $300W, 600W, 900W$ and $1200W$ at $1s$ and $1120W$ at $0.8s$. For illustrative purposes, $0.8s$ is regarded as being similar to $1s$. Therefore the effects of laser power with 'constant' pulse duration on melt depth and width are shown in Figure 4.16. As illustrated in Figure 4.16, at lower laser power (up to $1120W$) the melt depth increases linearly with laser power. This relationship changes at $1120W$ and $1200W$ and the melt depth increases slightly. The amount of data in Figure 4.16 is not enough to draw conclusions about the behaviour of the melt depth beyond laser power levels of $1200W$, but it suggests that at higher laser power the melt depth increase becomes limited. However, the melt width continues to increase linearly at all laser power values plotted in Figure 4.16. Unlike the melt depth, the data in Figure 4.16 does not suggest the limitation of melt width increase with increasing laser power. The same behaviour has been reported by Akman et al. [61]. They explain the observations made in Figure 4.16 with plasma absorption of laser beam. Plasma absorption is very strong at the top of the weld where the available laser energy is high, this leads to enlarged melt width and limitation in the melt depth increase [61]. This not only proves the presence of laser plasma during the experiments at higher laser power levels, but also shows that the effects of laser plasma increase with increasing laser power. Therefore, this is consistent with the author's claim that the presence of laser plasma seizes the deepening of the melt pool hence the tendency of the measured melt depth getting farther away from that which is calculated, with increasing laser power and pulse duration.

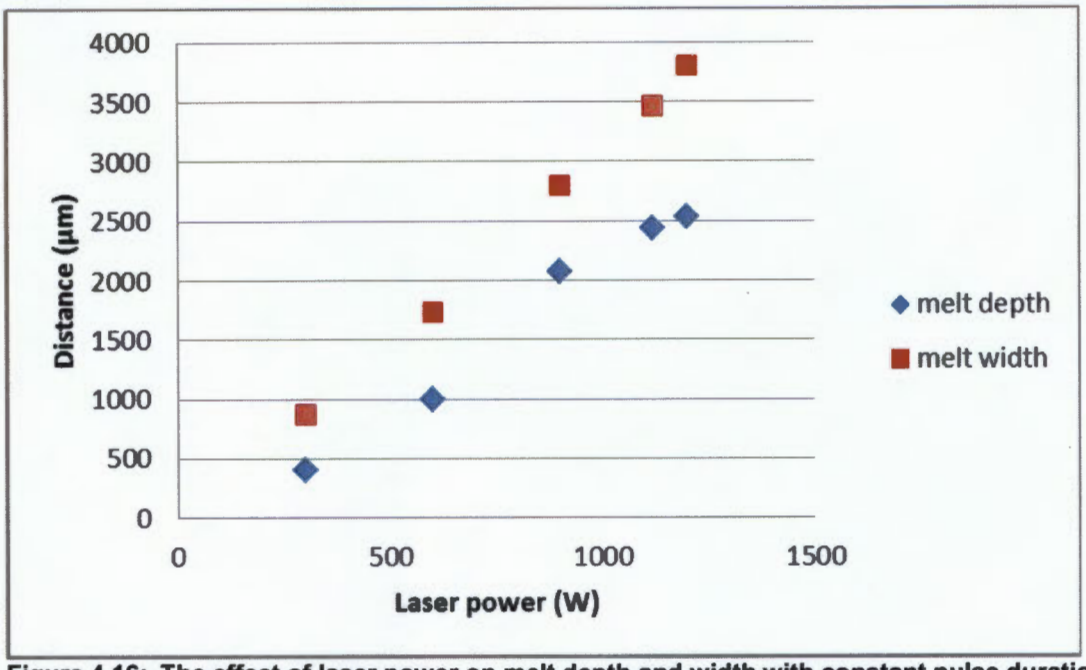

Figure 4.16: The effect of laser power on melt depth and width with constant pulse duration.

4.10 Microstructure results and discussion

The purpose of microstructure characterization is to identify the different isotherms characteristic of titanium phase transformations during laser irradiation. The identification of these isothermal boundaries allows for the measurement of the different zones that are characteristic of different phase transformations. These are the measurements that will be compared with the analytical results.

Figure 4.17 presents the microstructure of the pre-laser irradiated titanium samples. This starting microstructure is comprised of equiaxed α grains.

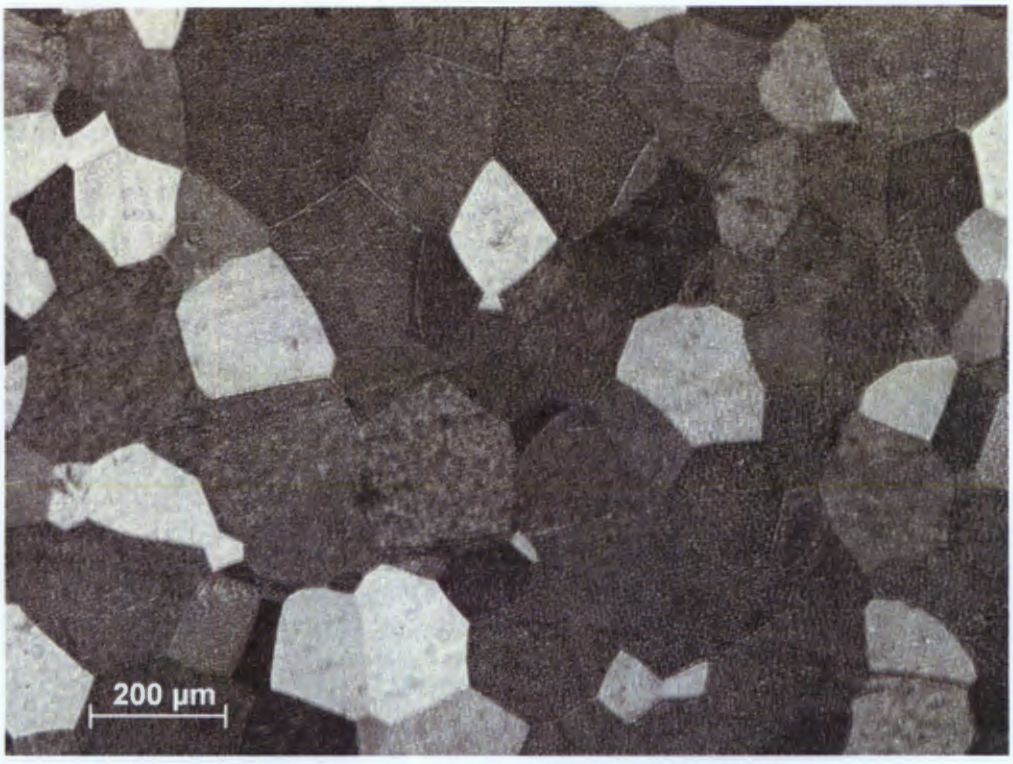

Figure 4.17: Microstructure of titanium samples before laser irradiation.

Figure 4.18 presents the microstructure of a cross-section of a titanium sample laser irradiated at $900W$ laser power and $0.1s$ pulse duration. Three zones with different microstructures are observed in the cross-section shown in Figure 4.18. These zones represent regions in the sample that experienced different phase transformations thus different cooling rates. Each zone is clearly separated from the other by boundaries believed to be isotherms.

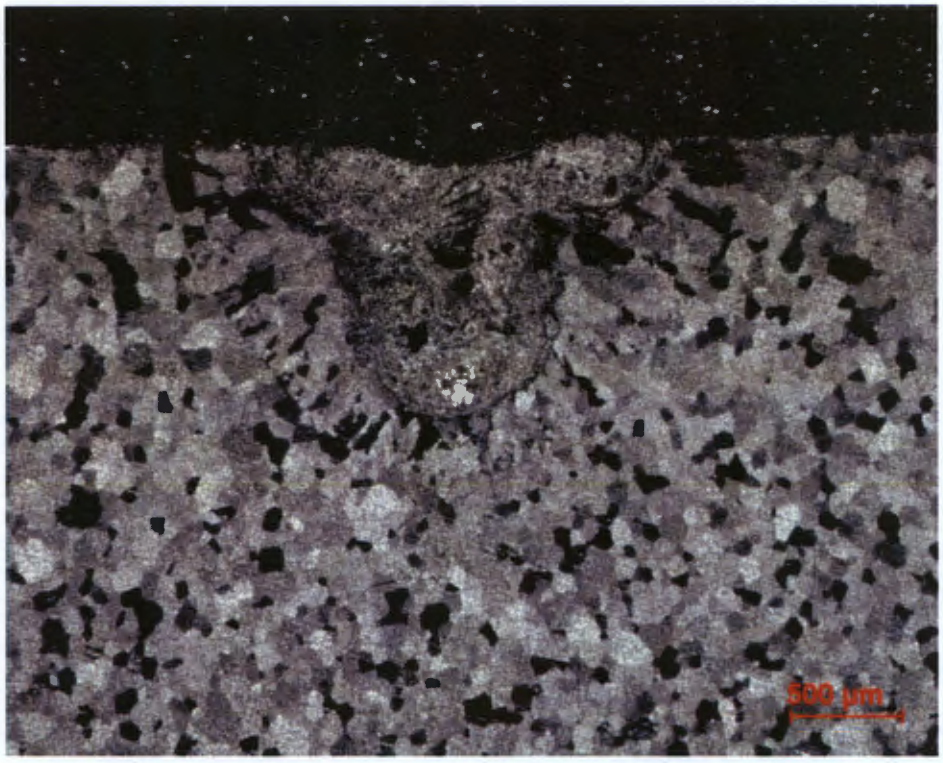

Figure 4.18: Cross-section of titanium sample irradiated under laser conditions: of $900W$ and $0.1s$.

Figure 4.19 is given as a higher magnification of the three zones with Figure 4.20 giving a closer look at the zones in Figure 4.19. Figure 4.20 (a) represents the region closest to the laser irradiated surface. It is characterised by a needle-like microstructure that is characteristic of a region that has been heated to above the melting point, solidified as β and underwent diffusionless transformation to α'. Therefore this region can be referred to as the melt zone (MZ). Shown in Figure 4.20 (b) is the region adjacent to the MZ and unlike the MZ, it is composed of irregularly-shaped columnar-like grains. When compared to the equiaxed microstructure shown in Figure 4.17, it is clear that this region has been thermally affected. Consequently, it is referred to as the heat affected zone (HAZ).The microstructure in Figure 4.20 (c) is of the region furthest away from the laser irradiated surface and adjacent to the HAZ. The similarity between the microstructure in Figure 4.20 (c) and that in Figure 4.17 justifies the region in Figure 4.19 (c) being referred to as the thermally unaffected zone (TUZ).

As already pointed out, there are two isothermal boundaries separating the three microstructurally different zones. The microstructure in the HAZ is consistent with microstructure that has been subjected to temperatures beyond the T_β thus underwent a massive transformation from $\beta - \alpha$ upon cooling. There is a decline in cooling rates between the MZ and the TUZ. Therefore, it follows that the MZ experienced the highest cooling rates as compared to the HAZ, hence the difference in the final microstructure even though they both were once β before the transformation to α upon cooling. Since the HAZ is believed to have not been heated up to the melting point, the isothermal boundary separating the MZ from the HAZ is thus believed to be the T_m.

According to other literature the isothermal boundary between the HAZ and TUZ can either be T_β [40, 54], $T_{\alpha-\beta}$ or $T_{annealing/recrystallization}$ [54]. Elmer et al. [54] reported an annealed and recrystallized microstructure adjacent to the TUZ during arc welding. Therefore, according to their findings, the boundary seen to separate the TUZ from the HAZ in Figures 4.18 and 4.19, should be regarded as the annealing temperature isotherm. However, that cannot be the case in this study. For annealing to occur, there needs to be stored strain energy in the material. This stored strain energy would be a product of cold work. Since laser irradiation was carried out on samples with an equiaxed microstructure, the driving force for annealing and recrystallization was absent. Therefore, the possibility of having the TUZ/HAZ boundary considered as the annealing or recrystallization temperature isotherm is ruled out. This leaves two options as to what temperature the TUZ/HAZ boundary represents. Elmer et al. [54] also reported a region of partial transformation between the recrystallized and fully transformed regions inside the HAZ. Since the possibility of both the annealed and recrystallized regions has been ruled out, it follows that according to the findings of Elmer et al. [54] the TUZ/HAZ boundary should be the $T_{\alpha-\beta}$. However, the abrupt morphology change from the TUZ to HAZ is not consistent with microstructure that would have partially transformed to β upon cooling. If ever the TUZ/HAZ boundary represented the $T_{\alpha-\beta}$, there would be a gradient in the degree of phase transformation. Therefore, there would not be as an abrupt change from the microstructure in the TUZ to that in the HAZ. Instead, there would be evidence of grain refinement in HAZ regions closest to the TUZ/HAZ boundary [54]. The abrupt morphology change is consistent with a region that has been subjected to temperatures above the T_β on heating [40]. The irregularly-shaped and elongated-looking grains are consistent with microstructure that has undergone massive transformation [55]. Massive transformation is associated with high cooling rates. Considering that the samples were subjected to high cooling rates, the microstructure in the HAZ is consistent with that which has been subjected to temperatures above the T_β on heating, and underwent massive transformation upon cooling.

4.11 Assessment of the adapted model's accuracy against experimental HAZ results

Figure 4.21 shows a comparison of the measured HAZ depths to those calculated at T_β isotherm. Similar to what was observed in Figure 4.15, the accuracy of the adapted model deteriorates with increasing pulse duration. The comparison therefore reveals that there is better agreement at short laser pulses than at longer laser pulses. The error introduced by the adapted model in approximating the HAZ was approximately 17% at $0.1s$ and $1200\ W$ as opposed to the 59% error introduced when calculating the melt depth for the same laser parameters. This could suggest that the accuracy of the adapted model is affected by temperature thus improves with lower temperatures, given that $T_\beta < T_m$. The speculations of laser plasma effects are not only limited to melt depths but are also employed in the behaviour of the HAZ depth with increasing laser power

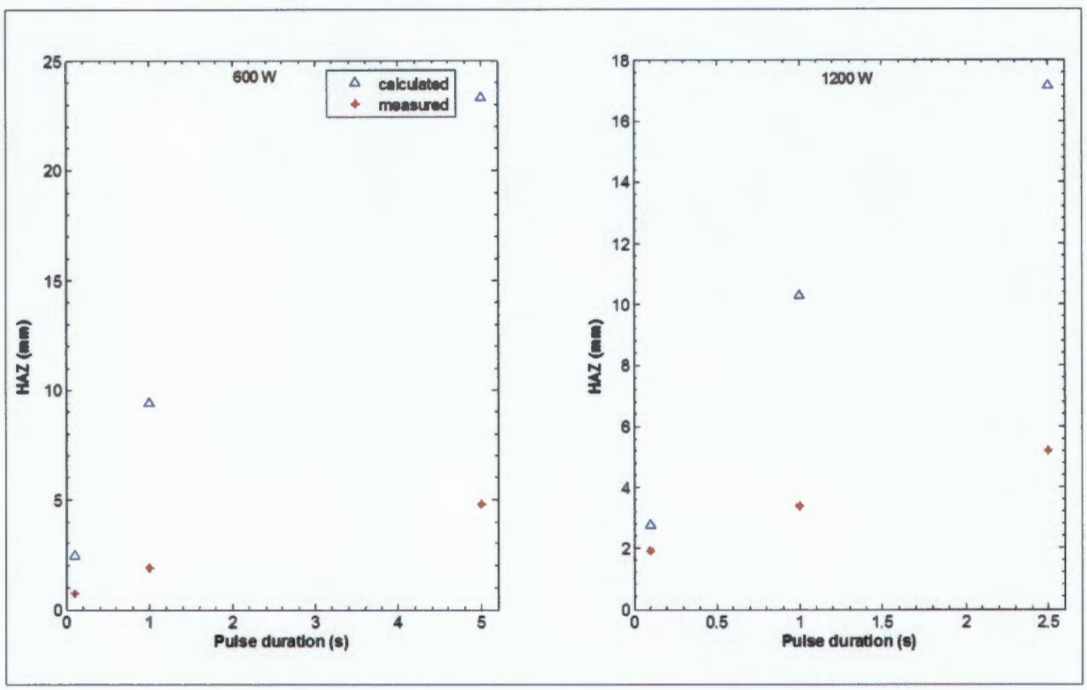

Figure 4.21: A comparison between the measured and calculated HAZ depths for 300 W and 1200 W.

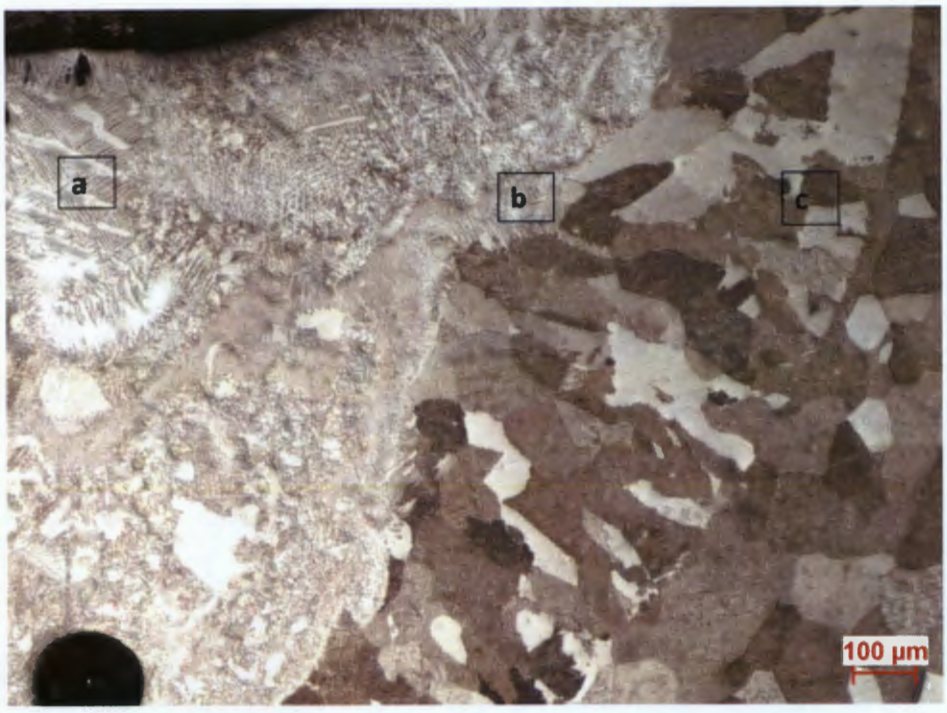

Figure 4.19: Cross-section showing three different microstructures after laser irradiating titanium sample under conditions of $900W$ and $0.1s$.

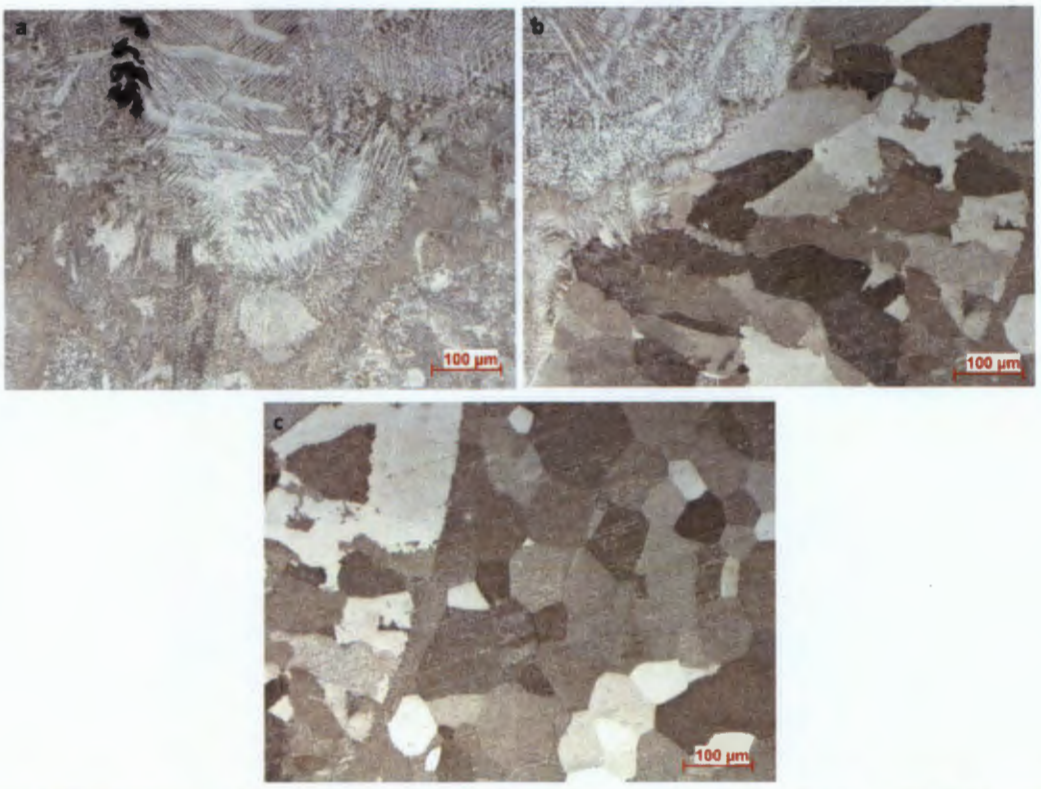

Figure 4.20: Optical microscope images of a titanium sample laser irradiated under conditions $900W$ and $0.1s$ (a) the MZ, (b) the MZ and HAZ separated by the T_m isotherm and (c) the HAZ and TUZ separated by the T_β.

5 CONCLUSIONS

As per the objectives of this study and research questions, the existing analytical models were adapted in this study in order to approximate the temperature fields and subsequently approximate the melt depth inside a single-pulsed laser irradiated titanium sample. When compared to a couple of laser spot welding results of existing literature, the adapted model introduced errors that range from 45% at laser operating parameter ranges of $1500 - 5000\,W/mm^2$laser beam intensity, $3ms$ pulse duration and $428\mu m$ beam diameter, to 52% at laser operating parameter ranges of $2.5 - 3.5\,J$ laser beam energy, $2 - 4\,ms$ pulse duration and $428\mu m$ beam diameter. When compared to the experimental results of this study, the adapted model introduced errors in the range of 59% at laser parameters $0.1s$ and $1200W$ to 90% at laser parameters $5s$ and $600W$.

The measured results revealed that the accuracy of the analytical model developed in this study improved with short pulses and increased laser power. At increased laser power and pulse durations, the suspected presence of laser plasma slowed down the growth of the melt and HAZ depth. Since the model does not account for laser plasma, the accuracy thereof deteriorated with increased pulse duration at constant laser power, and at increased pulse duration and increasing laser power.

The macrostructure results of laser pulsed irradiation of commercially pure titanium showed that laser power and pulse duration have an effect on the MZ shape and size. Laser pulse and laser power are directly proportional to the penetration depths of the heat effects. The melt depth increased with either increasing laser pulse or increasing laser power. The control of both parameters yields different laser irradiation results. The combination of short pulses with high laser power produced a MZ with minimal mass loss in the form of craters and fewer cracks than the other combinations. Long pulses combined with high laser power resulted in a damaged MZ. The damage was in the form of deepened craters thus indicating increased mass losses. In addition to deepened craters, cracks and pores attributed to the damaged MZ. The differences between the latter combination of long pulses with high laser power, and that of long pulses with low laser power are the MZ shape and size. The combination of long pulses with low laser power produced narrower MZ's. The combination of short pulses with low laser power produced the smallest MZ's out of all four combinations. However, relative to the MZ size, the mass loss was significant with slightly increased laser power. An example of the latter is the MZ produced by $300W$ and $600W$ with pulse duration of $0.1s$. These two conditions both fall under the combination of short pulses and low laser power but, the crater depth was more significant with the laser condition of $600W$. As a result, it would seem that the crater size increases with increasing

laser power. However, the macro results also showed that the crater size decreased from $900W$ to $1200W$ for pulse duration of $1s$. Therefore the laser parameter combinations that produced the smallest craters are the short pulses with both high and low laser power.

The microstructure results showed that the MZ was composed of needle-like microstructures, and that the HAZ was composed mainly of columnar grain microstructures. From the micro results the MZ and HAZ were measureable.

6 RECOMMENDATIONS

Based on the limitations and discrepancies observed in this study, the following recommendations are made:

- Since short pulses of high laser power result in melt zones of better quality, an improvement of the model's accuracy in these operating conditions is valuable. This will result in a model that can provide operating parameters that yield defect-free melt zones
- A method must be devised to allow for the measuring of temperature gradients during the laser irradiation experiments. Considering that mounting thermocouples inside the workpiece may present difficulty with ensuring the connection of the thermocouple tip with the workpiece, it may be wise to mount the thermocouples on the surface. This will measure the radial temperature gradient. It will be up to the investigator to find a link between radial temperature gradients and those that exist along the depth of the workpiece.
- For some unknown reason, the keller's reagent proved to be problematic during cross-sectional surface etching. Therefore, it might be worth it to prepare blank titanium samples on which polishing and etching runs will be done. Once the method of revealing the titanium microstructure has been discovered and tested, it can be applied to the laser-irradiated titanium samples. This will avoid mistakes that lead to repeating the polishing step thus ending up with a cross-section that is not a true reflection of the cross-section through the centre of the melt zone.

7 REFERENCES

1. Siva Shanmugam, N., G. Buvanashekaran, and K. Sankaranarayanasamy, *Some studies on weld bead geometries for laser spot welding process using finite element analysis.* Materials & Design. **34**: p. 412-426.
2. Rykalin, N., *The solutions of thermal processes during welding.* 1951, Moscow.
3. Sun, Z., et al., *Effect of laser surface remelting on the corrosion behavior of commercially pure titanium sheet.* Materials Science and Engineering: A, 2003. **345**(1): p. 293-300.
4. Langlade, C., et al., *Surface modification and tribological behaviour of titanium and titanium alloys after YAG-laser treatments.* Surface and Coatings Technology, 1998. **100**: p. 383-387.
5. Bereznai, M., et al., *Surface modifications induced by ns and sub-ps excimer laser pulses on titanium implant material.* Biomaterials, 2003. **24**(23): p. 4197-4203.
6. Liu, X., P.K. Chu, and C. Ding, *Surface modification of titanium, titanium alloys, and related materials for biomedical applications.* Materials Science and Engineering: R: Reports, 2004. **47**(3): p. 49-121.
7. Xin, H., S. Mridha, and T. Baker, *The effect of laser surface nitriding with a spinning laser beam on the wear resistance of commercial purity titanium.* Journal of materials science, 1996. **31**(1): p. 22-30.
8. Mazumder, J. and W. Steen, *Heat transfer model for CW laser material processing.* Journal of applied physics, 1980. **51**(2): p. 941-947.
9. Ji, Z. and S. Wu, *A Simple Finite Element Method for Computing Temperature Field of Laser-Heated Sheet Metal.* JOURNAL-NORTHWESTERN POLYTECHNICAL UNIVERSITY, 1997. **15**: p. 207-211.
10. Xie, J. and A. Kar, *Mathematical modeling of melting during laser materials processing.* Journal of applied physics, 1997. **81**(7): p. 3015-3022.
11. Yilbas, B. and S. Shuja, *Heat transfer analysis of laser heated surfaces:conduction limited case.* Applied Surface Science, 1997. **108**(1): p. 167-175.
12. Costa, A., et al., *Analysis of beam material interaction in welding of titanium with fiber lasers.* Materials and Manufacturing Processes, 2007. **22**(7-8): p. 798-803.
13. Weckman, D., H. Kerr, and J. Liu, *The effects of process variables on pulsed Nd: YAG laser spot welds: Part II. AA 1100 aluminum and comparison to AISI 409 stainless steel.* Metallurgical and Materials Transactions B, 1997. **28**(4): p. 687-700.
14. Tokarev, V.N. and A.F.H. Kaplan, *An analytical modeling of time dependent pulsed laser melting.* Journal of applied physics, 1999. **86**(5): p. 2836-2846.
15. Shen, Z., et al., *Mathematical modeling of laser induced heating and melting in solids.* Optics & Laser Technology, 2001. **33**(8): p. 533-537.
16. El-Nicklawy, M., A. Hassan, and S.E.S. Abd El-Ghany, *On melting a semi-infinite target using a pulsed laser.* Optics & Laser Technology, 2000. **32**(3): p. 157-164.
17. Gagliano, F.P., R.M. Lumley, and L.S. Watkins, *Lasers in industry.* Proceedings of the IEEE, 1969. **57**(2): p. 114-147.
18. Tabata, N., S. Yagi, and M. Hishii, *Present and future of lasers for fine cutting of metal plate.* Journal of materials processing technology, 1996. **62**(4): p. 309-314.
19. Tian, Y., et al., *Research progress on laser surface modification of titanium alloys.* Applied Surface Science, 2005. **242**(1): p. 177-184.
20. Pleshakov, E., Y. Senyavs' kyi, and R. Filip, *Laser Surface Modification of Ti-6Al-4V Alloy with Silicon Carbide.* Materials Science, 2002. **38**(5): p. 646-652.
21. Molian, P.A. and L. Hualun, *Laser Cladding of Ti-6Al-4V with BN for Improved Wear Performance.* Wear, 1989. **130**(2): p. 337-352.
22. Quan, H., *Accession of Titanium as an Aircraft Material--A Current View.* 1981, DTIC Document.

23. Cao, X. and M. Jahazi, *Effect of welding speed on butt joint quality of Ti6Al4V alloy welded using a high-power Nd: YAG laser.* Optics and Lasers in Engineering, 2009. **47**(11): p. 1231-1241.
24. Jiang, P., et al., *Wear resistance of a laser surface alloyed Ti6Al4V alloy.* Surface and Coatings Technology, 2000. **130**(1): p. 24-28.
25. Yerramareddy, S. and S. Bahadur, *The Effect of Laser Surface Treatments on the Tribological Behavior of Ti-6Al-4V.* Wear, 1992. **157**(2): p. 245-262.
26. Budinski, K.G., *Tribological properties of titanium alloys.* Wear, 1991. **151**(2): p. 203-217.
27. Waterhouse, R.B. and M.H. Wharton, *Titanium and tribology.* Industrial Lubrication and Tribology, 1974. **26**(1): p. 20-23.
28. Suzuki, K. and Y. Nakamoto, *Experience with titanium heat exchangers in oil refineries.* Japan. Materials Performance, 1981. **20**(6): p. 3-26.
29. Montgomery, J.S. and M.G.H. Wells, *Titanium armor applications in combat vehicles.* JOM Journal of the Minerals, Metals and Materials Society, 2001. **53**(4): p. 29-32.
30. Lathabai, S., B. Jarvis, and K. Barton, *Comparison of keyhole and conventional gas tungsten arc welds in commercially pure titanium.* Materials Science and Engineering: A, 2001. **299**(1): p. 81-93.
31. Malik, A.U. and P.C.M. Kutty. *Corrosion and material selection in desalination plants.* in *Proceedings of the Seminar on Operation and Maintenance of Desalination Plants, SWCC.* 1992.
32. Kasemo, B., *Biocompatibility of titanium implants: surface science aspects.* The Journal of prosthetic dentistry, 1983. **49**(6): p. 832.
33. Kodama, T., *[Study on biocompatibility of titanium alloys].* Kokubyo Gakkai zasshi. The Journal of the Stomatological Society, Japan, 1989. **56**(2): p. 263.
34. Schwager, K., *Titanium as a biomaterial for ossicular replacement: results after implantation in the middle ear of the rabbit.* European archives of oto-rhino-laryngology, 1998. **255**(8): p. 396-401.
35. Li, J., *Behaviour of titanium and titania-based ceramics in vitro and in vivo.* Biomaterials, 1993. **14**(3): p. 229-232.
36. Maeland, A., G. Libowitz, and J. Lynch, *Hydride formation rates of titanium-based BCC solid solution alloys.* Journal of the Less Common Metals, 1984. **104**(2): p. 361-364.
37. Collings, E., *Materials properties handbook: titanium alloys*. 1994: ASM International (OH).
38. Worner, H., *Thermoelectric Properties of Titanium with Special Reference to the Allotropic Transformation.* Australian Journal of Chemistry, 1951. **4**(1): p. 62-83.
39. Moiseyev, V.N., *Titanium alloys: Russian aircraft and aerospace applications.* Vol. 5. 2005: CRC.
40. Liu, H., et al., *Microstructural evolution of fusion zone in laser beam welds of pure titanium.* Materials Characterization, 2011. **65**(0): p. 1-7.
41. Danielson, P., R. Wilson, and D. Alman, *Microstructure of titanium welds.* Advanced materials & processes, 2003. **161**(2): p. 39.
42. Santos, E.C., et al., *Laser gas nitriding of pure titanium using CW and pulsed Nd: YAG lasers.* Surface and Coatings Technology, 2006. **201**(3): p. 1635-1642.
43. Fu, Y. and A.W. Batchelor, *Laser nitriding of pure titanium with Ni, Cr for improved wear performance.* Wear, 1998. **214**(1): p. 83-90.
44. Watanabe, I. and D.S. Topham, *Laser welding of cast titanium and dental alloys using argon shielding.* Journal of Prosthodontics, 2006. **15**(2): p. 102-107.
45. Sjogren, G., M. Andersson, and M. Bergman, *Laser welding of titanium in dentistry.* Acta Odontologica, 1988. **46**(4): p. 247-253.
46. Wang, R. and G. Welsch, *Joining titanium materials with tungsten inert gas welding, laser welding, and infrared brazing.* The Journal of prosthetic dentistry, 1995. **74**(5): p. 521-530.

47. Yamagishi, T., M. Ito, and Y. Fujimura, *Mechanical properties of laser welds of titanium in dentistry by pulsed Nd: YAG laser apparatus.* The Journal of prosthetic dentistry, 1993. **70**(3): p. 264-273.
48. Roggensack, M., M. Walter, and K. Boning, *Studies on laser-and plasma-welded titanium.* Dental Materials, 1993. **9**(2): p. 104-107.
49. Buddery, A., et al., *The effect of contamination on the metallurgy of commercially pure titanium welded with a pulsed laser beam.* Journal of materials science, 2011. **46**(8): p. 2726-2732.
50. Baba, N. and I. Watanabe, *Penetration depth into dental casting alloys by Nd: YAG laser.* Journal of Biomedical Materials Research Part B: Applied Biomaterials, 2004. **72**(1): p. 64-68.
51. Lee, W.B., et al., *Microstructural investigation of friction stir welded pure titanium.* Materials Letters, 2005. **59**(26): p. 3315-3318.
52. Sun, Z. and J. Ion, *Laser welding of dissimilar metal combinations.* Journal of materials science, 1995. **30**(17): p. 4205-4214.
53. Yunlian, Q., et al., *Electron beam welding, laser beam welding and gas tungsten arc welding of titanium sheet.* Materials Science and Engineering: A, 2000. **280**(1): p. 177-181.
54. Elmer, J.W., J. Wong, and T. Ressler, *Spatially resolved X-ray diffraction phase mapping and alpha-beta-alpha transformation kinetics in the heat-affected zone of commercially pure titanium arc welds.* Metallurgical and Materials Transactions A, 1998. **29**(11): p. 2761-2773.
55. Li, C., et al., *Fiber laser-GMA hybrid welding of commercially pure titanium.* Materials & Design, 2009. **30**(1): p. 109-114.
56. Kelkar, G., *PULSED LASER WELDING.* 2000. **3**: p. 256-262.
57. Chikarakara, E., S. Naher, and D. Brabazon, *High speed laser surface modification of Ti6Al4V.* Surface and Coatings Technology, 2012. **206**(14): p. 3223-3229.
58. Bertrand, C., et al., *Effect of the combination of different welding parameters on melting characteristics of grade 1 titanium with a pulsed Nd-Yag laser.* Lasers in Medical Science, 2007. **22**(4): p. 237-244.
59. Covelli, L., et al., *Surface microstructure of titanium irradiated by Nd: YAG pulsed laser in presence of carbon and nitrogen.* Surface and Coatings Technology, 1996. **78**(1): p. 196-204.
60. Ming, G., Z. Xiaoyan, and H. Qianwu, *Effects of gas shielding parameters on weld penetration of CO2 laser-TIG hybrid welding.* Journal of materials processing technology, 2007. **184**(1): p. 177-183.
61. Akman, E., et al., *Laser welding of Ti6Al4V titanium alloys.* Journal of materials processing technology, 2009. **209**(8): p. 3705-3713.
62. Robert, A. and T. Debroy, *Geometry of laser spot welds from dimensionless numbers.* Metallurgical and Materials Transactions B, 2001. **32**(5): p. 941-947.
63. Chang, W.S. and S.J. Na, *Prediction of laser-spot-weld shape by numerical analysis and neural network.* Metallurgical and Materials Transactions B, 2001. **32**(4): p. 723-731.
64. Kawahito, Y., M. Kito, and S. Katayama, *In-process monitoring and adaptive control for laser spot and seam welding of pure titanium.* J. Laser Micro/Nanoeng, 2006. **1**(3): p. 269-274.
65. Cline, H. and T.R. Anthony, *Heat treating and melting material with a scanning laser or electron beam.* Journal of applied physics, 1977. **48**(9): p. 3895-3900.
66. Assuncao, E., S. Williams, and D. Yapp, *Interaction time and beam diameter effects on the conduction mode limit.* Optics and Lasers in Engineering, 2012. **50**(6): p. 823-828.
67. Montross, C.S., et al., *Laser shock processing and its effects on microstructure and properties of metal alloys: a review.* International Journal of Fatigue, 2002. **24**(10): p. 1021-1036.

68. Szymanski, Z., J. Kurzyna, and W. Kalita, *The spectroscopy of the plasma plume induced during laser welding of stainless steel and titanium.* Journal of Physics D: Applied Physics, 1999. **30**(22): p. 3153.
69. Sankaranarayanan, S. and A. Kar, *Nonlinear effects of laser-plasma interaction on melt-surface temperature.* Journal of Physics D: Applied Physics, 1999. **32**(7): p. 777.
70. Dowden, J., P. Kapadia, and N. Postacioglu, *An analysis of the laser-plasma interaction in laser keyhole welding.* Journal of Physics D: Applied Physics, 2000. **22**(6): p. 741.
71. Suder, W. and S. Williams, *Investigation of the effects of basic laser material interaction parameters in laser welding.* Journal of laser Applications, 2012. **24**(3): p. 032009.
72. Abd El-Ghany, S.E.S., *The temperature profile in the molten layer of a semi-infinite target induced by irradiation using a pulsed laser.* Optics & Laser Technology, 2001. **33**(8): p. 539-551.
73. Lee, J.Y., et al., *Mechanism of keyhole formation and stability in stationary laser welding.* Journal of Physics D: Applied Physics, 2002. **35**(13): p. 1570.
74. Semak, V. and A. Matsunawa, *The role of recoil pressure in energy balance during laser materials processing.* Journal of Physics D: Applied Physics, 1999. **30**(18): p. 2541.
75. Momin, O., S. Shuja, and B. Yilbas, *Laser heating of titanium and steel: Phase change at the surface.* International Journal of Thermal Sciences, 2012. **54**: p. 230-241.
76. He, X., P. Fuerschbach, and T. DebRoy, *Heat transfer and fluid flow during laser spot welding of 304 stainless steel.* Journal of Physics D: Applied Physics, 2003. **36**(12): p. 1388.
77. Jouvard, J., K. Girard, and O. Perret, *Keyhole formation and power deposition in Nd: YAG laser spot welding.* Journal of Physics D: Applied Physics, 2001. **34**(18): p. 2894.
78. Liu, J., et al., *Joint strength of laser-welded titanium.* Dental Materials, 2002. **18**(2): p. 143-148.
79. Kharkhin, V., *Effect of Surface Tension on the Formation of the Weld Pool in Welding Thin Metal Sheets Without a Backing Sheet.* TRANSLATIONS-VE RIECANSKY, 2006. **12229**.
80. Garai, J., *Physical model for the latent heat of fusion.* Chemical physics letters, 2004. **398**(1): p. 98-101.
81. Matsunawa, A. and T. Ohnawa, *Beam-plume interaction in laser materials processing.* Transactions of the JWRI(Japan Welding Research Institute)(Japan), 1991. **20**(1): p. 9-15.
82. Matsunawa, A., et al., *Dynamics of keyhole and molten pool in laser welding.* Journal of laser Applications, 1998. **10**: p. 247.
83. Wang, R.R. and C.T. Chang, *Thermal modeling of laser welding for titanium dental restorations.* The Journal of prosthetic dentistry, 1998. **79**(3): p. 335-341.
84. Yang, J., et al., *Experimental investigation and 3D finite element prediction of the heat affected zone during laser assisted machining of Ti6Al4V alloy.* Journal of materials processing technology, 2010. **210**(15): p. 2215-2222.
85. Frewin, M. and D. Scott, *Finite element model of pulsed laser welding.* WELDING JOURNAL-NEW YORK-, 1999. **78**: p. 15-s.
86. Penner, S., M. Rotenberg, and O. SHARMA, *Phase-change problems with variable surface temperatures.* AIAA Journal, 1967. **5**(4): p. 677-682.
87. Holman, J., *Heat transfer 9th Edition.* New York, Boston, McGraw-Hill, Inc, 2002.
88. Stewart, J., *Calculus Concepts and Contexts.* 2001, Brooks/Cole.
89. El-Adawi, M. and E. Elshehawey, *Heating a slab induced by a time-dependent laser irradiance--An exact solution.* Journal of applied physics, 1986. **60**(7): p. 2250-2255.
90. Carslaw, H.S. and J.C. Jaeger, *Conduction of heat in solids.* Oxford: Clarendon Press, 1959, 2nd ed., 1959. **1**.

91. Boley, B.A., *Upper and lower bounds in problems of melting or solidifying slabs.* The Quarterly Journal of Mechanics and Applied Mathematics, 1964. **17**(3): p. 253-269.
92. Gebhart, B., *Heat Transfer: 2d Ed.* 1971: McGraw-Hill.